UNIVERSITY OF CALIFORNIA, SAN DIEGO

SAN DIEGO STATE UNIVERSITY

Sensitive Standoff Nonlinear Spectroscopic Studies of Gas- and Condensed-Phase Molecules in Ambient Conditions for Environmental and Security Applications

A dissertation submitted in partial satisfaction of the requirements for the degree
Doctor of Philosophy
in
Chemistry

By

Marc Sannes Gregerson

Committee in Charge:

University of California, San Diego

Professor Andrew Kummel, Co-Chair
Professor Dariusz Stramski
Professor Jerry Yang

San Diego State University

Professor William G. Tong, Chair
Professor Gregory Kalyuzhny
Professor Chun-Ta Lai

2012

This Dissertation of Marc Sannes Gregerson is approved, and it is acceptable in quality and form for publication on microfilm:

_____

_____

_____

_____

_____
Co-Chair

_____
Chair

University of California, San Diego

San Diego State University

2012

Dedication

To my wife Barbara, daughter Dharma, and son Alexander, we have been in California for eight years now. My little girl is now a teenager, my son is now growing so fast I cannot believe it. It has been a great 8 years. I hope the next 8 years are as good as the last 8 years. Thank you for your patience and support while I pursued this goal. I love you all.

Table of Contents

List of Figures

List of Tables

Acknowledgments

There are many people that I would like to thank for the assistance they gave me. I would like to thank Dr. William Tong for his assistance in completing this work. His guidance and insight were invaluable in solving the problems that inevitably arise during the course of research. Thank you to Adrian for her expertise and training in how laser wave-mixing setups operate. To Donna, you made me think hard about our lab and the work we do. I think I learned more in helping you than you learned from me. To Marcel, Tiffany and Manna, you three were the newbies after Wendy left. You brought fresh enthusiasm and ideas to the lab. Thank you. Ashley, you impressed me with your intelligence, perseverance and cheerfulness. I hope you and Michael have great success in Arizona. And Wendy, you were my best friend in San Diego. We spent a lot of time in the lab together banging on the research trying to get things done. You also threw the best parties and let me wear my chef's hat. I am honored to call you a friend.

I would like to thank Sam Crivello and the staff at Daylight Solutions, Inc., for providing special services for our quantum cascade lasers used in this dissertation. I would like to thank Dr. LeRoy Lafferty, Dr. Ratnasamy Somanathan for their support in obtaining NMR and FT-IR spectra. I would also like to thank Rhett Barnes, thank you for letting me bounce my thoughts off you while you were visiting our lab. It was great having an outsider's perspective. I would also like to thank Donnie Eastman and Mark Kottke for reading some of the chapters and editing them for me.

Vitae

May 30, 1971	Born, Decorah, Iowa
1989	Graduate, Clear Lake Community High School Clear Lake, Iowa
1993	Bachelor of Science, Interdisciplinary Studies Iowa State University, Ames, IA
1994	Bachelor of Science, Clinical Laboratory Sciences University of Iowa, Iowa City, IA
1995 – 1998	Bench Technologist Medtox Scientific, St. Paul, MN
1998 – 2000	Second Shift Supervisor Medtox Scientific, St. Paul, MN
2000 – 2001	Clinical Lab Scientist, Department of Pathology University of Iowa Hospitals and Clinics, Iowa City, IA
2001 – 2004	Research Assistant II, Department of Anesthesia University of Iowa Hospitals and Clinics, Iowa City, IA
2004 – 2011	Research and Teaching Assistant San Diego State University
2012	Joint Ph.D. Program, Chemistry University of California at San Diego San Diego State University San Diego, CA
2012	Forensic Scientist Orange County Crime Lab

Publications

1. Gregerson, MS; Tong, WG. The sensitive detection of TNT complexes using degenerate four wave mixing. *In Preparation*

2. Gregerson, MS; Tong, WG. The detection of Triacetone Triperoxide using degenerate four wave mixing. *In Preparation*

3. Gregerson, MS; Tong, WG. The Detection of homonuclear diatomic gas molecules at ambient conditions using degenerate four wave mixing. *In Preparation*

4. Lyons, W; Schafer, J; Briggs, R; Gregerson, M; Tong, WG. Nonlinear wave-mixing spectroscopy for sub-Doppler isotope analysis with trace-level detection sensitivity. *Proceedings of SPIE - The International Society for Optical Engineering*, v 5971, *Photonic Applications in Nonlinear Optics, Nanophotonics, and Microwave Photonics*, 2005,

5. Baker, MT; Gregerson, MS; Naguib M. Role of lipid in sulfite-dependent propofol dimerization. *Anesthesiology*, 2004, 100(5).

6. Naguib, M; Baker, MT; Spadoni, G; Gregerson, MS. Hypnotic and analgesic Effects of 2-Bromomelatonin. *Anesthesia and Analgesia*. 97 (3): SEP 2003

7. Martin, SM; Baker, MT; Gregerson, MS; Buettner, GR. Detection of sulfite free radical in propofol and other drug formulations. *Free Radical Biology and Medicine*, 35: 426 Suppl. 1 2003.

8. Baker, MT; Gregerson, MS; Martin, SM; Buettner, GR. Free radical and drug oxidation products in an intensive care unit sedative; propofol with sulfite. *Critical Care Medicine* 2003, 31(3).

9. Baker MT, Gregerson MS, Naguib M. Sulfite radical formation in a sulfite containing morphine preparation. *Critical Care Medicine* 30 (12): 239 Suppl. S DEC 2002

10. Baker, MT; Dehring, DJ; Gregerson, MS. Sulfite supported lipid peroxidation in propofol emulsions. *Anesthesiology* 2002, 97(5).

ABSTRACT OF THE DISSERTATION

Sensitive Nonlinear Spectroscopic Studies of Gas- and Condensed-Phase Molecules in Ambient Conditions for Environmental and Security Applications

By

Marc Sannes Gregerson

Doctor of Philosophy in Chemistry

University of California, San Diego, 2012
San Diego State University, 2012

Professor William G. Tong, Chair
Professor Andrew Kummel, Co-Chair

Multiphoton laser wave-mixing spectroscopy is presented as a sensitive and specific optical detection technique for liquid and gas phase analytes. Compared to other detection methods, wave-mixing offers numerous advantages including small laser probes, high spatial resolution, excellent sensitivity, and specificity that allows for the identification of analytes. The signal generated is a coherent laser-like beam, thus it can be spatially and optically modulated to enhance the signal-to-noise ratio of the system. The laser wave-mixing signal exhibits a quadratic dependence on analyte absorptivity, thus small changes in concentration result in large changes in signal intensity. Furthermore, laser wave-mixing has a cubic dependence on laser power, allowing for the use of low power laser systems.

Laser wave-mixing is shown to be a sensitive detection technique that is adapted for detection beyond normal lab scale distances. The simple two-beam forward scattering arrangement is used to detect molecular bromine gas in a sealed 10 cm gas cell. Bromine is detected at distances from 0.25 to 6 meters while maintaining sensitivity in the parts per billion range. This proof of concept work has applications in environmental and medical applications that require real time detection of gaseous analytes.

The detection of explosives in the visible range is an important technique for forensic, defense, and security applications. This work shows that laser wave-mixing can be applied to the colorimetric detection of both trinitrotoluene and triacetone triperoxide. Trinitrotoluene is detected with parts per trillion sensitivity using a 514 nm Argon ion laser and triacetone triperoxide is detected in the parts per billion range using a 405 nm solid state diode laser system.

Laser wave-mixing is then adapted to use mid-infrared quantum cascade lasers for the detection of explosives and explosives precursors. Quantum cascade lasers are powerful, compact, lasers that feature wavelength and power tunability. This laser system offers sensitivity and specificity in detection of dinitrotoluene, triacetone triperoxide, and acetone as native species in the gas and liquid phase. The wavelength tunability of quantum cascade lasers allows for the identification of these molecules in the fingerprint mid-IR region with parts per billion detection sensitivities.

Chapter 1

Introduction of Degenerate Four-Wave Mixing

1.1 Motivation

Multi-photon nonlinear laser spectroscopy is one of the most powerful tools used by chemists to identify and quantify molecules in a variety of sample types. We employ a nonlinear technique called degenerate four-wave mixing (DFWM), one of the most sensitive optical absorption-based spectroscopic techniques. Our excellent DFWM sensitivity levels allow reliable study of trace-concentration analytes in complex samples.

This work investigates the laser wave-mixing signal characteristics at various standoff detection distances using different molecules that are important for environmental and security applications, including TNT, TATP, HMTD, RDX and HMX. Beginning with the Russian-Japanese War of 1905, TNT saw wide use as a military explosive [1]. In the following 100 years, the need for improved detection of TNT has risen in numerous areas. Land-mine detection, improvised explosive device (IED) detection, munitions remediation, post-blast forensic investigations and homeland security applications now require more sensitive and reliable detection methods.

Wolffenstein first synthesized triacetone triperoxide (TATP) in 1895 [2] and TATP is an attractive explosive for terrorist and criminal organizations since it can be easily synthesized with materials that are available from grocery stores, pharmacies and other retail outlets [3]. The ease of synthesis using readily

available materials makes it imperative that we have a sensitive, reliable and specific detection technique available for law enforcement agencies. TATP does not yield significant UV-visible optical absorption or fluorescence signal [4]; however, it has a characteristic IR absorption spectrum. This work investigates the use of mid-infrared quantum cascade lasers in a DFWM setup to detect and quantify TATP.

Acetone has an indirect effect on the concentration of atmospheric ozone. Acetone triggers the production of several atmospheric gases that in turn affect ozone concentrations [5]. Acetone has applications in a variety of fields from environmental and biomedical to defense areas. There are a number of medical conditions that induce the production of acetone in the body, such that it rises above the natural ppb range seen in healthy adults. Diabetes [6], congestive heart failure [7] and fat burning measurements [8] all trigger the production of acetone. Acetone is also one of two principle components needed to make the explosive triacetone triperoxide. Acetone has a much higher vapor pressure as compared to that of triacetone triperoxide, and hence, it is an excellent analyte for probing with laser wave mixing. Given current and historical events, there is a need for very sensitive and reliable detection method with a reasonable standoff remote detection capability. This has been the primary motivator for this work.

1.2 Laser Wave Mixing

The development of the first laser in 1960 by Maiman [9] led to the field of laser spectroscopy and opened up a completely new area of investigation in the field of analytical chemistry. The conception and discovery of phase conjugation was the next big step in the use of lasers for chemical analysis. There were a number of early experiments designed to test the concept of phase-conjugate beams.

Zel'dovich *et al.* [10] utilized a stimulated Mandel'stam-Brillouin scattering experiment to show that narrow beam spots with minimal diffraction distribution could be created by passing the beam through the same medium twice. This resulted in the production of a time-reversed replica of the input beam although the replica beam was slightly frequency shifted. It was the first work to explore the effects of phase distorting in nonlinear media using counter propagating beams. Later, Yariv [11] introduced a three-wave mixing setup, with strict phase-matching requirements.

In 1977, Hellwarth [12] performed experiments in an attempt to remove the phase-matching requirements that limited the previous work by Yariv. He described a nonlinear method for generating nearly instantaneous phase conjugate beams. The interaction of an incident pump beam with a counter-propagating beam in a nonlinear medium produced a time-reversed replica of the input beam that was not limited by previous phase-matching requirements. In 1977, Yariv and Pepper [13] also began investigating degenerate four-wave mixing. They showed that by using two intense pump beams in combination with

a weak probe beam, one could generate a fourth beam that is the phase conjugate of the probe beam.

Both Hellwarth and Yariv-Pepper studies utilized the dynamic holography system first published by Kogelnik [14]. In Kogelnik's method, two counter-propagating pump beams interact in a medium with third order nonlinearity. A third probe beam interacts with the pump beams and the medium to produce a fourth phase-conjugate beam that propagates in the opposite direction of the probe beam.

While work on the theoretical side of degenerate four-wave mixing continues, there is a growing body of work that utilizes DFWM as a sensitive detection technique for a variety of samples in both gas- and condensed-phase samples. The study of DFWM encompasses a large number of applications. Putting aside applications in the nonlinear optics and quantum electronics fields, DFWM has been an active area of research in the nonlinear spectroscopy of atoms and molecules.

In 1984, Tong and Yeung [15] measured the hyperfine structures of Cu isotopes and determined relative abundances of ^{63}Cu and ^{65}Cu isotopes in a demountable dc discharge plasma atomizer. They determined a limit of detection of 1.6 ppm using laser-induced ionization spectroscopy. Pender and Hesselink [16] detected Na in an air-acetylene flame and marked the first time DFWM detected an analyte in an analytical flame. In 1986, Ewart and O'Leary [17] detected the hydroxyl radicals in an air-methane flame in a commercial flame absorption spectrophotometer using DFWM.

Condensed-phase samples were the next in the development of DFWM as an analytical technique. In 1989, Wu and Tong [18] reported the first ultrasensitive DFWM detection of Eosin B in a flowing liquid analyte cell with a detection limit of 2.9×10^{-18} moles in a probe volume of 0.14 μL.

From this point forward, research into condensed-phase and gas-phase samples blossomed. Numerous groups reported continually lower detection limits with a wide variety of analytes. DFWM has been coupled to the ICP atomizer torch, hollow cathode discharge cells, graphite furnaces, liquid chromatography systems, capillary electrophoresis systems, flowing capillary cells, protein micro-arrays, DNA micro-arrays and sol-gel matrices.

Research into the applications of DFWM continues and different groups report DFWM detectors interfaced to more and more sample delivery systems. Given its reported sensitivities, DFWM will be used to detect ever-smaller concentrations of analytes. The use of multiple lasers with different wavelengths will result in DFWM being used as a compact tool for the differentiation of multiple compounds in complex mixtures.

1.3 Comparison to Other Optical Techniques

A comparison to several different techniques is needed to fully present the advantages of DFWM in optical spectroscopy. Since DFWM is an optical absorption technique, the most obvious comparison is to UV-visible absorption spectrometry and other laser-based absorption methods. Other methods include Raman spectroscopy, coherent Raman methods, fluorescence-based detection

methods and multi-photon laser methods. Although DFWM has not been explored as much for the determination of functional groups and molecular structures, it has been demonstrated to be as sensitive, if not more sensitive than many optical spectroscopy techniques including fluorescence-based methods.

Standard UV-visible absorption spectromertry is a one-photon excitation process and relaxation proceeds by thermal and/or radiative processes. The UV-visible absorption signal is governed by Beers Law, and therefore, it has a linear relationship with molar absorptivity (and concentration). UV-visible absorption methods typically show relatively poor limits of detection in the parts-per-million (ppm) to parts-per-billion (ppb) ranges. An excellent laser-based UV-visible absorption spectrometer may be able to detect in the ppb to ppt range. For comparison, DFWM sensitivity levels have been demonstrated to be orders of magnitude better in the parts-per-quadrillion (ppq) levels [19]. The exquisite sensitivity of DFWM is attributable to its inherent advantages including coherent collimated signal beams, high S/N, minimum background, separate signal propagation directions and nonlinear laser power and concentration dependencies.

Typical limits of detection for a conventional Raman method are in the parts-per-billion range, with better results (parts-per-trillion) when using resonance Raman methods. The Stokes and anti-Stokes Raman scattering signals are relatively weak as compared to many other optical detection methods. In contrast, the DFWM signal is instantaneous and continuous as long as an absorbing medium in present. The DFWM signal does not rely upon

analyte emission or fluorescence, and hence, both fluorescing and non-fluorescing samples can be detected. Another advantage is that the DFWM signal is a coherent laser-like beam, whereas the conventional Raman signal is an incoherent diffused light. All the signal intensity is concentrated in the coherent DFWM signal beam, and hence, it yields a much higher S/N.

The fluorescence signal is also an incoherent diffused light that is collected and detected by a collection lens, and hence, only a small fraction of the overall fluorescence signal is collected. Having absorbed energy and reached one of the higher vibrational levels of an excited state, the molecule rapidly loses its excess energy until it reaches the lowest vibrational level of the excited state. From this level, the molecule can return to any of the vibrational levels of the ground state, emitting its energy in the form of a fluorescence signal [20].

Some laser-based fluorescence methods demonstrate sensitivity levels in the parts-per-trillion to parts-per-quadrillion range. This is very competitive with the sensitivity levels reported for DFWM. The major advantage that DFWM has over fluorescence is that it can detect any absorbing analyte. Fluorescence requires a fluorescing analyte or an analyte labeled or tagged with a fluorescent dye. This is a drawback since it is time consuming and costly to label analytes and some analytes cannot be labeled at all. Fluorescent signal is incoherent, and thus, the S/N is not as high as that of DFWM. Fluorescence and Raman methods yield incoherent signals that decay with distance from the sample. DFWM produces a coherent signal beam that does not decay as much over a

long distance, and hence, DFWM offers inherent advantages for standoff detection of security, military and environmental analytes.

1.4 Lasers

The word laser is an acronym for **L**ight **A**mplification by **S**timulated **E**mission of **R**adiation. Theodore Maiman at Hughes Research Lab in California developed the first laser in 1960. It was the visible counterpart to the maser, **M**icrowave **A**mplification by **S**timulated **E**mission of **R**adiation. Lasers have a number of characteristics that are useful in optical spectroscopy. The light emitted is monochromatic and spatially and temporally coherent, allowing it to remain collimated over a long distance. The development of the laser has led to major advances in other fields including chemistry, physics, optical science and medicine.

There are two major requirements for the generation of a laser beam. A metastable excited state must exist, with a lifetime sufficient for participation in stimulated emission. A population inversion is needed so that the population of the upper energy state is greater than that of the lower state. There are different mechanisms by which a lasing medium can obtain a population inversion. In a three-level laser system, as shown in **FIGURE 1.1,** the lasing medium is pumped from the ground state E_o to an excited state E_2. The medium then spontaneously non-radiatively relaxes to the intermediate energy level E_1. The lifetime of the intermediate energy level is longer than that of the excited level, allowing more and more of the medium to populate the intermediate energy level. When the

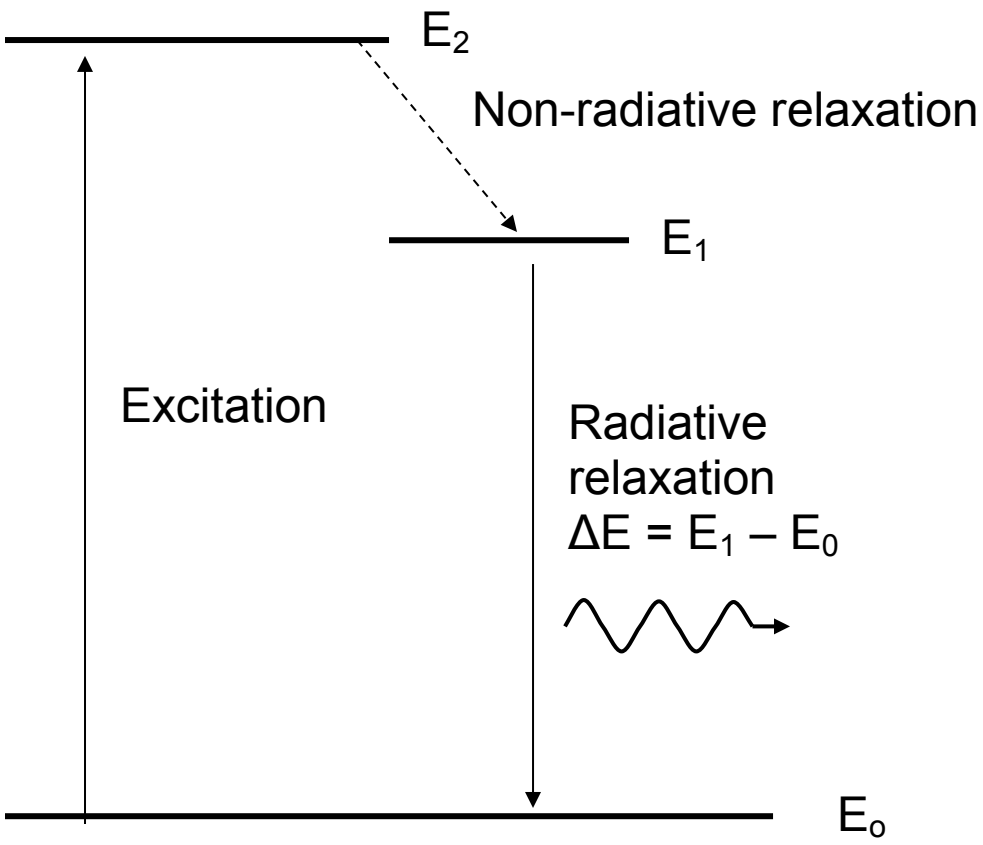

FIGURE 1.1 Three-level laser system. The lasing medium is excited to level E_2 by an optical pump. The system relaxes via a non-radiative process to a relatively long-lived intermediate state, E_1. The system further relaxes back to ground state via emission of a photon. When the population in E_1 is greater than that in $E_{0,}$ a population inversion has occurred and lasing is initiated.

population of the intermediate states becomes larger than that of the ground state, population inversion is achieved and lasing is initiated. As the lasing medium relaxes from the intermediate level to the ground state, a photon is emitted. This photon has the wavelength that corresponds to the energy difference between the intermediate level and the ground state. The difficulty with the three-level system is that the population inversion is much harder to achieve and it requires strong pumping processes and more energy to initiate lasing. The classic example of a three-level laser system is the ruby laser first reported by Maiman in 1960.

In a four-level laser system, as shown in **FIGRUE 1.2,** the lasing medium is excited from the ground state E_o to an excited state E_3. The medium non-radiatively relaxes to a lower-energy intermediate state E_2. The medium then relaxes from E_2 to an even lower-energy intermediate level E_1. The final transition is a non-radiative relaxation from E_1 back to the ground state. The beam emitted in the four-level system has the wavelength of light that corresponds to the energy difference between E_2 and E_1. Given that E_1 is initially unpopulated and that the lasing medium relaxes to the higher level E_2, it is easier to obtain a population inversion between the two intermediate states. The lifetime of E_3 is much shorter than that of E_2, thus a population accumulates in E_2. The lifetime of E_1 is also relatively short and always less than that of E_2, thus the population of E_1 is always near zero. Given that the intermediate energy level E_2 has the longest lifetime of the three different non-ground level states, it is

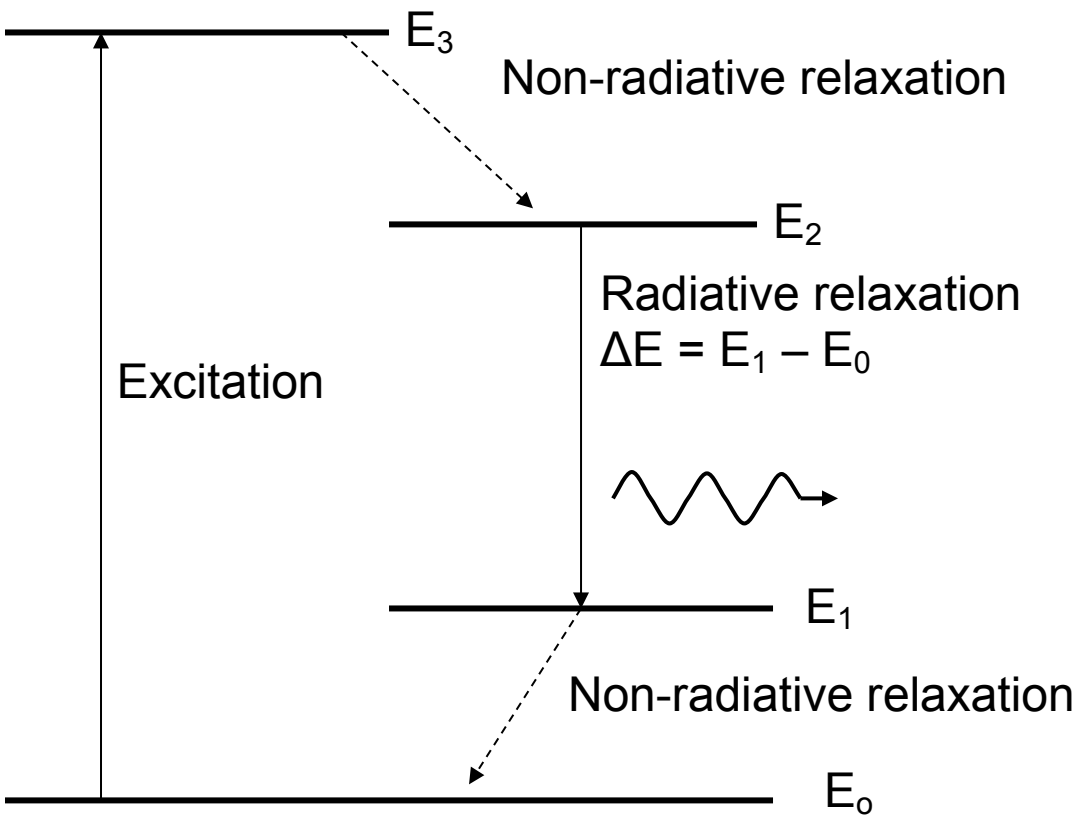

FIGURE 1.2 Four-level laser system. The lasing material is pumped to an excited state, E_3. The system relaxes via a non-radiative process to a relatively long-lived E_2 state. Since the population of E_1 is not as high as that of E_0, it is easier to obtain population inversion between E_2 and E_1.

easy to induce a population inversion between levels E_2 and E_1. The argon ion laser used in this work is an example of the four-level laser system.

FIGURE 1.3 shows the stimulated amplification effect exhibited by lasers. Initially, the ground state population is larger than the excited state population. The top portion of the diagram shows that the lasing medium is pumped to achieve population inversion. The spontaneous relaxation of one atom in the metastable state releases a photon that stimulates another atom to emit another photon. These two photons then induce more emissions. The process creates a cascade of photons that becomes a coherent amplified beam of laser light.

FIGURE 1.4 shows a generic laser system. Two mirrors cap the lasing medium, one is 100% reflective and the other is less than 100% reflective. The purpose of this arrangement is to amplify stimulated emission by bouncing the photons between the two mirrors. The photons that remain parallel to the beam path will continue to bounce back and forth and amplify in the cavity until enough photons have been generated to pass through the partially transmitting mirror. All non-parallel photons are lost from the laser cavity and not amplified. The resulting laser beam has the characteristics expected including monochromaticity, good collimation and small divergence.

A relatively new type of laser used in this work is the external cavity tunable quantum-cascade laser (QCL), first reported by Faist in 1994 [21]. The QCL is a quantum-well laser as opposed to the band-gap transition types found in conventional semiconductor lasers. A quantum-cascade laser is constructed of multiple thin layers of semiconductor material (quantum wells) and it is a

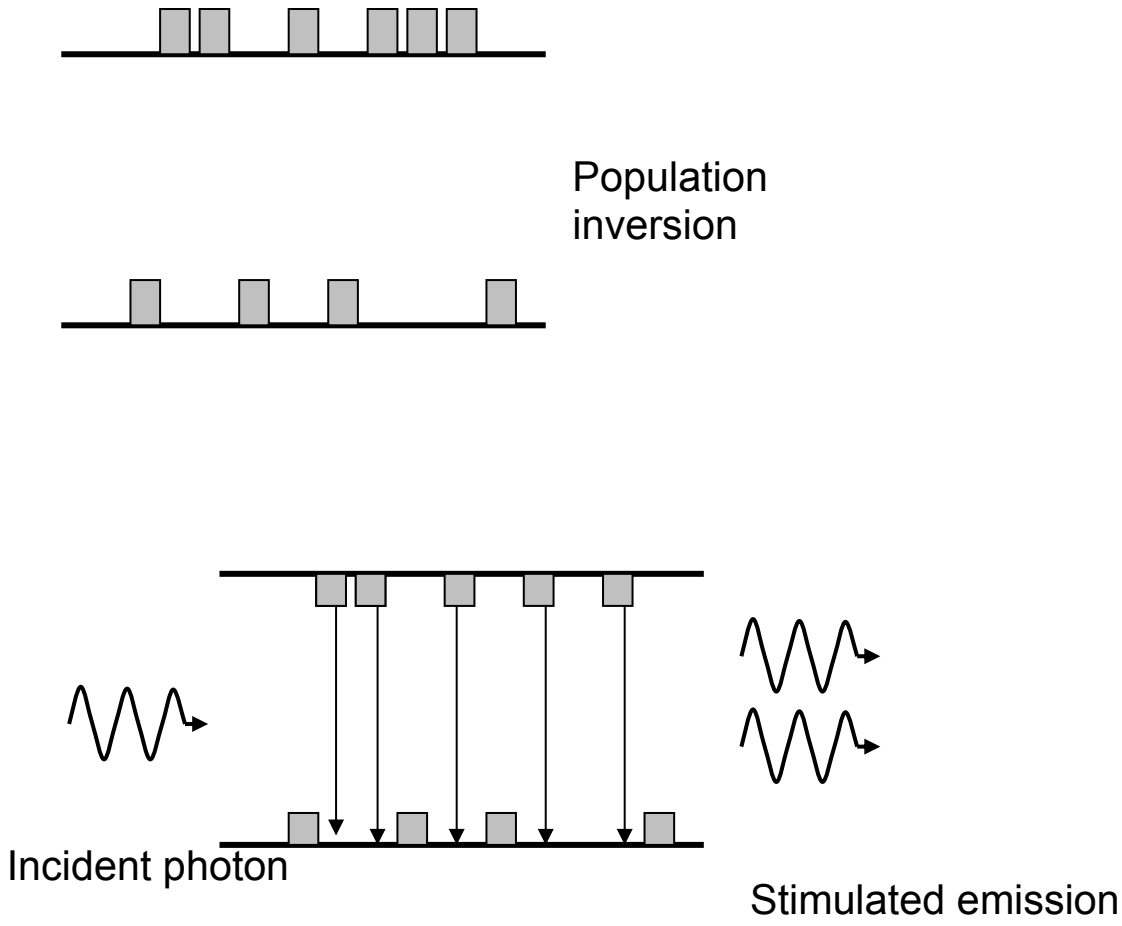

FIGURE 1.3 Stimulated emission. When the population of the higher energy level exceeds that of the preferred lower level, population inversion occurs. When an incident photon with an energy that is equal to the energy difference between the excited and ground states interacts with an excited atom, the excited atom relaxes and emits a photon of the same energy and the total amplitude is amplified.

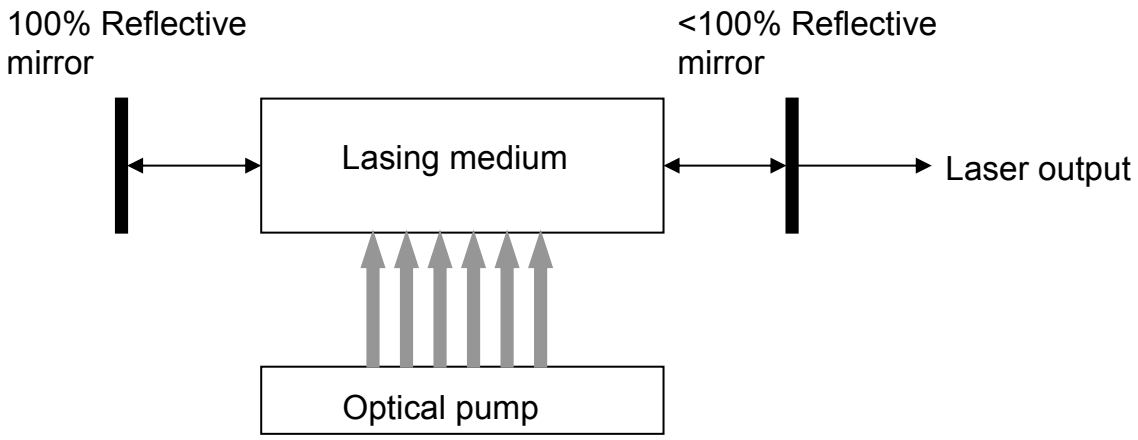

FIGURE 1.4 A generic laser system showing optical pumping, the laser cavity and the laser output. An optical pump excites the lasing medium. The resulting photons are bounced between the mirrors, causing more stimulated emission. When enough photons are produced, the output beam penetrates through the partially reflective mirror.

unipolar light source based on only one type of carrier, electrons. The electrons make intersubband (*intraband*) transitions between confined energy levels within the conduction band. The energy levels are arranged such that electrons transition from one quantum well to the next by tunneling or cascading. Each tunneling event results in the release of a photon. One electron can emit multiple photons by tunneling through successive quantum wells, as shown in **FIGURE 1. 5**. The emission wavelength of a quantum-cascade laser is determined not by the semiconductor band gap, but by the quantum confinement in the wells created by the quantum-well material and the barrier material. The thickness of these layers determines the wavelength of the QCL output.

Another laser used in this work is a 405 nm solid-state semiconductor laser made of InGaN. This laser generates photons by transitioning high-energy electrons across the band gap between the conduction and valence bands of the semiconductor laser, as shown in **FIGURE 1.6.** The material used in the semiconductor determines the wavelength output of the laser. When an electron transitions across the band gap, it stops in the band to which it transitioned. Therefore, one electron nets only one photon.

1.5 Conclusions

Degenerate four-wave mixing is an ultrasensitive laser spectroscopic technique that has been developed over the last 30 years. Nonlinear DFWM detection systems have been developed using a wide range of lasers and

demonstrated to for sensitive detection of a wide range of analytes including isotopes, atomic gases, small organic molecules and bio cells.

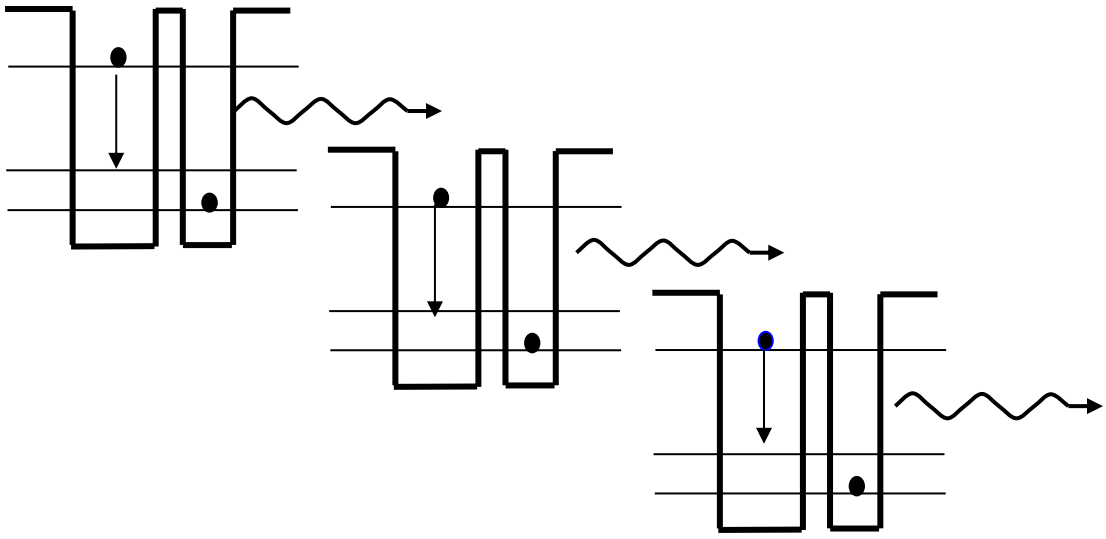

FIGURE 1.5 Quantum-well structure and electron tunneling in a quantum cascade laser. As the electron tunnels, it releases a photon. One electron in the system can tunnel many times, thus producing many photons.

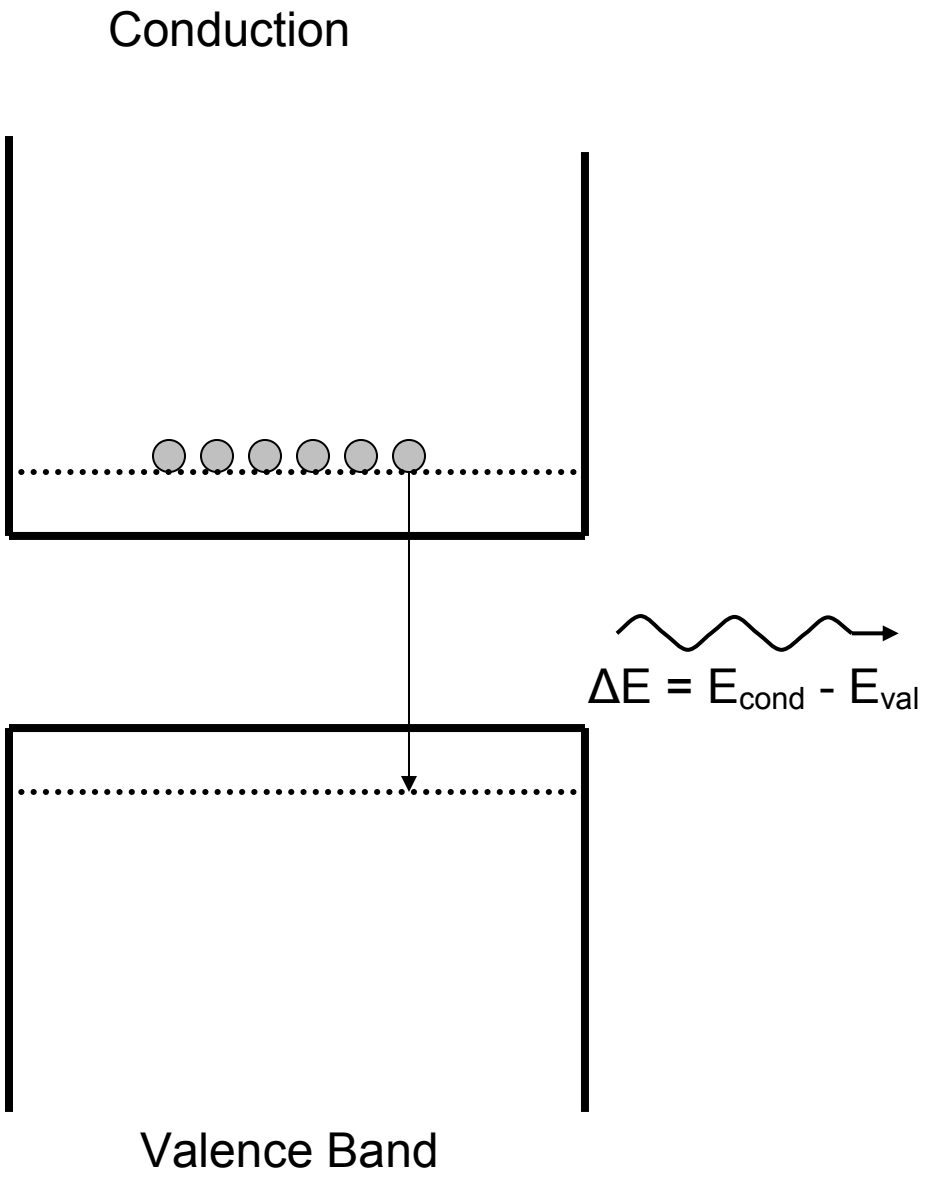

FIGURE 1.6 The transition and photon emission in a traditional semiconductor laser. The semiconductor laser operates on the principle that photons are released when electrons jump across the band gap in the materials.

REFERENCES

1. Karasch, C.; Popovic, M.; Qasim, M.; Bajpai, RK. *Applied Biochemistry and Biotechnology.* **2002**, vol 98-100, pg. 1173-1185.

2. Wolffenstein, R.: *Chem. Ber.* **1895**, *28*, 2265 – 2269.

3. Olsen, JM: *The San Diego Union Tribune*, **2007**, Nov 23; Bonner, R: *The New York Times*, **2005**, Nov 15.

4. Schulte-Ladbeck, R; Edelmann, A; Quintas, G; Lendl, B; Karst, U*: Anal. Chem.* **2006**, *78,* 8150 – 8155.

5. Stockwell, WR; Milford, JB; Gao, D; Yang, YJ; *Atmospheric Environment,* **1995**, *29(14)*, 1591- 1599.

6. Deng, C; Zhang, J; Yu, X; Zhang, W; Zhang, X: *Journal Chromatography B*, **2004**, 269-275.

7. Kupari, M; Lommi, J; Ventila, M; Karjalainen, U: *American Journal of Cardiology*, **1995**, *76*, 1076-1078.

8. Kundu, SK; Bruzek, JA; Nair, R; Judilla, AM: *Clinical Chemistry*, **1993**, *39(1)*, 87-92.

9. Maiman, TH.: *Nature,* **1960**, 187, 493-494.

10. Zel'dovich, BY; Popovich, VI; Ragul'skii, VV; Faizullov, PN: *Soviet Physics JETP Letters*, **1972**, 15(3), 109-113.

11. Yariv, AJ: *Journal of the Optical Society of America*, **1976**, 66, 301-306.

12. Hellwarth, RW: *Journal of the Optical Society of America*, **1977**, 66, 1-3.

13. Yariv, AJ; Pepper, DM: *Optics Letters*, **1977**, 1(1), 16-18.

14. Kogelnik, H.: *Bell Systems Technical Journal*, **1965**, 44, 2451-2455.

15. Tong, WG; Yeung, ES: *Talanta*, **1984**, 31(9), 659-665.

16. Pender, J; Hesselink, L.: *Optics Letters*, **1985**, 10(6), 264-266.

17. Ewart, P; O'Leary, SV: *Optics Letters*, **1986**, 11(5), 279-281.

18. Wu, Z; Tong, WG: *Analytical Chemistry*, **1989**, 61(9), 998-1001.

19. Mickadeit, FK; Berniolles, S; Kemp, HR; Tong, WG: *Analytical Chemistry*, **2004**, 75(6), 788-792.

20. Perkin Elmer, Inc.: *An Introduction to Fluorescence Spectroscopy*. **2000**.

21. Faist, Capasso, Sivco, Sirtori, Hutchinson, Cho: *Science*, **22 April 1994**, vol 264, pg. 553 – 556.

Chapter 2

Theoretical Considerations For Degenerate Four-Wave Mixing

2.1 Laser Wave-Mixing Spectroscopy

Laser wave-mixing spectroscopy is an optical absorption method based on the patterns created by the constructive and destructive interferences of two overlapping input laser beams. In the configuration used in this work, two beams of the same wavelength overlap at a small angle creating a pattern of constructive and destructive interferences. When an absorbing analyte is present in the overlap region of the lasers, energy is absorbed by the analyte. Non-radiative relaxation by the absorbing molecules imprints a thermal grating in the surrounding medium. This results in a change in the refractive index of the medium. When this thermal grating is formed, a portion the pump beam and a portion of the probe beam diffract off the thermal grating with the same angle as that between the pump and probe beams. The diffracted beams are the laser wave-mixing signal beams. Given the geometric arrangement of the optics in this particular laser wave-mixing setup, the signal beams propagate in the same general direction as the pump and probe beams. Thus, the technique is called forward-scattering laser wave-mixing spectroscopy [1] and is diagramed in **FIGURE 2.1**.

The signal beams have the same coherence and directionality characteristics as those of the pump and probe beams. The angle between the pump beam (or the probe beam) and the signal beam is the same as that between the input

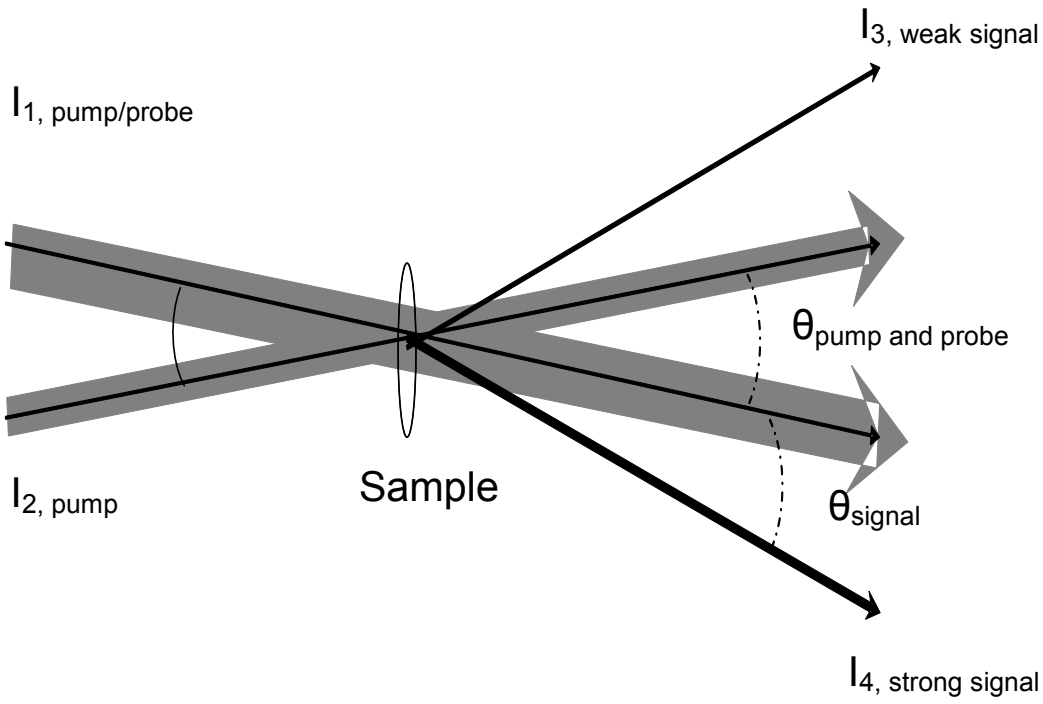

FIGURE 2.1 Forward-scattering degenerate four wave-mixing signal beams. The angle between the pump/probe and pump beams is the angle at which the signal beam diffracts off the grating formed in the sample.

beams. Hence, the signal beam separates from the pump or probe beam within a short distance. This allows for easy and efficient signal collection against a dark background.

The laser wave-mixing signal exhibits a quadratic dependence on the molar absorptivity (or concentration) and a cubic dependence on the total laser power of the input beams. Thus, the technique exhibits sensitivity far beyond that of conventional optical absorption spectroscopic techniques.

2.2 Phase-Conjugate Mirrors

A discussion of the underlying theory of degenerate four-wave mixing (DFWM) begins with a brief description of optical phase conjugation. A phase-conjugate mirror is a nonlinear medium that performs a *complex* conjugation on the spatial part of the *complex* amplitude of an impinging electromagnetic field [2]. The reflected beam propagates back on the incident beam, with its phase flipped 180° such that α becomes –α. The reflected waves of linearly- and circularly-polarized lights have the same polarization characteristics as the incident wave. **FIGURE 2.2** shows how a conventional mirror and a phase-conjugate mirror act upon an incident light beam. A regular mirror reflects incident beams at the same angle as they strike the mirror, as shown in Diagram 1 and Diagram 2 in Figure 2.2. A phase-conjugate mirror reflects the beam back on itself, regardless of the angle of incidence, as shown in Diagram 3 and Diagram 4 in Figure 2.2.

Phase Conjugate Mirror

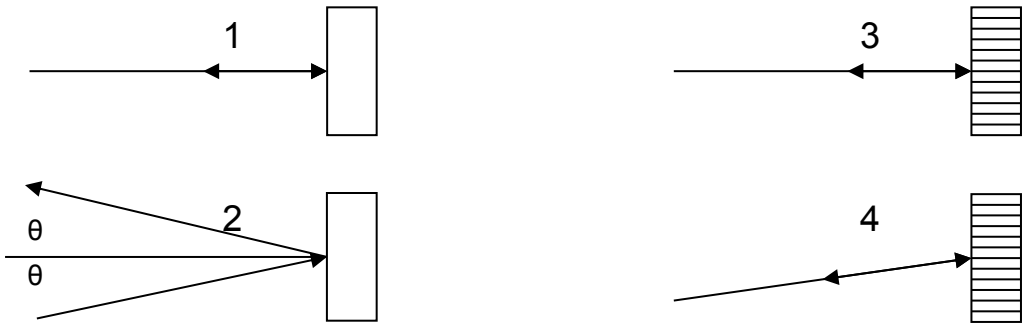

Figure 1 and 2 are regular mirrors. The angle of reflection is the same as the angle of incidence ($\theta_r = \theta_i$).
Figure 3 and 4 are phase conjugate mirrors. Light is reflected 180° upon itself, regardless of the angle of incidence

FIGURE 2.2 Comparison of a regular mirror and a phase-conjugate mirror. A regular mirror reflects light with the incident angle the same as the reflected angle. A phase-conjugate mirror bounces the light back in the original incident path, regardless of the angle of incidence.

Many branches of nonlinear spectroscopy offer a wide range of potential real-world applications. Two-photon coupling produces second harmonic generation, optical rectification, parametric mixing and the Pockels effect. These are all second-order nonlinear susceptibility phenomenon. Three-photon coupling allows third harmonic generation, Raman scattering, non-degenerate four wave mixing, Brillouin scattering, the Kerr effect, two-photon absorption and laser wave mixing [3].

2.3 Absorption Selection Rules

As mentioned previously, DFWM works in both gas and condensed phases and it can probe atoms in the gas phase and polyatomic molecules in solutions. As with any absorption technique, the DFWM signal generation requires that there must be a net change in the dipole moment of the atom or molecule for any absorption to occur. The multi-electron atom and polyatomic molecules follow different sets of selection rules.

In the case of the multi-electron atom, the basic selection rules that govern electronic transitions may be applied [4].

1. $\Delta l = \pm 1$. Only a single electron can move from one orbital to another.
2. $\Delta L = 0, \pm 1$. Change in total orbital angular momentum.
3. $\Delta J = 0, \pm 1$. Change in total angular momentum. Thus fine transitions from ½ → 3/2, 3/2 → 5/2, etc., are allowed. Also, the J=0 to J'=0 transition is forbidden.
4. $\Delta S = 0$. There is no change in overall spin.

There are some additional requirements for transitions in the multi-electron atom. The LaPorte rule (even ↔ odd parity) must be followed, and ΔL only remains valid for atoms with small spin-orbit couplings. Large spin-orbit couplings allow for mixing of terms with different S and L values [4].

Hyperfine splittings are due to the interaction of the nuclear magnetic moment with the electronic spin and the total angular momentum. These splittings are very small and require a high resolution spectroscopic technique to distinguish them. They can be used to differentiate isotopes such as ^{63}Cu and ^{65}Cu. Hyperfine splittings can even be used to differentiate atoms of similar mass that cannot be otherwise differentiated, even by mass spectrometry, such as ^{87}Sr (mass of 86.908884, I = 9/2) and ^{87}Rb (mass of 86.909187, I = 3/2). The hyperfine profiles of these two atoms are different and can be resolved by DFWM. Hence, DFWM can be used as an "atomic and hyperfine fingerprinting" method for the determination of isotopes in the gas phase.

The selection rules for diatomic and polyatomic molecules are more complicated than those for the multi-electronic atom. There are six selection rules identified by Bernath [4]:

1. ΔΛ = 0, ±1. This is the angular momentum rule. Σ→ Σ, Π→Σ, etc., transitions are allowed.
2. ΔS = 0. Spin multiplicity transitions are very weak until the atoms making up the diatomic molecule become heavy.
3. ΔΣ = 0. This is for Hund's Case A. There are many Hund's cases that may not obey this rule.

4. $\Delta\Omega = 0, \pm 1$. This is the total angular momentum rule.
5. $\Sigma^+ \rightarrow \Sigma^+$ and $\Sigma^- \rightarrow \Sigma^-$ are allowed due to the μ_z having Σ^+ symmetry. Note that $\Sigma^+ \rightarrow \Pi$ and $\Sigma^- \rightarrow \Pi$ are also allowed.
6. Transitions are g → u and u → g for centrosymmetric molecules.

Due to the varying sizes of the molecules and the number of different transitions, the broadband absorption spectrum of a given molecule may or may not yield useful information. One of the most useful pieces of information for an experimentalist using DFWM is λ_{max} since it allows for the selection of an appropriate laser for probing a molecule. Like other optical techniques, DFWM is subject to various spectral lineshape functions. The following is a brief discussion of six different line broadening parameters and how these factors can be minimized.

The natural linewidth is the smallest measurable profile for an atom or molecule [5]. It is inversely related to the lifetime of the excited state.

Pressure (Lorentzian) broadening is dependent on a variety of different factors, such as the collisional cross-section, pressure, atomic mass and molecular mass. It is the broadening of the line due to collisions between the atoms or molecules of interest with any other atoms or molecules that may be present. In the condensed phase, there is no way to minimize this broadening. In the gas phase, using a low-pressure atomizer, e.g., a hollow cathode discharge plasma cell, can reduce pressure broadening.

Doppler broadening is due to the thermal motion of the analyte being investigated. It is proportional to the square root of the analyte temperature. Even at low pressure levels, Doppler broadening is much wider than the natural linewidth [4]. Since Doppler broadening is proportional to the square root of temperature, its effect can be reduced by lowering the analyte temperature. In DFWM, using an experimental setup that uses two counterpropagating beams reduces Doppler broadening by probing a single velocity group of atoms [5].

Wall collisional broadening is due to collisions of the excited atoms or molecules with the walls of the sample chamber. A hollow cathode discharge cell, a capillary flow cell, a graphite furnace, and other sample holders all add to the relaxation of excited atoms and molecules. The broadening is directly proportional to the initial velocity of the atoms or molecules and inversely proportional to the diameter of the flow cell.

Transit-time broadening is dependent on the flight path of particles through the probe volume. It is proportional to the average speed of the particle and inversely proportional to the beam diameter. Reducing the probe volume (by reducing the beam diameter) in a DFWM setup can reduce the effects of transit-time broadening.

Power broadening is dependent on the laser power of the two input beams. To alleviate the effect of power broadening, one can simply reduce the laser intensity and use appropriate power levels below the saturation level. All these line broadening parameters [5] are summarized in **TABLE 2.1**.

TABLE 2.1 Line-broadening parameters [Briggs, RD: *Ph.D. Dissertation*, **2004**, UCSD-SDSU]. In the forward-scattering two-beam arrangemnet using molecular species, these parameters are not the major influence on peak width. Rather, the biggest influence on peak width is the number transitions available in a polyatomic molecule.

Type of Broadening	Cause of Broadening	Broadening Equation
Natural Line Width	Lifetime of excited state	$\Delta v,N = 1/2\pi T2$
Doppler	Thermal motion	$\Delta v,D = 0.0716x10\text{-}6vo(T/A)1/2$
Lorentzian	Pressure	$\Delta v,L = 2NA\sigma 2P[(2/\pi RT)(1/A + 1/M)]1/2$
Wall Collisional	Molecular collisions with sample cell wall	$\Delta v,WC = vo/2\pi L$
Transit Time	Molecule flight path through probe space	$\Delta v,TT = vo/2\pi a$
Power	Intensity of input laser power	$\Delta v,P = P12E/\hbar$

Natural Life Time: T_2 = lifetime of excited state

Doppler: v_o = initial frequency, T = temperature, A = atomic weight

Lorentzian: N_A = Avogadro's number, σ = collisional cross section, P = pressure,
R = universal gas constant, A = atomic weight , M = molecular weight

Wall Collsional: V_o = average speed, L = cell diameter

Transit Time: V_o = average speed, a = beam diameter

Power: P_{12} = transition dipole, E = laser field strength, $\hbar$ = Planck's constant

2.4 Laser-Induced Gratings

When two laser beams of the same wavelength interact at a small angle, an interference pattern is created. This pattern can be described by the light intensity modulation equation below [6]:

$$I = I_o[1 + m \cdot \cos(2\pi x/\Lambda)]$$

where I is the signal intensity, I_o is the total intensity of the input beams, x is the spatial coordinate, and Λ the spatial grating period. The pattern contrast is represented by the variable m and it is dependent upon the intensity of each beam (I_1 and I_2), as shown in the following equation [6]:

$$m = 2(\sqrt{I_1 I_2})/I_o$$

where I_o is the total intensity of the two input beams. The spatial grating period, Λ, depends on the angle (θ) between the input beams and the wavelength (λ) of the light used to form the gratings, as shown in the equation below [7]:

$$\Lambda = \lambda/(2 \sin(\theta/2))$$

The interference pattern formed by the interaction of the two beams of incident light is the result of constructive and destructive interferences as shoen in **FIGURE 2.3**. This interference pattern can be formed in an absorbing medium by different mechanisms. In the case of a liquid-phase sample, the constructive and destructive interferences form thermal gratings in the liquid. When an absorbing analyte passes through, the molecules are excited in the areas of constructive interference. The molecules remain less excited if they are in the region of destructive interference. The resulting grating then diffracts subsequent photons to generate the DFWM signal.

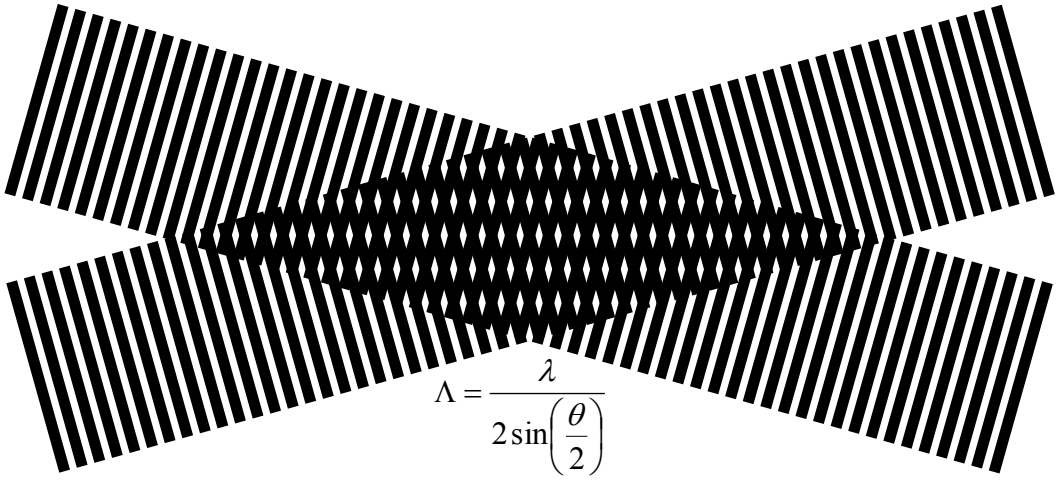

FIGURE 2.3 Grating pattern formed by overlapping input laser beams. When the two input laser beams overlap at a small angle, a pattern of constructive and destructive interference forms. This grating pattern imprints onto the absorbing medium. The equation describes the grating period. The exaggerated beams shown in this figure yield 8 grating periods from top to bottom.

In the gas phase, the interference pattern formed by the two incident beams is directly imprinted onto the absorbing gas-phase molecules. The portion of the gas- phase molecules that are in the area of constructive interference are excited, while the molecules in the deconstructive region of the grating remain less excited or in the ground state. The grating pattern is directly imprinted onto the absorber and is known as a population grating. Signal generation can be achieved either using the three-beam backward-scattering DFWM arrangement or the two-beam forward-scattering DFWM arrangement.

The DFWM signal is very strong and visible to the naked eye when both the laser power and the sample concentration are high. **FIGURE 2.4** shows the two input beams and the two signal beams generated. The distance from the input beam to the signal beam is the same as the distance between the two input beams. The signal beam is diffracted at the same angle, relative to the adjacent input beam, as compared to the angle between the two input beams.

2.5 Wave-Mixing Signal

All work done in this dissertation uses the forward-scattering two-beam DFWM optical alignment. For further discussion of other alignments and configurations, including the three-beam backward-scattering Doppler-free optical alingment, please see previous works from our lab [5]. In the two-beam forward-scattering DFWM arrangement, two signal beams are produced that exhibit the same characteristics [8]:

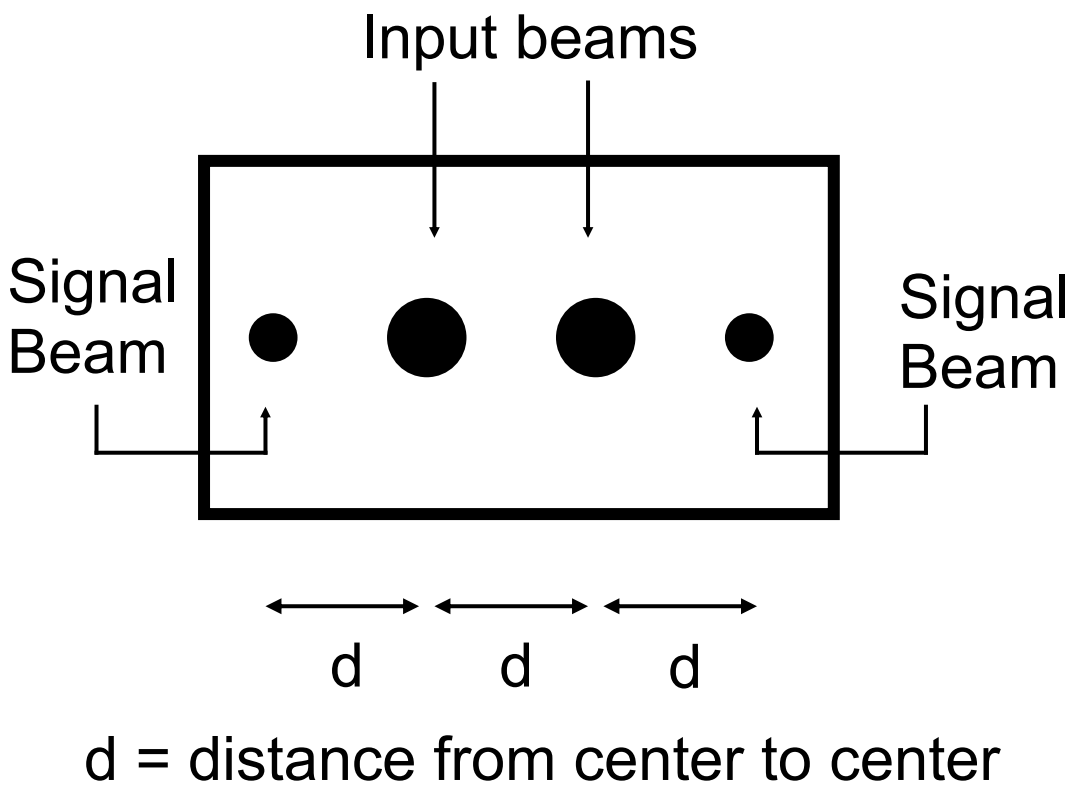

FIGURE 2.4 Beam locations. The beam-center-to-beam-center distance between the signal beam and the input beam is the same as the distance between the two input beams.

$$I_{signal1} \sim (b/8\pi)^2 I^2_{pump} I_{probe} [\lambda^2/\sin^4(\theta/2)](dn/dT)^2 (\alpha^2/K^2)$$

$$I_{signal2} \sim (b/8\pi)^2 I_{pump} I^2_{probe} [\lambda^2/\sin^4(\theta/2)](dn/dT)^2 (\alpha^2/K^2)$$

where b is the path length of the two-laser overlap region, I_{signal} is the strength of the signal beam, I_{pump} and I_{probe} are the intensities of the input beams, λ is the wavelength of the input lasers, θ is the angle between the input beams, dn is the index of refraction, dT is the change in temperature of the medium, α is the absorptivity coeffecient, and K is the thermal conductivity of the medium. The input beam power distribution is usually set for 70:30 between pump and probe input beams. **TABLE 4.2** shows the relative relationship between laser power and signal intensity when all other variables are held constant.

The equations above illustrate the ***properties*** that give DFWM its characteristic ***dependencies***. There is a cubic dependence on laser power and a quadratic dependence on absorption coefficient. Either of these properties can be manipulated to induce dramatic changes in signal with small changes in either laser power or concentration. The cubic dependence of signal on laser power and the quadratic dependence on sample concentration are demonstrated and confirmed here and in other DFWM experiments.

2.6 Advantages of Laser Wave Mixing

Laser wave mixing is a sensitive absorption-based detection method that has several inherent advantages including excellent sensitivity, small sample requirements, short optical path length, high spatial resolution and good standoff detection capability. Wave mixing is inherently suitable for interfacing to

TABLE 2.2 Effect on the signal strength based on laser power distribution between the input beams. Assuming all other factors are constant, a relative signal intensity can be calculated using $I = I^2_{pump} I_{probe}$. The optimal ratio is 65/35; however, the beam splitters available make the 70/30 ratio the best for use in this work.

Laser Power Pump	Laser Power Probe	Relative Signal Intensity
0.20	0.80	0.032
0.25	0.75	0.047
0.30	0.70	0.063
0.35	0.65	0.080
0.40	0.60	0.096
0.45	0.55	0.111
0.50	0.50	0.125
0.55	0.45	0.136
0.60	0.40	0.144
0.65	0.35	0.148
0.70	0.30	0.147
0.75	0.25	0.141
0.80	0.20	0.128

microfluidic systems, capillary chromatography systems, capillary electrophoresis systems and other liquid- and gas-phase flowing systems. The wave-mixing signal is generated instantaneously as the two-input laser beams intersect in the presence of an absorbing medium. Detection sensitivity levels are comparable or better than those of fluorescence-based methods, and yet, wave mixing can be used for both fluorophores and chromophores. This allows the detection of many molecules, including small organic molecules, diatomic gases and large biomolecules in their native form. Since the wave-mixing signal is a coherent laser-like beam, it can be collected against a virtually noise-free dark background. The coherent signal also offers remote standoff detection capability.

REFERENCES

1. Wu, Z.; Tong, WG.;. *Anal. Chem.* **1993**, *65 (2)*, 112-117.

2. Garrucio, A; *Foundations of Physics*, **2004**, 34(2), 198301992.

3. Fisher, RA; *Optical Phase Conjugation*, **1983**, Academic Press, Orlando, FL.

4. Bernath, PF; *Spectra of Atoms and Molecules, 2nd Edition*, **2005**, Oxford University Press.

5. Briggs, RD: *Ph.D. Dissertation*, **2004**, UCSD-SDSU.

6. Simoni, F; Cipparone, G; Duca, D; Khoo, IC: *Optics Letters,* **1991**, 16(6), 360-362.

7. Bernoilles, S: *Ph.D. Dissertation*, **1997**, UCSD-SDSU

8. Wu, Z.; Tong, W. G. *Anal. Chem.* **1991**, *63(18)*, 1943-1946

Chapter 3

Sensitive Standoff Detection of Bromine Using Degenerate Four-Wave Mixing

3.1 Introduction

Degenerate four-wave mixing (DFWM) is a sensitive optical absorption technique used to detect several different gaseous atoms and ions. In our laser research group, Maniaci detected Samarium in the ppb range using an ICP torch [1]; Mickadeit detected Rubidium at the sub parts-per-quadrillion levels in the graphite furnace [2], and Andrews. detected Barium ion in the low ppm range [3]. These previous works all used a three-beam backward-scattering Doppler-free DFWM arrangement. This particular arrangement reduces Doppler broadening, allowing hyperfine and isotopic profiling on atomized samples.

The current work probes the diatomic bromine molecules in the gas phase with some standoff distances. Molecular species typically show broad absorption peaks as compared to those of atomic species, thus, there is no benefit in eliminating Doppler broadening. Previous DFWM work on polyatomic gas-phase samples focused on the study of the physical parameters of DFWM signal generation. Delve modeled the thermal-grating effect [4], Pahkomov studied the power dependence of the DFWM signal in gaseous samples [5], and Ljunberg explored the effects of molecular collisions and temperatures on the DFWM signal [6]. Additionally, Smith investigated the effect of various buffer gasses on the DFWM signal produced by molecular gas samples [7]. These previously

reported works provided some useful information on the characteristics of the DFWM signal from gaseous molecules. Our work presented here focuses on enhanced detection sensitivity levels and standoff detection capabilities of the DFWM method.

Previous DFWM studies on gases operated under low-pressure regimes and only approaching room pressure regimes by backfilling a cell with pure buffer gas. In our work, we detect gaseous molecular species in ambient room-pressure conditions. We use DFWM as a remote detection technique and obtain parts-per-billion levels of sensitivity at distance of a few meters. **TABLE 3.1** compares our laser wave-mixing results to those previously published. This work improves upon the sensitivity levels reported in previously published work while adding a distance component to the detection of gas-phase analytes.

There are two different signal generation mechanisms occurring when working with an analyte gas buffered by an inert gas. At low buffer gas pressure levels (< 100 Torr), the DFWM signal occurs due to a laser-induced population grating. The two input beams form a grating based on constructive and destructive interferences, and these areas of high and low energy modulate the molecules between excited and ground states. The resulting population grating acts to diffract subsequent photons that impinge upon it, creating a DFWM signal beam that can be collected against a dark background. At higher buffer gas pressures, the DFWM signal is due to thermal gratings formed by the excitation and relaxation of molecules in the beam probe. There are three different signal dependencies on buffer gas pressure [4]. At low buffer gas pressures (<10 Torr),

TABLE 3.1 Comparison of detection limits for gas-phase samples.

Gas Analyte	**LOD**	**Method**	**Reference**
I_2	2.6 ppm	DFWM	Appl Opt, 34(18), 3281-3289, 1995
NO_2	12.6 ppm	DFWM	Phys Chem Chem Phys, 2, 5594-5601, 2000
NO_2	12.6 ppm	DFWM	Appl Phys B, 60, 11-18, 1995
NO_2	11.7 ppm	DFWM	Appl Phys B, 54, 271-277, 1992
NO	6.2 ppm	DFWM	Appl Phys B, 63, 69-78, 1996
C_2H_2	6.4 ppm	DFWM	Chem Phys Lett, 233, 525-532, 1995
SF_6	2 ppm	DFWM	Chem Phys Lett, 233, 525-532, 1995
Br_2	1.8 ppb	DFWM	This work

collisional relaxation is slow and signal intensity is independent of pressure. However, as buffer gas pressures increase to greater than 10 Torr, signal intensity has a pressure dependency of p^{-3} until pressures reach to 100 to 150 Torr. From 150 Torr to 1000 Torr, signal intensity shows a quadratic dependence on buffer gas pressure. Dreizler showed that signal intensity peaked around 15 Torr when using a pure ethylene gas [8]. Adding buffer gas to a sample cell containing 4 Torr of ethylene showed a signal increase that began at 100 Torr total pressure, with signal remaining strong beyond 760 Torr [8].

Our work probes bromine gas at a small partial pressure under a total pressure equal to atmospheric pressure, conditions that are similar to those in Driezler's work on ethylene. However, our work presented here differs since we vary the concentration of the analyte gas (molecular bromine) while maintaining a constant pressure of buffer gas (room pressure), rather than the reverse. The purpose of this work is to show that DFWM is an adaptable, sensitive analytical technique for the detection of molecular gas-phase species under ambient conditions with some standoff detection capability.

3.2 Experimental Setup

This work investigates laser wave mixing as a detection technique at different standoff distances. **FIGURE 3.1** shows a typical experimental setup used in this work. For the distances shorter than 1 m (i.e., 0.25, 0.50, 0.75 m), a quartz focusing lens mixes the probe and pump beams in the sample. In order to maintain the proper beam angle relationship as the distance of detection gets

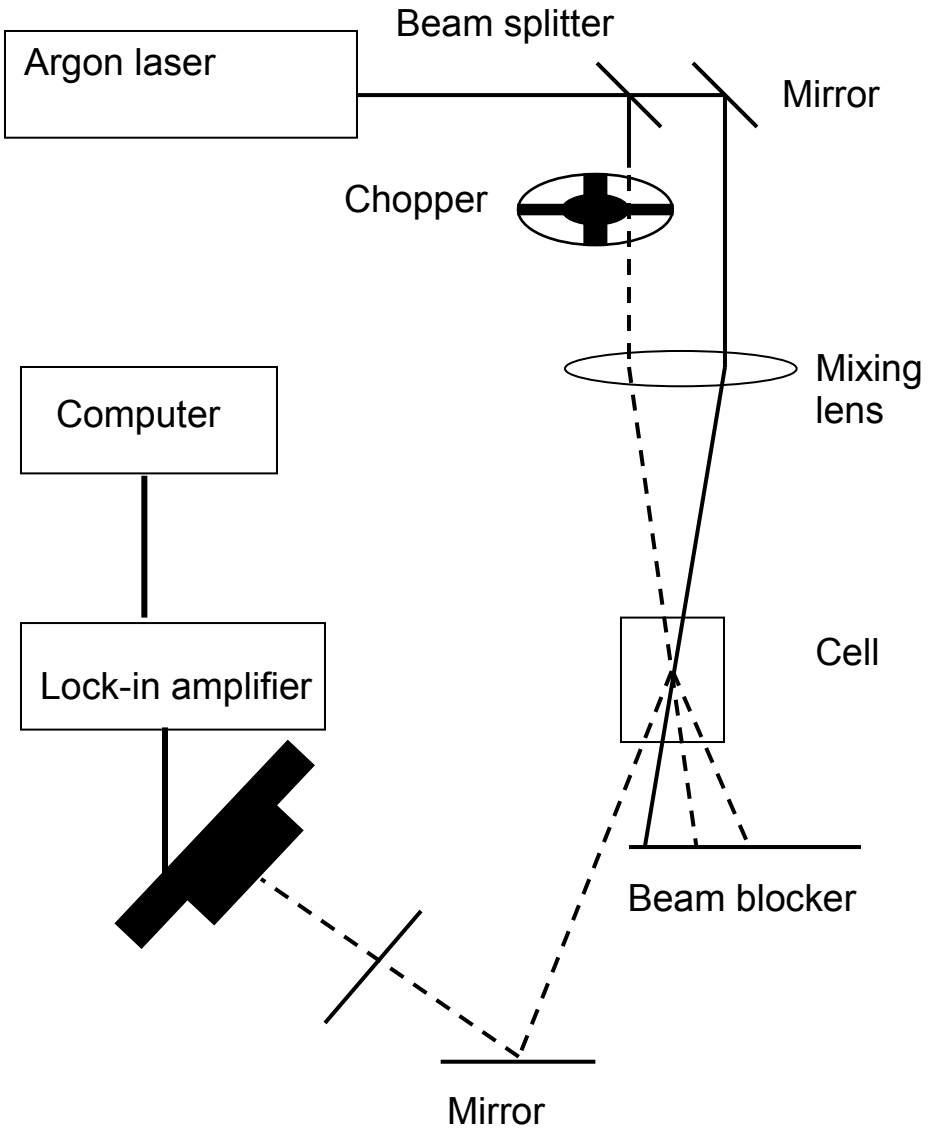

FIGURE 3.1 Laser wave-mixing setup. At distances of shorter than 2 m, the focusing lens mixes the two input beams at the sample, forming the grating for signal generation. At longer distances, the mixing lens is removed and the input beams are allowed to expand naturally.

longer, the two beams move farther apart as the detection length increases and a mixing lens is no longer used. For shorter standoff distances, a mixing lens yields smaller probe volumes and more intense gratings. For longer standoff distances, the beams are not mixed with a lens, resulting in larger beam diameters and probe volumes with lower power density, and hence, yielding reduced detection sensitivity levels at longer distances.

In our setup, an argon ion laser (Coherent Innova 90-6, Santa Clara, CA) is used with the 514 nm output. The laser beam is split by a 70/30 Reflectance/Transmittance beam splitter to form the two input beams, E1 and E2. The reflected beam from the beam splitter, E1, has the higher laser intensity, and therefore, serves as the pump beam and the subsequent probe beam. The weaker transmitted beam, E2, serves as the second pump beam. An optical chopper (Stanford Research Systems, SR541, Sunnyvale, CA) modulates the input beam at 1.3 kHz to help isolate the signal beam and reduce background noise. The chopper is interfaced to a lock-in amplifier (Stanford Research Systems, SR810 DSP, Sunnyvale, CA), which is connected to a computer for data acquisition and display. The two input excitation beams travel equal distances before mixing within the sample cell in a small laser probe volume. The two signal beams, E3 and E4, generated by the interaction of the sample with the two input beams, propagate in the forward direction.

FIGURE 3.2 shows the input beams (E_1 and E_2) and their propagation in the forward direction with an angle between the signal and the input beam equals to that between the two input beams. These signal beams(E_3 and E_4) are

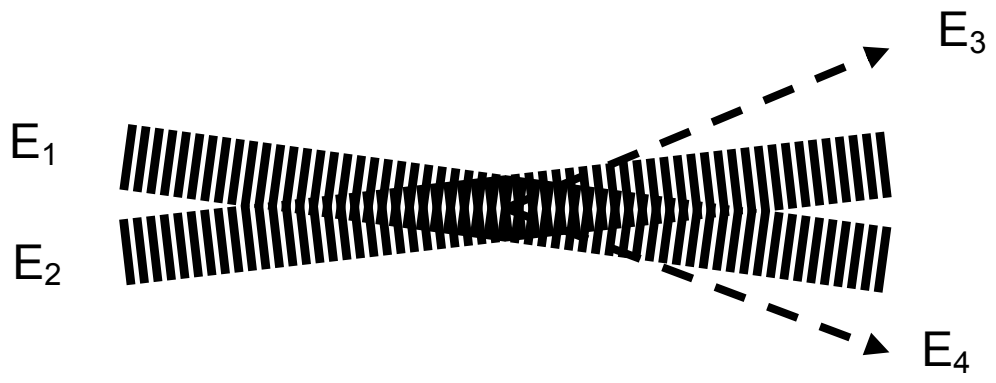

FIGURE 3.2 The laser probe volume inside the grating and the propagation directions of the two signal beams.

coherent laser-like beams and the stronger of the two signal beams, E3, is directed into a simple photodiode detector (ThorLab, PDA55, Newton, NJ) after passing through spatial filters and a focusing lens. The wave-mixing sample cell is a 10 cm x 2.54 cm cylindrical Quartz cell (Starna, Atascadero, CA) with a single resealable frosted glass injection port containing a small amount of bromine gas at room pressure. A diagram of this cell is shown in **FIGURE 3.3**. The cell produces scattered light that is present in all cases. This noise is subtracted from the raw data of the bromine gas samples.

Bromine liquid has a high vapor pressure, and hence, it is difficult to introduce small quantities into the gas cell. To counter this problem, liquid bromine is diluted in methylene chloride to the desired injection concentration. The mixture is introduced into the gas cell using a standard pipette (0.5 to 10 μL). The sample is allowed to sit for ten minutes, so that bromine and methylene chloride can reach concentration equilibrium in the cell. When calculating the concentration of the analyte in the cell, bromination of methylene chloride is a possibility; however, this reaction occurs only at high temperatures in the presence of HBr [9]. Thus, this is not a concern for this experimental setup.

Molecular bromine dissociates in the presence of light. McAfee reported that light of 510.7 nm dissociates Bromine [10]. They examined the excitation and subsequent fluorescence decay using a 514.5 nm argon ion laser and reported no dissociation at this wavelength. Seery and Britton note that discrete absorption of bromine begins at 512 nm [12]. Additionally, Tech [11] found no lines in the Br I atom at 514.5 nm, the chosen wavelength of our argon ion laser.

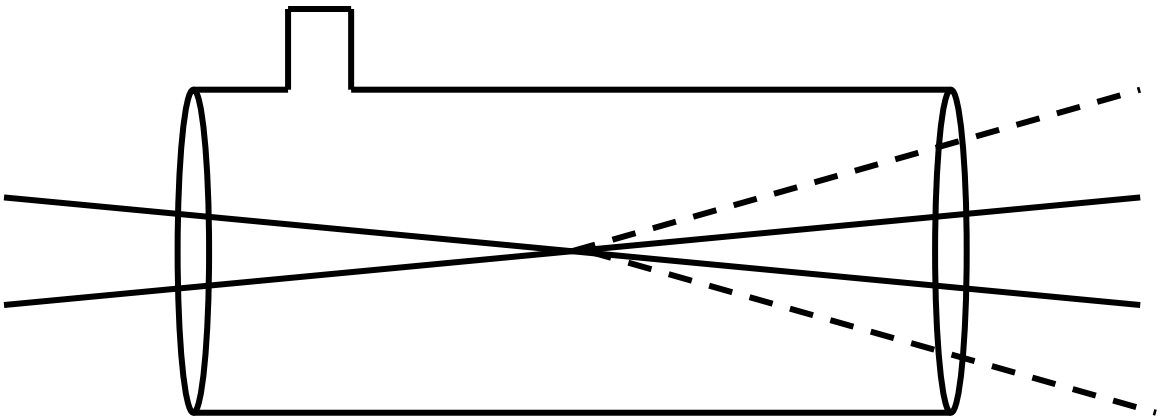

FIGURE 3.3 Gas cell with UV-transparent Quartz windows. Analyte samples with known concentration levels are introduced through the inlet and then sealed using a removable cap.

Thus, we are certain that the molecule probed is diatomic bromine and not atomic bromine (Br I).

UV-visible absorption spectra are used to help identify appropriate laser wavelengths for probing the bromine analyte. All UV-visible absorption work is performed on a bench top UV-visible spectrophotometer (Hewlett Packard, 8452A) using a standard Quartz cuvette with 25 □L of bromine. Thus, the cell is a saturated system that has come to a dynamic equilibrium between the gas and liquid states of bromine. This portion of the work follows the procedures outlined by Seery [12] with some modifications. Seery and Britton used a sealed 10 cm cell with millimolar amounts of bromine contained within the cell, whereas this work uses a 1 cm cell with a saturated headspace above the bromine liquid.

We investigated several analyte cell designs before settling on the cylindrical gas cell. Our initial flowing analyte cell consists of different cell systems attached to a two-way circulating air pump that moves bromine through the cells. This flowing sample system yields some signal and S/N instability levels and the pump could be easily contaminated by bromine gas. On the other hand, an airtight static cell yields better S/N and one can control the trace-concentration levels of bromine more accurately. Different static cells are tested including a 1 cm cuvette, a 20 mL scintillation vial, a capped 60 mL Erlenmeyer flask and NMR tubes. These sample cells have significant optical background noise levels resulting from scattering off poor optical quality glass used to construct these cells. Thus, a 10-cm cell with Quartz optical windows is custom designed and used as an analyte cell for our work.

3.3 Results and Discussion

A UV-visible spectrum is measured first to identify the largest absorption peak using a Quartz cuvette with liquid bromine at the bottom and the bromine vapor above the liquid, as shown in **FIGURE 3.4**. Molecular bromine has a broad peak from 400 nm to 600 nm with maximum absorption near 425 nm. We test the 514.5, 488.0, 476.5, and 454.6 nm wavelengths of the argon ion laser as an excitation source. As shown in **FIGURE 3.5,** the DFWM signal at 514.5 nm is greater than those generated by the other argon ion laser wavelengths, even though the 514.5 nm wavelength is not as close to the bromine absorption maxima as compared to other wavelengths. Given the cubic dependence on laser power and the quadratic dependence on absorptivity exhibited by laser wave mixing, it would be expected that each of the other three wavelengths would have resulted in a larger signal. However, the observed behavior runs counter to expectations. The other three argon ion laser wavelengths, 488.0 nm, 476.5 nm and 454.6 nm, all yield higher energy than the 510 nm dissociation limit of the bromine molecule, and hence, it is possible, though not studied in this work, that the higher energy beams are dissociating the bromine molecules, thus significantly reducing the population available to generate the DFWM signal. Thus, the 514.5 nm wavelength is used to excite the analyte in this work.

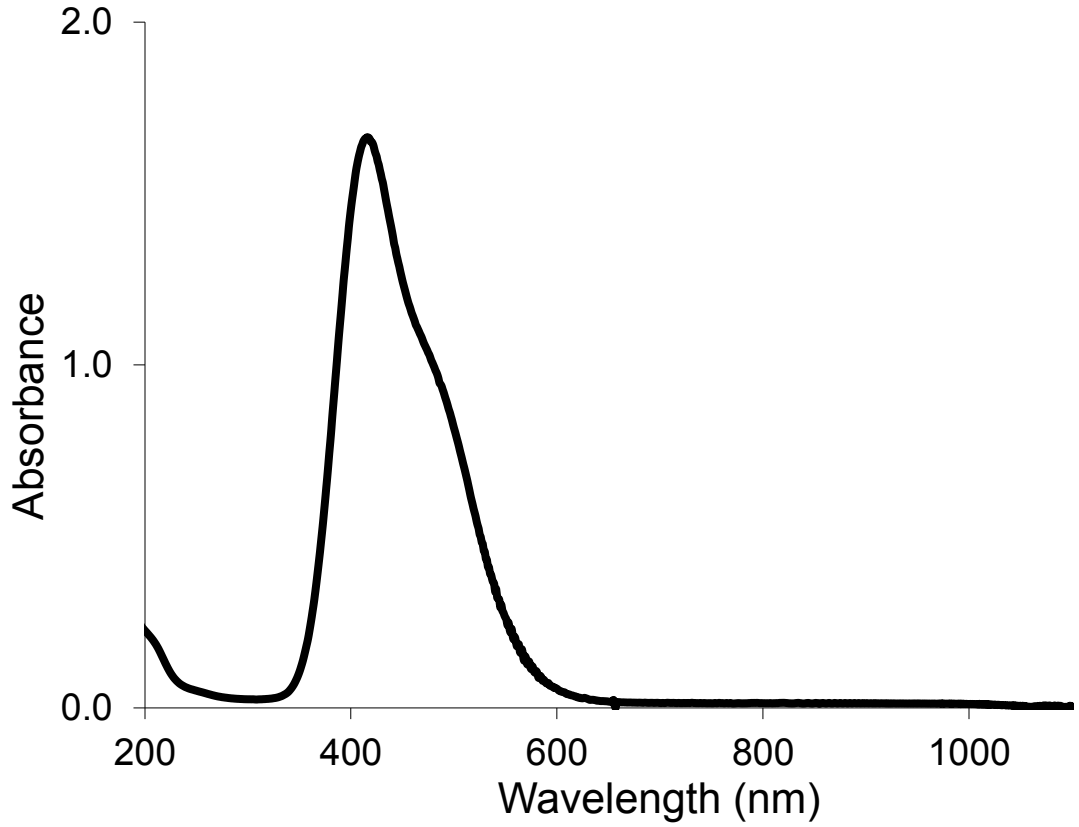

FIGURE 3.4 UV-visible absorption spectrum of bromine vapor. A 1-cm Quartz cuvette is charged with a small amount of liquid bromine at the bottom and then the cuvette is sealed with a Teflon cap and Parafilm. The spectrophotometer analyzes the bromine vapor above the liquid deposited.

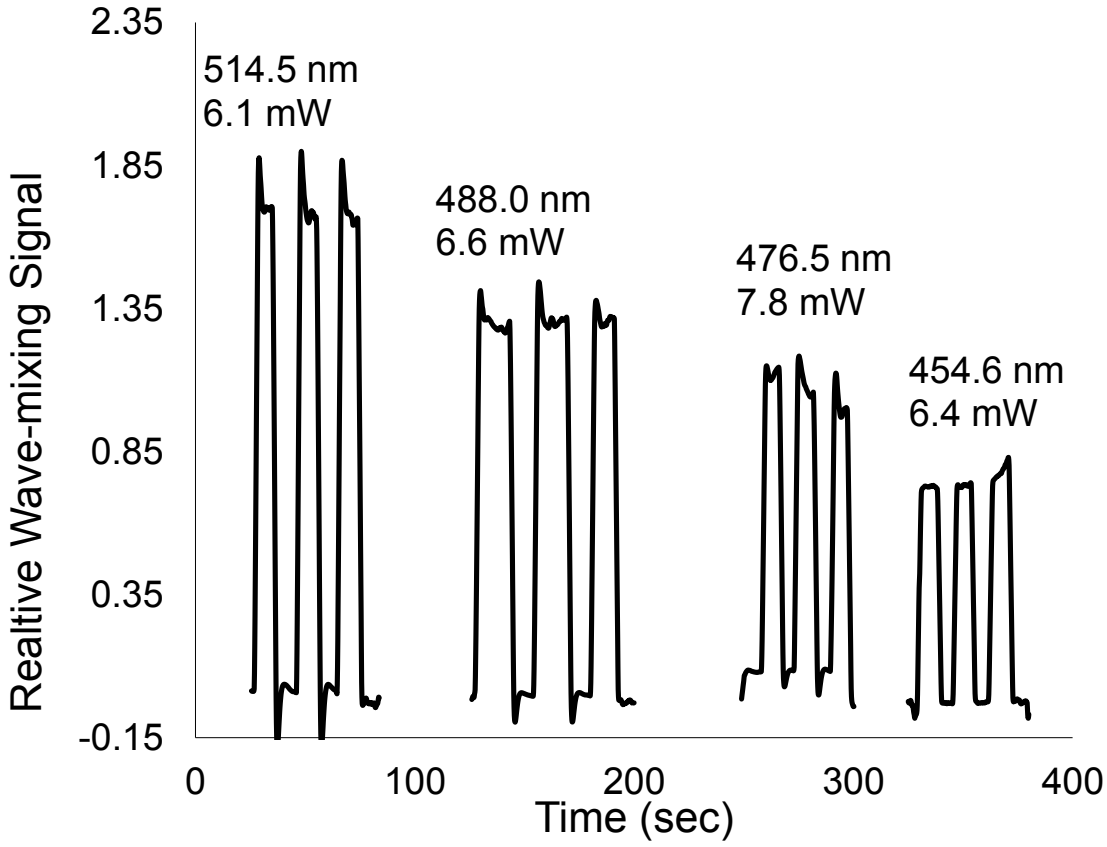

FIGURE 3.5 DFWM signal strengths at different argon ion laser wavelengths (seven-point moving average).

An essential property of laser wave mixing is its cubic dependence on laser power. This work exhibits a cubic or near dependence on laser power at all distances investigated. **FIGURE 3.6** shows experimental confirmation of the cubic dependence of signal on laser power at 25 cm. **FIGURE 3.7** shows the cubic power dependency at 2 m. In both cases, the relationship is nearly cubic. Small deviations from the ideal cubic relationship are observed since there is a small, consistent amount of noise due to the sample cell used. After confirming the DFWM signal based on cubic dependence on power or quadratic dependence on concentration, the detection sensitivity limits at different distances are determined. Previously reported works on bromine only used detection distances in the centimeter scale and our work demonstrates DFWM standoff detection distances in the meter scale. This inherent advantage of DFWM in detecting trace chemicals at good standoff distances promises a wide range of potential applications including detection of explosive and environmentally important chemical and biological agents in the gas phase.

FIGURES 3.8 shows the detection sensitivity level achieved at the detection distance of 75 cm using a mixing lens and **FIGURE 3.9** shows the sensitivity level at 2 m without using a mixing lens. Preliminary detection limits of 169 ppb, 26 ppb, 12 ppb, 2 ppb, 3ppb and 38 ppb are determined at 0.25 m, 0.5 m, 0.75 m, 2 m, 4 m and 6m, respectively. The detection sensitivity levels indicate that DFWM is more sensitive at longer standoff distances as compared to other detection methods. In all cases, the blank signal is subtracted from the total signal detected for bromine gas samples. Detection limits improve mostly

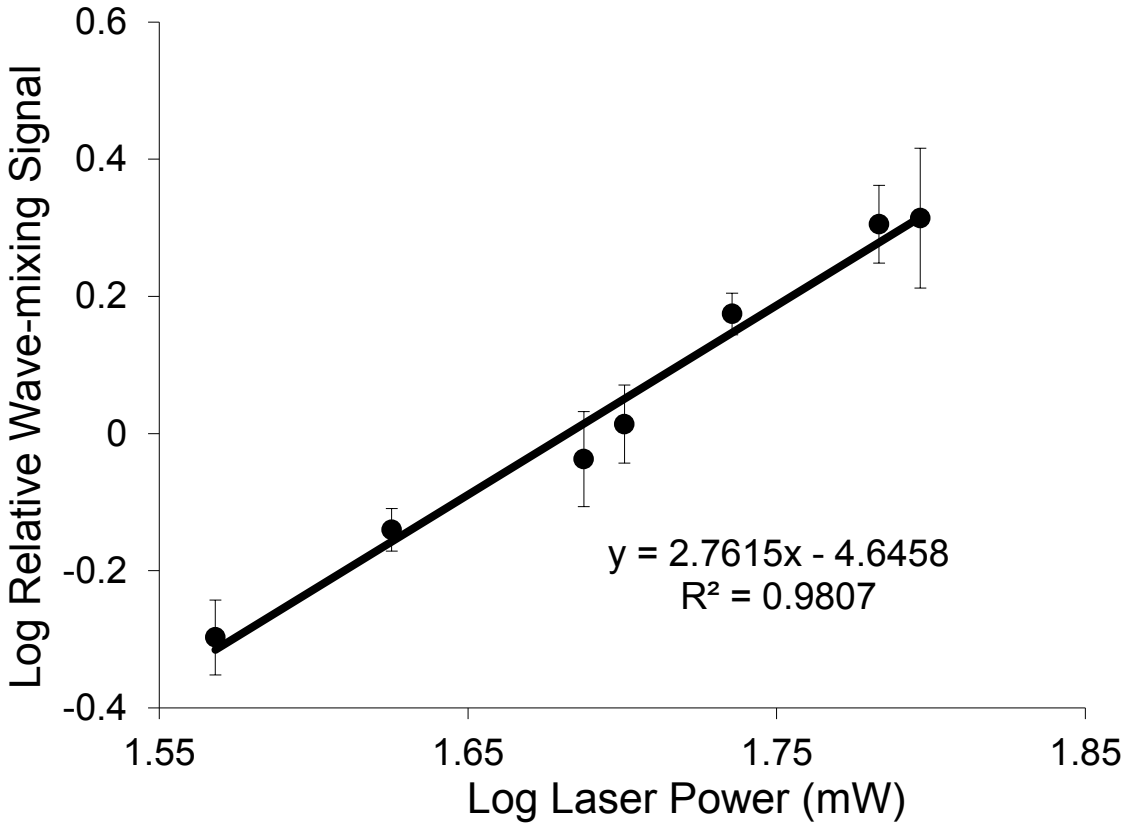

FIGURE 3.6 Cubic dependence of DFWM signal on laser power at 25 cm distance.

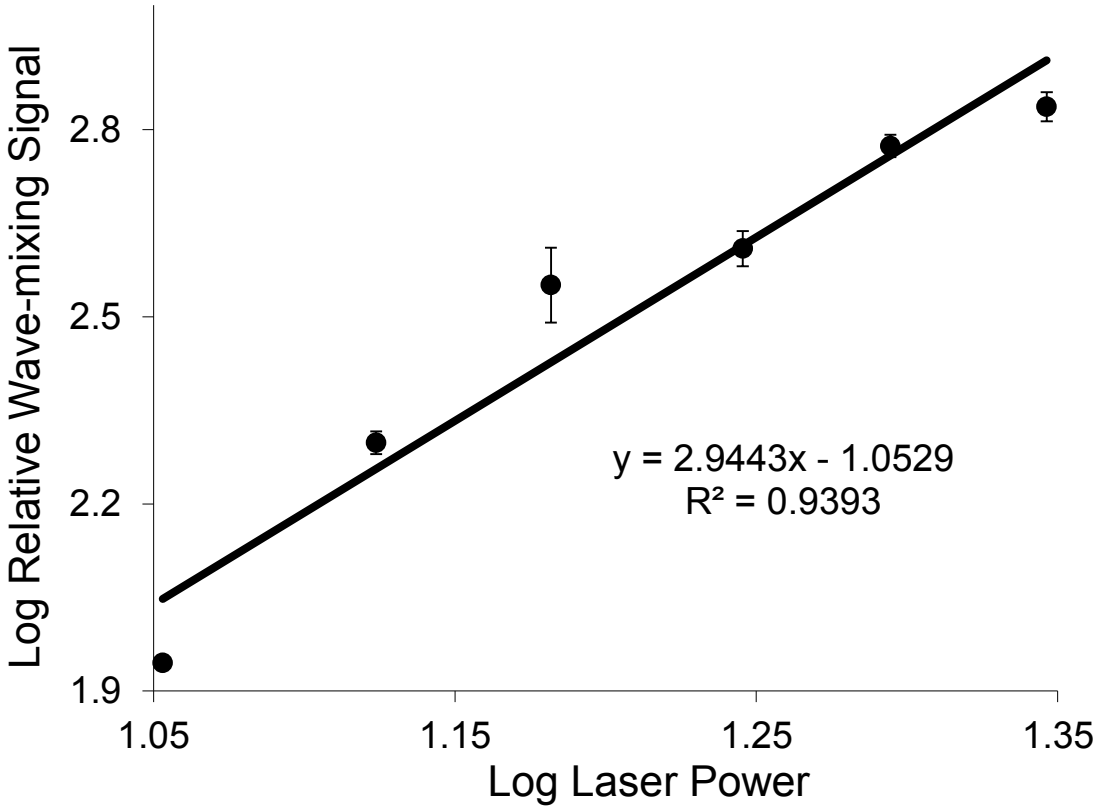

FIGURE 3.7 Cubic dependence of DFWM signal on laser power at 2 m distance.

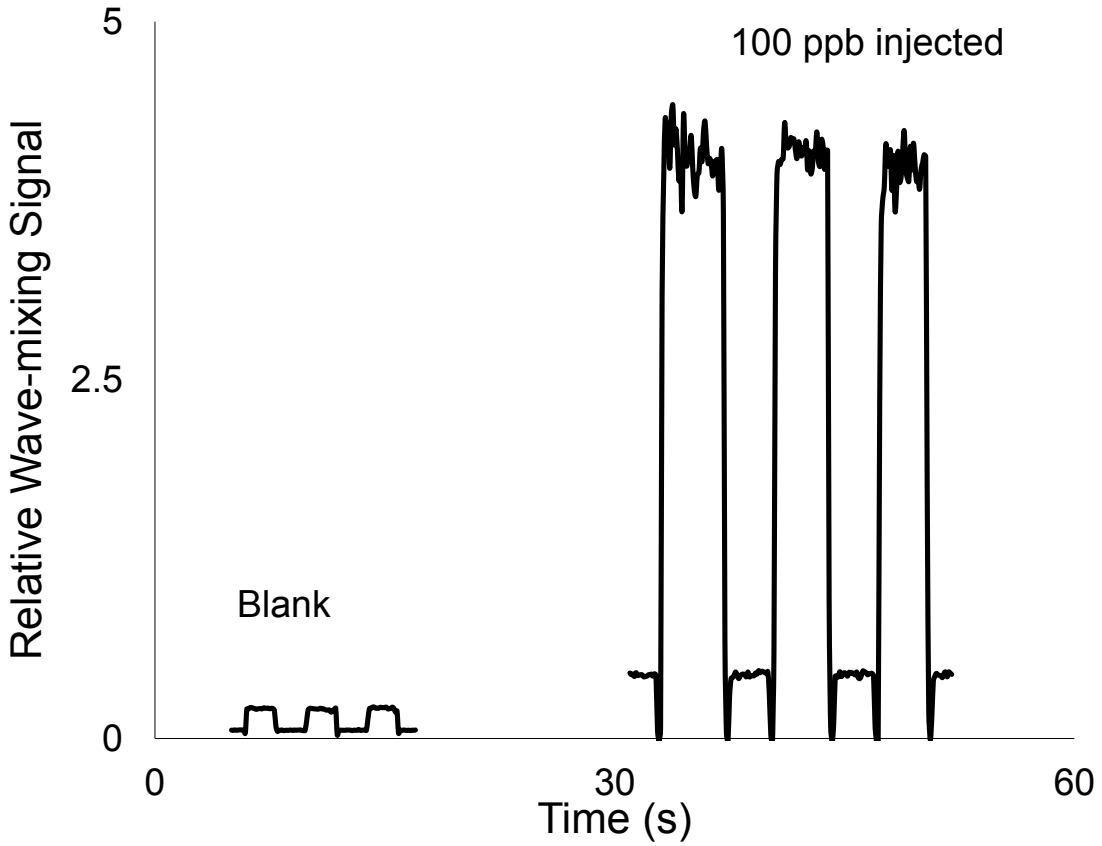

FIGURE 3.8: Detection sensitivity at a distance of 75 cm (100 ppb injected, 12 ppb LOD).

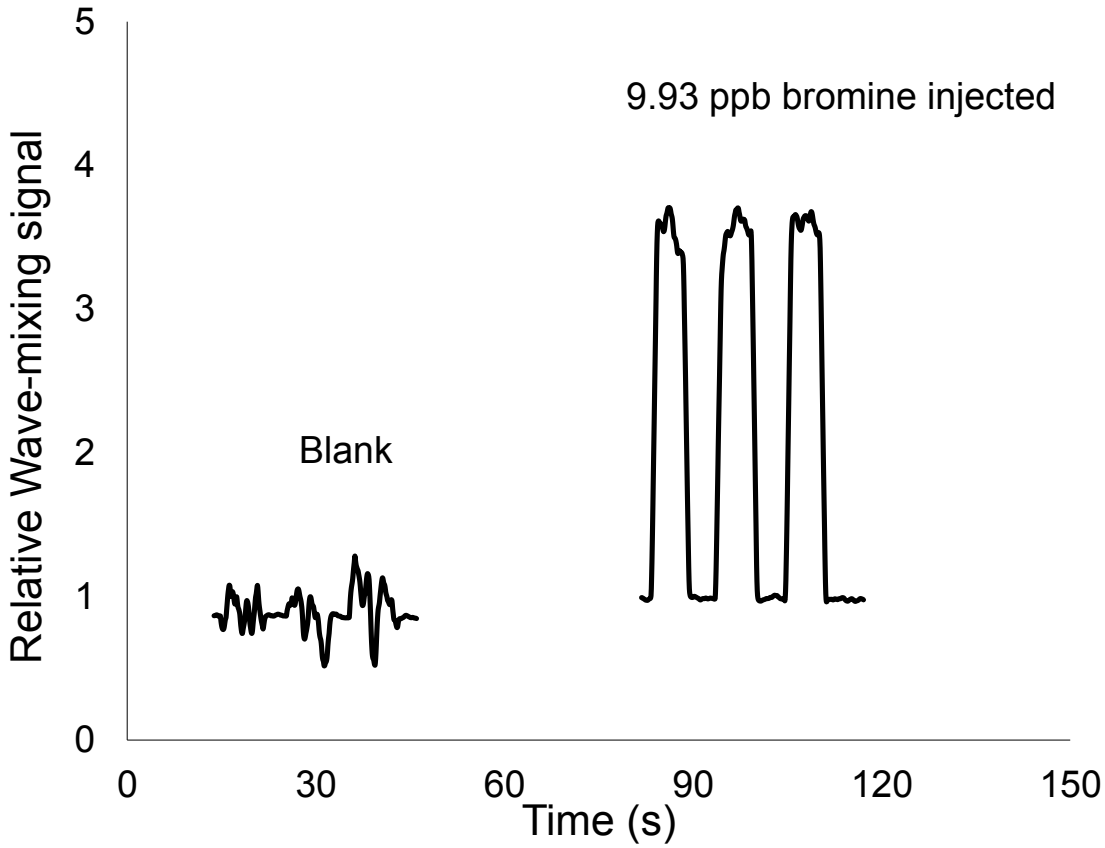

FIGURE 3.9 Detection sensitivity at a distance of 2 m (9.9 ppb injected, 1.5 ppb LOD).

as the distance is increased, likely due to the increase in the probe volume as the distance is increased. As the distance from the lens to the mixing region increases, beams E_1 and E_2 overlap for longer lengths. Thus, each distance of detections has a larger probe volume. The advantage of a larger probe volume is that the probe holds more analyte molecules. At the longest distance tested, the beam diameter is nearly 5 mm wide (i.e., lower laser power density) and the beam shows more flaws in its TEM profile. Hence, the DFWM grating is not as sharp and the resulting signal is not as strong.

The limits of detection are calculated based on the concentration extrapolated to the S/N of two. First, the net signal amplitude is determined, i.e., signal minus background, and then the noise level is determined, i.e., standard deviation of the signal. Once the S/N is determined, the limit of detection for nonlinear DFWM detection is estimated using the following equation;

$$\text{LOD} = \text{Sample Concentration } (\text{SQRT } (2/(\text{S/N}))$$

Our preliminary results compare favorably, both in terms of limits of detection and standoff distances, to other optical methods for gas-phase analytes.

3.4 Conclusions

Nonlinear laser wave mixing is a sensitive optical absorption technique for standoff detection of gaseous molecular bromine. This work shows that wave

mixing can be adapted to detect gaseous molecules under room temperature and pressure conditions without using atomizers such as inductively coupled plasma or a hollow cathode discharge plasma cell. Diatomic bromine has a broad absorption peak, thus Doppler broadening is not a concern as it is in atomic spectroscopy and given the fixed wavelength nature of the laser, we use the simpler two-beam forward-scattering optical setup instead of a complex three-beam Doppler-free backward-scattering optical arrangement. This work demonstrates that even at long distances laser wave mixing provides excellent ppb-level detection limits for gas-phase samples at room conditions

REFERENCES

1. Maniaci, MJ; Tong, WG: *Spectrochimica Acta Part B*, 2004, 59, 967-973.

2. Mickadeit, FK; Berniolles, S; Kemp, HR; Tong, WG: *Analytical Chemistry*, **2004**, 76, 1788-1792.

3. Andrews, JM; Weed, KM; Tong, WG: *Applied Spectroscopy*, **1991**, 45, 697-700.

4. Delve, PA; Whitaker, BJ: *Physical Chemistry Chemical Physics*, **2000**, 2, 5594-5601.

5. Pakhomov, A; Chung-Jen, W; Yit-Song, C; Lin, HS: *Physical Review A*, **1997**, 55(4), 3086- 3091.

6. Ljunberg, P; Axner, O: *Applied Physics B,* **1996**, 63, 69-78.

7. Smith, AP; Hall, G; Whitaker, BJ; Astill, AG; Neyer, DW; Delve, PA: *Applied Physics B*, **1995**, 11-18.

8. Dreizler, A; Dreier, T; Wolfrum, J: *Chemical Physics Letters*, **1995**, 233, 525-532.

9. [1989 Patent GB-1989-25012 Patent SU-1982-3524010],

10. McAfee, KB; Hozack, RS: *Journal of Chemical Physics*, **1976**, 64(6), 2491 – 2495.

11. Tech, JL; *Journal of Research of the National Bureau of Standards A). Physics and Chemistry*, **1963**, 67A (6)**,** 505-554.

12. Seery, DJ; Britton, D: *Continuous Absorption Spectra of Halogens and Interhalogen Compounds*, **1964**, 68(8), 2263-2266.

Chapter 4

Detection of Trinitrotoluene Using Degenerate Four-Wave Mixing

4.1 Introduction

Trinitrotoluene (TNT) saw wide use as a military explosive beginning with the Russian-Japanese war of 1905 [1], and ever since, the need for sensitive and reliable detection of TNT has arisen in numerous areas. Land-mine detection, improvised explosive device (IED) detection, munitions plant environmental remediation, post-blast forensic investigations and homeland security applications all require reliable, fast and sensitive detection methods. Currently, there are dozens of different methods for detecting trace amounts of TNT in different sample matrices including HPLC [2], capillary electrophoresis [3], chemical complexation [4], reduction [5], chemical degradation [6], fluorescence [7, 8, 9], fluorescence quenching [10, 11], photoluminescence quenching [12], immunoassay [13, 14], mass spectrometry [15, 16] and surface plasmon resonance [17].

Degenerate four-wave mixing (DFWM) is a simple, yet extremely sensitive absorption method that can be easily adapted for TNT detection. As shown in **TABLE 4.1,** laser wave mixing compares favorably too many other methods. Most of the other methods require the use of a fluorophore, a label, an antibody, a separation method or pre-concentration steps. The complexation reaction used in this work is a simple one-step reaction with a short incubation time. When coupled to a DFWM detection setup, it yields excellent detection sensitivity levels.

TABLE 4.1 Laser wave-mixing detection sensitivity compares favorably to other detection methods including immunoassay-based systems.

Method	Current LOD
Absorption	
EPA Method 8330	4-14 ppb in water
	0.25-1 ppm in soil
Chemical Complexation	TNT 0.72 ppm DNT 2 ppm
SPE-CE	TNT 0.34 ppb
	TNB 0.25 ppb
	Tetryl 0.19 ppb
Fluorescence	
Fluorescence Quenching	TNT 71 ppb
MEKC-LIF	TNT, DNT, TNB, DNB 1 ppm
Fluorescent Polymers	TNT sub fg
High Speed Fluorescence Detection of Vapor	DNT 23 ppb
	DNB 80 ppb
Immunoassay	
Cont. Flow Immunosensor (Fluorescence)	TNT low ppb
ELISA	TNT I_{50} 0.4 ppb
Evanescent Fiber Optic Biosensor	TNT 10 ppb
Competitive Immunoassay	TNT and RDX 5 ppb
Other	
Thermal Desorption GC	1 ppm for all explosives in EPA 8905 cal mix A
Surface Plasmon Resonance	TNT 0.09 ppb
This Work	
Laser Wave Mixing	TNT 0.516 ppt

In a laser wave-mixing setup, two identical input beams interact in a nonlinear fashion to produce a coherent signal beam. The coherence of the signal beam affords laser wave-mixing detection methods much better detection sensitivity levels as compared to those of incoherent optical methods such as fluorescence. The bright signal beam is collected against a dark background (unlike absorption-based techniques). Further, the signal has a quadratic dependence on analyte concentration [18], and hence, DFWM offers inherent advantages as a sensor where a large signal change is observed with a small change in chemical properties.

4.2 Experimental Setup

The DFWM experimental setup used in this work is similar to that described in Chapter 3. The input laser is an argon ion laser (Coherent, Innova 90-6, Santa Clara, CA) tuned to generate the 514.5 nm output wavelength. The laser beam is split by a 70/30 Reflectance/Transmittance beam splitter in order to form two beams, E1 and E2, and E2 is modulated by an optical chopper (Stanford Research Systems, SR541, Sunnyvale, CA) at 400 Hz. The chopper is interfaced to a lock-in amplifier (Stanford Research Systems, SR810 DSP, Sunnyvale, CA), which is connected to a computer for data acquisition and display.

A flexible fused silica capillary tube (Polymicro Technologies, Phoenix, AZ) is used as our sample holder and detector after removing a small section of the polyimide coating around the capillary so that the laser beams can penetrate

the 150 μm i.d. capillary detector cell. The analytes are introduced through the capillary using a syringe pump (New Era Pump Systems, Dual NE-1000, Farmingdale, NY). The signal from the lock-in amplifier is digitized using a data acquisition program, AIDA, developed by William Tong. A UV-visible spectrophotometer (Hewlett Packard, 8452A) equipped with a Quartz cuvette is used to measure absorption spectra to assure analyte purity.

A stock TNT solution of 2 μg/mL concentration is prepared in acetonitrile (Accustandards, New Haven, CT) and a 1 mL aliquot of the analyte is mixed with a molar excess of 1M NaOH and incubated at room temperature. We use a modified version of Janowsky reaction [4], substituting acetone with acetonitrile to form a carbanion. The reaction of trinitrotoluene with carbanion forms the colored complex, in which the carbanion fits on the ring between two of the nitro groups, as shown in **FIGURE 4.1.** A 1-cm Quartz cuvette serves as the sample holder for all UV-visible absorption measurements and a 150 μm i.d. hollow capillary serves as the flow cell for all laser wave-mixing measurements.

4.3 UV-Visible Absorption Spectra

A simple UV-visible spectrophotometer is used initially to monitor the reaction of trace amounts of TNT and acetonitrile and to ensure and confirm the shape of the expected spectra, reagent concentration parameters, and reaction time parameters. **FIGURE 4.2** shows the UV-visible absorption spectra of TNT and the TNT complex formed in the reaction used in this work. The TNT spectrum shows no absorption in the visible region and strong absorption in the

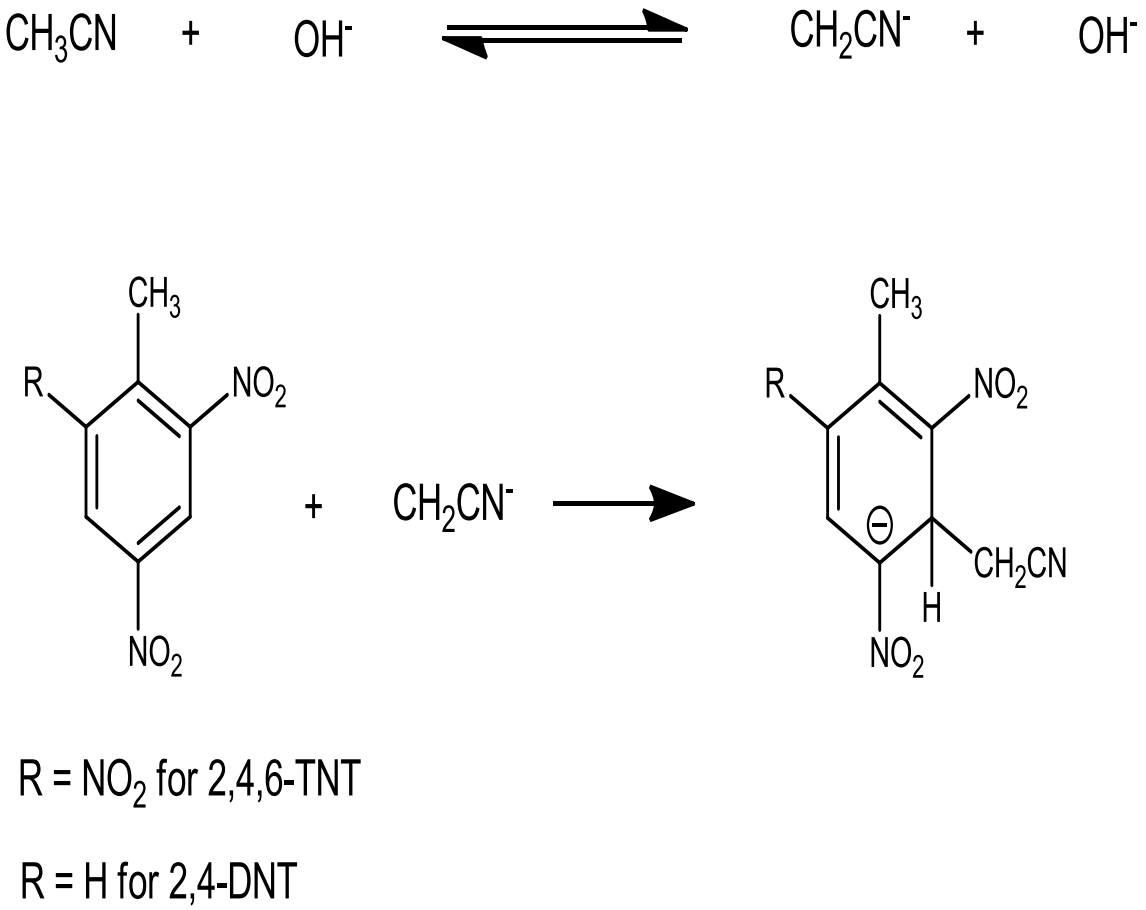

FIGURE 4.1 A colored TNT complex is formed using acetonitrile instead of acetone for Janowsky complex [Jenkins, T.F.; Walsh, M.E. *Talanta.* **1992,** 39(4), 419-428]. The strong base generates an acetonitrile carbanion that attaches to the ring in the 3 position, yielding a complex that absorbs at 524 nm.

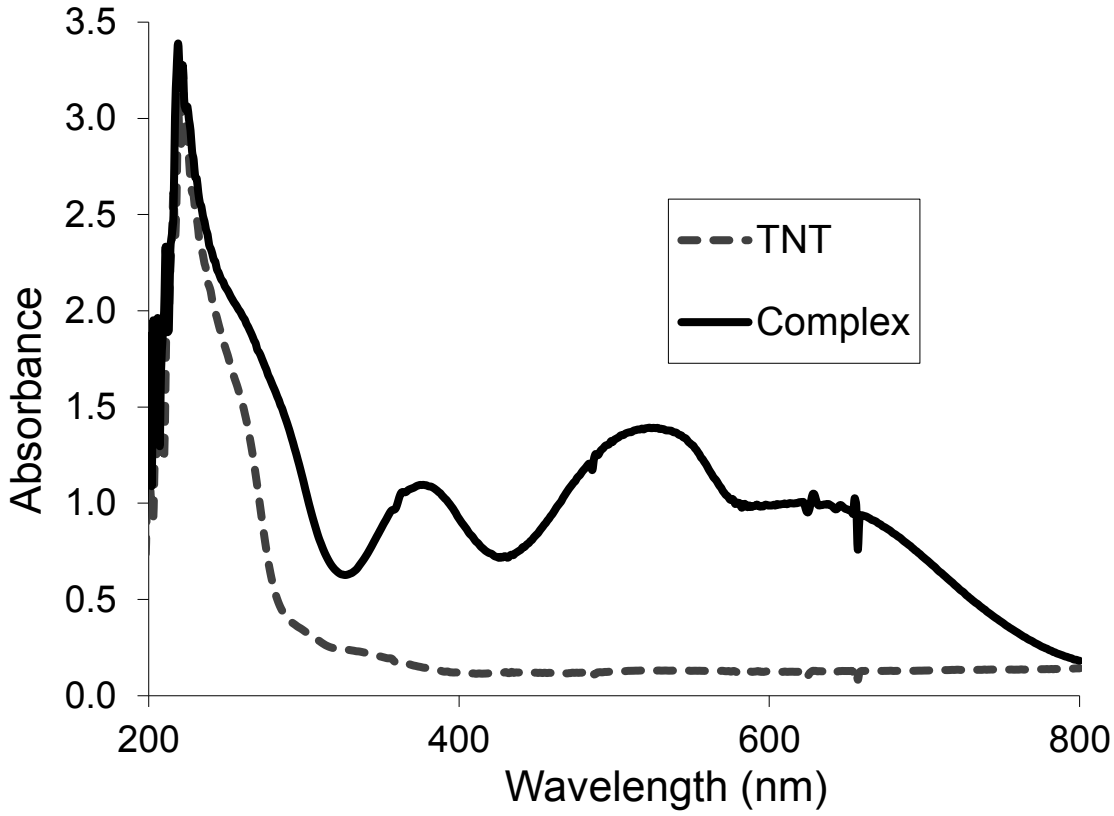

FIGURE 4.2 Comparison of UV-visible absorption spectra of native TNT and Janowsky TNT complex. The TNT complex absorbs at 523 nm and a 514 nm argon ion laser is used to excite the analyte to generate the wave-mixing signal.

UV region (this absorption is non-specific as many organic molecules absorb in this region). The acetonitrile/TNT complex shows a large absorption peak that spans from 425 nm to 600 nm with a maximum absorption at 523 nm. The acetone/TNT complex spectrum has a maximum absorption at 540 nm, as reported previously [4]. Our acetonitrile/TNT complex peak at 523 nm (acetonitrile carbanion added to TNT) is not far from their acetone/TNT peak at 540 nm (acetone carbanion added to TNT). Our argon ion laser excitation wavelength at 514 nm adequately matches our analyte peak at 523 nm.

The complex formation reaction, as described by Jenkins and Walsh, used Na_2SO_3 in NaOH to form the colored complex [4]. Sulfite can also be added to the aromatic ring of TNT to from a more stable complex that retains its color for more than 6 hours as compared to approximately 30 minutes without using sulfite [4]. For our TNT/acetonitrile complex, a time dependent study is performed to determine the incubation time needed to reach reaction completion by monitoring the time needed for the reaction to yield the maximum UV-visible absorption at 523.

FIGURE 4.3 shows a time-dependent trace for 40 µg/mL TNT in acetonitrile using 100 µL of 1 M NaOH and 100 µL of 1M Na_2SO_3 (excess amounts of reagents). The time to reaction completion is determined to be greater than 12 minutes. Given that Na_2SO_3 is a stabilizing agent, the next step is to form the complex using only 100 uL NaOH. **FIGURE 4.4** shows the reaction time required for the same reaction without using Na_2SO_3. The reaction

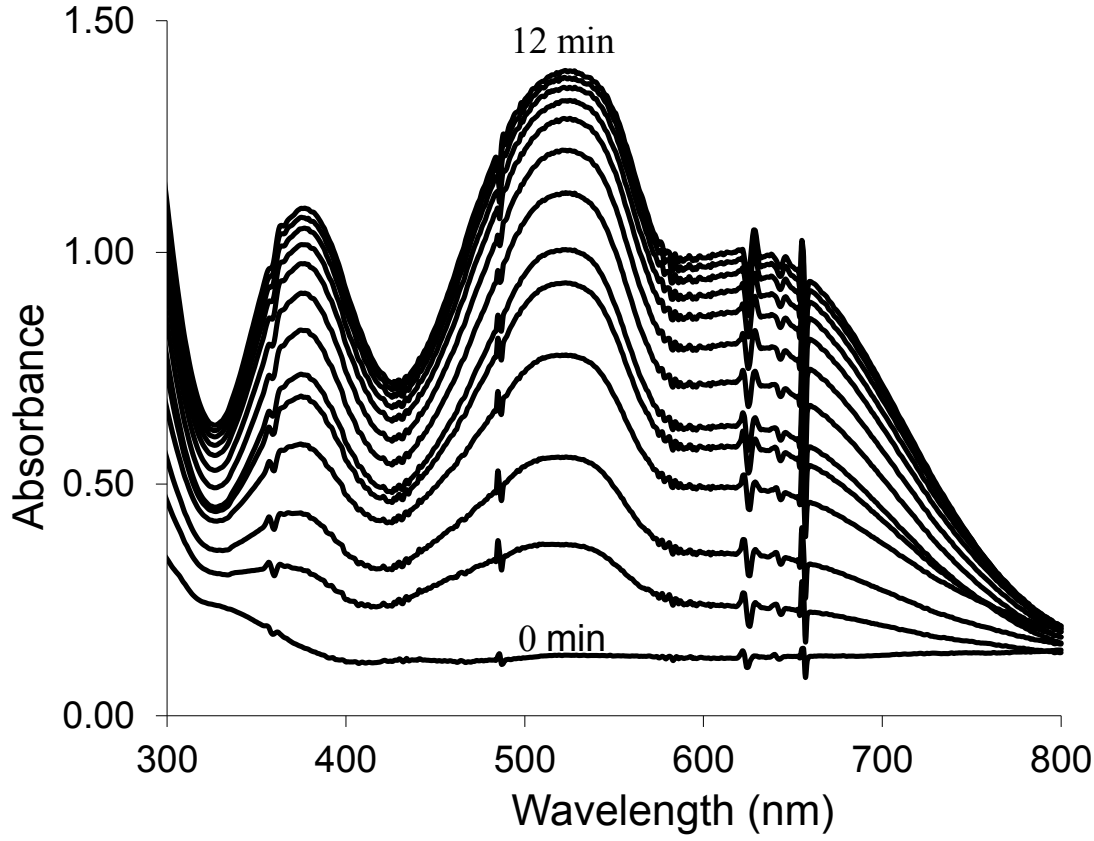

FIGURE 4.3 Reaction-time studies for TNT in acetonitrile using 100 uL of 1 M NaOH and Na_2SO_3. The reaction completion time is determined to be 12 minutes. An absorption spectrum is recorded every minute.

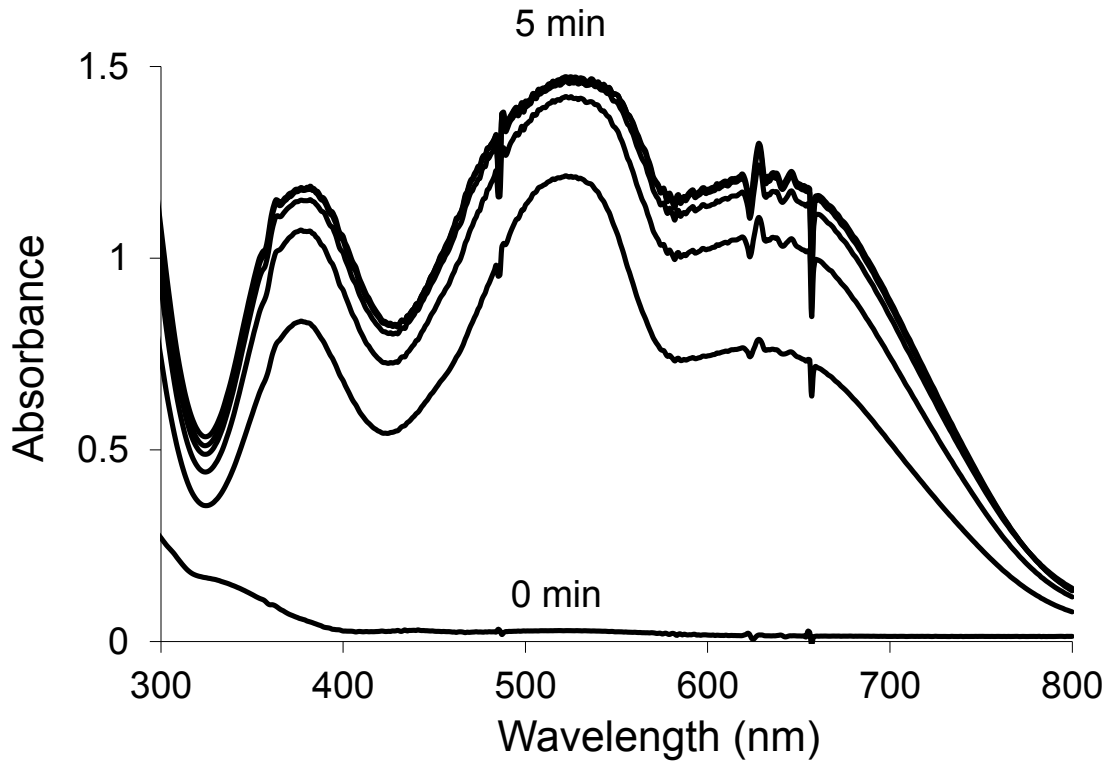

FIGURE 4.4 Reaction-time studies for TNT in acetonitrile using 100 uL of 1 M NaOH only. The reaction completion time is determined to be 5 minutes. An absorption spectrum is recorded every minute.

proceeds to completion much more quickly, taking 5 minutes rather than 12 or more minutes required for the reaction with Na_2SO_3.

FIGURE 4.5 shows comparison of UV-visible absorption spectra of the reaction mixtures with and without Na_2SO_3**.** Both the magnitude of the absorption peaks at 523 nm and the similarity of the spectra across the full wavelength range indicate that Na_2SO_3 does not enhance absorption or change the spectral characteristics of the complex formed. However, the reaction with Na_2SO_3 is much slower than without Na_2SO_3 (12 minutes vs. 5 minutes). The decrease in time to reaction completion coupled with the fact that sample analysis occurs well within the reported 30-minute stability period suggests that the limited stability period of the complex is not a problem. Thus, Na_2SO_3 is not used in the reaction for this work.

The amount of 1M NaOH needed is also determined experimentally. **FIGURE 4.6** shows the comparison of three different amounts of 1M NaOH (25, 50, 100 µL) across six different TNT concentration ranges (1, 2.5, 5.0, 10.0, 20.0, and 40.0 µg/mL). In all cases except the 40 µg/mL sample, the amount of NaOH does not have a significant effect on the absorption measured at 523 nm. It is determined that 25 µL of NaOH is sufficient for the reaction.

UV-visible absorption spectra are used to confirm and determine the parameters of complex formation before wave-mixing detection. The use of acetonitrile produces a colored complex with a similar, but not identical, absorption spectrum compared to that of the acetone complex, as reported previously [4]. A significant decrease in reaction time is observed when the

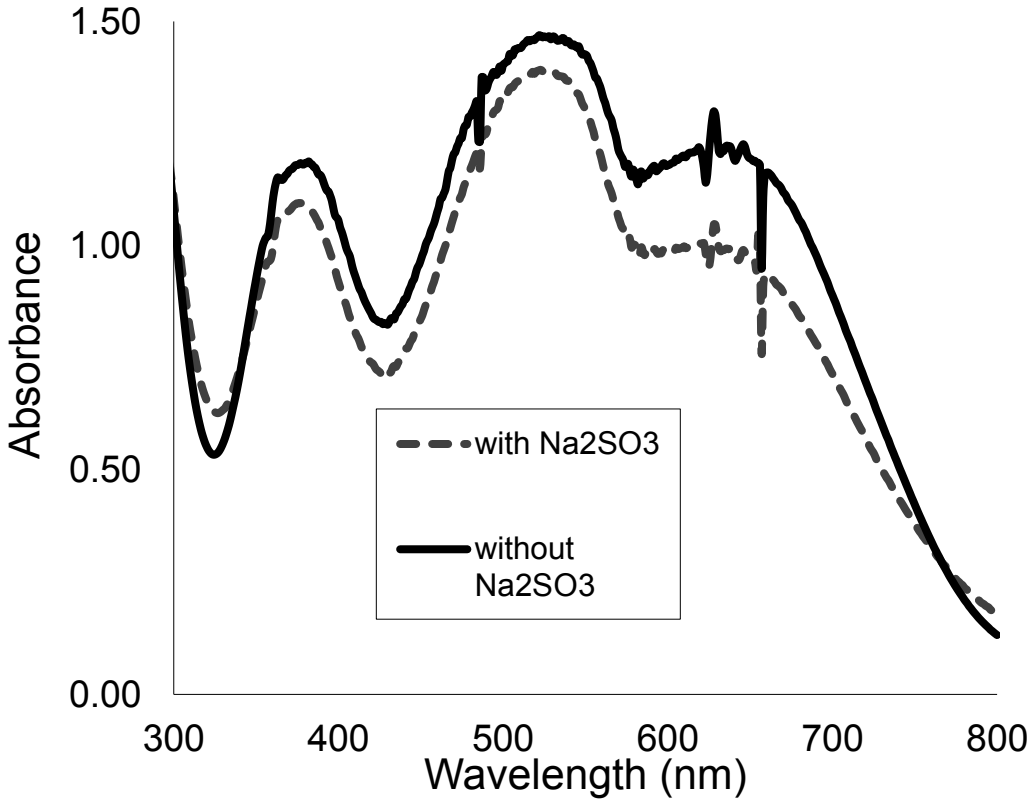

FIGURE 4.5 Comparison of UV-visible absorption spectra of 40 ug/mL TNT using two different reaction schemes. The difference in absorbance at 523 nm is small, and hence, the reaction is simplified by not adding Na_2SO_3.

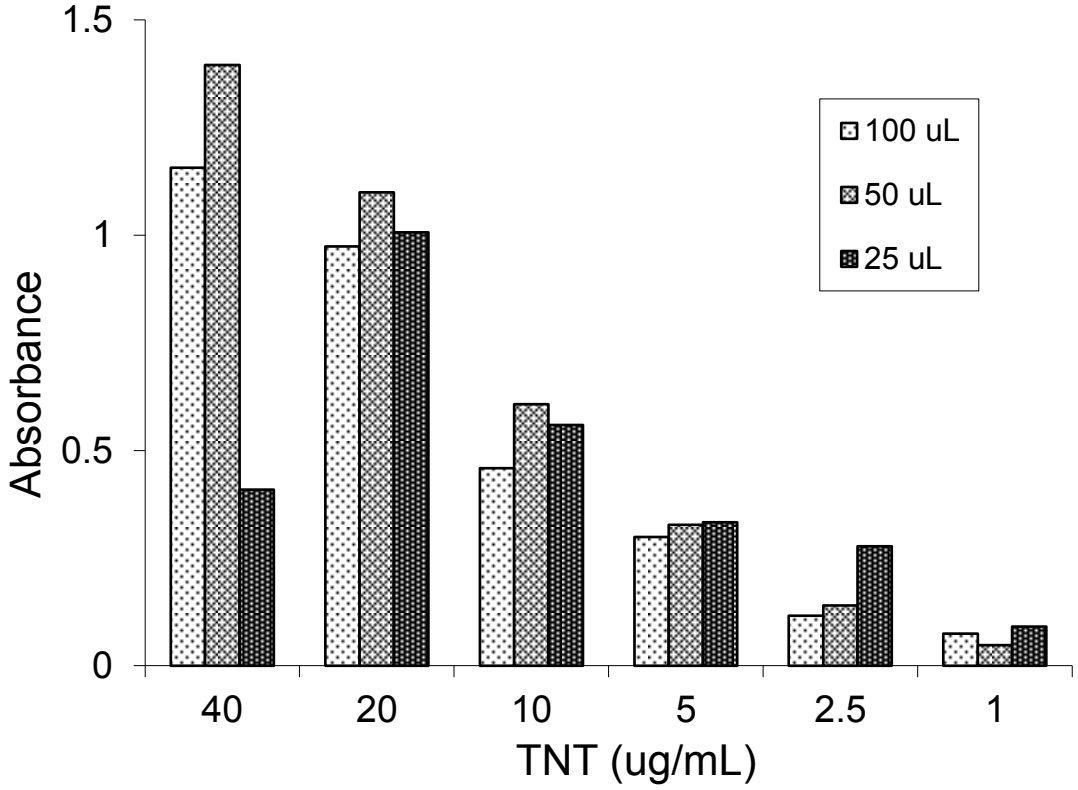

FIGURE 4.6 Determination of the amount of 1 M NaOH required for TNT in acetonitrile. At lower concentration levels of TNT, smaller amounts of NaOH yield stronger absorption, and hence, 25 uL of NaOH is used in all reactions measured at 523 nm.

reaction is run without Na2SO3. The absorption maximum is determined to be 523 nm, which is close to the 514 nm wavelength of the argon ion laser used.

4.4 Laser Wave-Mixing Detection

After the analytes are tested and confirmed by UV-visible absorption measurements, the wave-mixing signal is confirmed by checking its cubic dependence on input laser power [20, 21]. **FIGURE 4.7** shows cubic dependence of TNT wave-mixing signal on laser power for the 19.5 to 46.3 mW power range using a 500 pg/mL TNT complex sample in a capillary cell. The deviation from strict cubic dependence, i.e., a slope of 3, is likely due to some residual scattered noise in the system. The slope of this residual scattered noise is likely to be 1.0, as it is dependent only upon laser power and it is not the nonlinear signal desired. The scattered noise reduces the slope from cubic because noise represents a higher baseline level from which the signal has to emerge. Thus, the net signal seen will be lower at all power levels causing a deviation from the expected cubic dependence on laser power. Adding spatial filters and eliminating more background noise levels can increase the slope closer to the expected value of 3.0. Furthermore, the point with the greatest laser power is beginning to show the effects of power saturation on the sample. As the laser power increases, power saturation is observed.

FIGURE 4.8 shows comparison between the injected sample and a blank sample. A seven-point moving average is used to smooth some noise due to bubbles or small particulates in the capillary cell. A 1 pg/mL injected sample

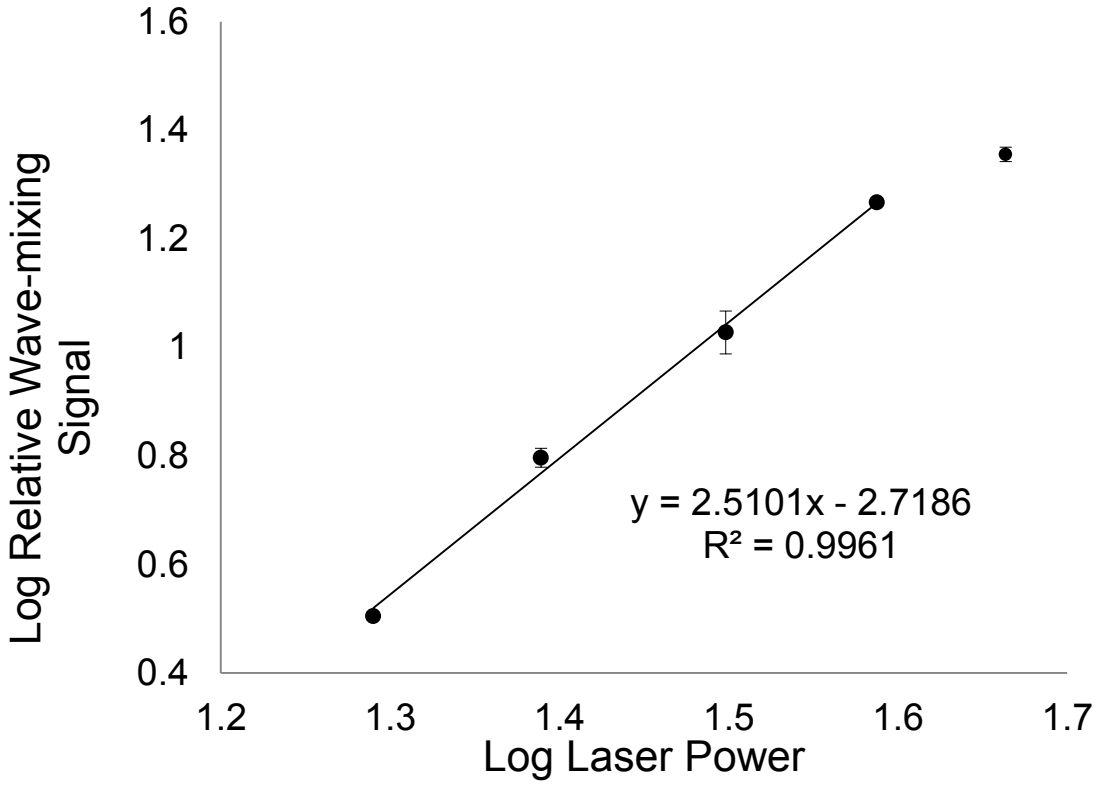

FIGURE 4.7 Cubic dependence of wave-mixing signal of 0.5 ng/mL TNT in acetonitrile (the slope is lower than the expected 3.0 due to some residual background noise levels). The data point with the highest laser power is beginning to show the effects of power saturation.

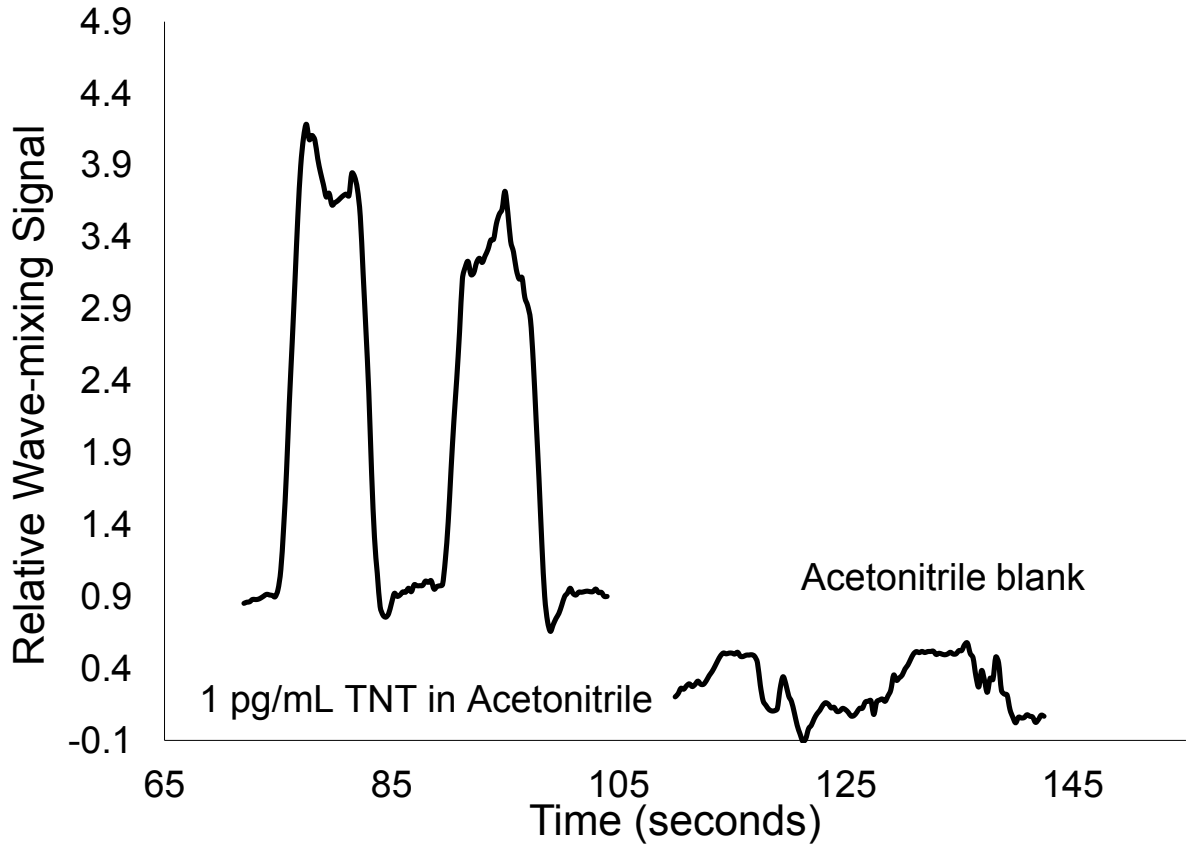

FIGURE 4.8 Wave-mixing signal of 1 pg/mL TNT analyte compared to blank sample containing only acetonitrile.

yields a S/N of 7.5. A preliminary detection limit of 0.516 pg/mL or 0.516 parts-per-trillion is determined at S/N of 2. This corresponds to a concentration detection limit of 2.27×10^{-12} M and a mass detection limit of 2.09×10^{-18} mole or 5.57×10^{-16} g or 1.26×10^{7} molecules inside the laser probe volume. Appendix A shows detailed calculation to determine these LOD levels.

4.6 Conclusions

Laser wave mixing is a sensitive absorption-based method for the detection of a colored TNT complex. This simple one-step reaction is easily adapted to a capillary-based analyte flow cell. The reaction with NaOH induces a color change in the TNT molecule that can then be conveniently probed using a visible argon ion laser at 514 nm. The reaction comes to completion in five minutes and is stable for at least 30 minutes. A preliminary limit of detection of 516 ppt is determined for trinitrotoluene, which compares favorably with other detection methods for TNT.

REFERENCES

1. Karasch, C; Popovic, M; Qasim, M; Bajpai, RK: *Applied Biochemistry and Biotechnology.* **2002**, vol 98-100, pg 1173-1185.

2. EPA Method 8330.

3. Lu, Q; Collins, GE; Smith, M; Wang, J: *Analytica Chimica Acta.* **2002,** 469, 253-260.

4. Jenkins, TF; Walsh, ME: *Talanta.* **1992,** 39(4), 419-428.

5. Khan, H; Harris, RJ; Barna, T; Craig, DH; Bruce, NC; Munro, AW; Moody, PCE; Scrutton, NS: *Journal of Biological Chemistry*. **2002**, 277(24), 21906-21912.

6. Schulte-Ladbeck, R; Kolla, P; Karst, U: *Analyst.* **2002,** 127, 1152-1154.

7. Wallenborg, SR; Bailey, CG: *Analytical Chemistry.* **2000,** 72(8), 1872-1878.

8. Cumming, CJ; Aker, C; Fisher, M; Fox, M; La Grone, MJ; Reust, D; Rockley, MG; Swager, TM; Towers, E; Williams, V: *IEEE Transactions on Geoscience and Remote Sensing.* **2001,** 39(6), 1119-1128.

9. Albert, KJ; Walt, DR: *Analytical Chemistry.* **2000,** 72(9), 1947-1955.

10. Barnes, JC; Golnazarians, W: *Acta Crystallographica.* **1987,** C43, 549-552.

11. Goodpaster, JV; McGuffin, VL: *Analytical Chemistry.* **2001,** 73(9), 2004-2011.

12. Sohn, H; Sailor, MJ; Magde, D; Trogler, WC: *Journal of the American Chemical Society.* **2003,** 125(13), 3821-3830.

13. Shriver-Lake, LC; Charles, PT; Kusterbeck, AW: *Analytical and Bioanalytical Chemistry.* **2003,** 377, 550-555.

14. Altstein, M; Bronshtein, A; Glattstein, B; Zeichner, A; Tamiri, T; Almog, J: *Analytical Chemistry*. **2001,** 73(11), 2461-2467.

15. Holmgren, E; Carlsson, H; Goede, P; Crescenzi, C: *Journal of Chromatography A*. **2005,** 1099, 127-135.

16. Groom, CA; Halasz, A; Paquet, L; Thiboutot, S; Ampleman, G; Hawari, J: *Journal of Chromatography A*. **2005,** 1072, 73-82.

17. Shankaran, DR; Gobi, KV; Sakai, T; Matsumoto, K; Toko, K; Miura, N: *Biosensors and Bioelectronics.* **2005,** 20, 1750-1756.

18. Knittle, J: *Ph.D. Dissertation*, **2004**, UCSD-SDSU.

19. Janowsky, JV: *Berichte**, 1891,** 24, 971**.**

20. Wu, Z; Tong, WG: *Anal. Chem.* **1993**, *65 (2)*, 112-117.

21. Wu, Z; Tong, WG: *Anal. Chem.* **1991**, *63(18)*, 1943-1946

Chapter 5

Detection of Triacetone Triperoxide Using Horseradish Peroxidase and 2, 2'-azino-bis (3-ethylbenzothiazoline-6-sulphonic acid)

5.1 Introduction

Wolffenstein first synthesized triacetone triperoxide (TATP) in 1895 [1]. TATP is easily synthesized with materials that are readily available from a variety of retail outlets. This ease of access makes TATP an attractive explosive for terrorists and criminal organizations around the world. As reported by Associated Press, the Danish government convicted three men for their involvement in a plot to destroy a variety of buildings in Copenhagen based on the seizure of TATP in the home of one of the defendants [2]. A similar incident in Australia in 2005 resulted in the arrest of a man for the possession of instructions and materials for the production of TATP [3]. The ease of synthesis makes it imperative that sensitive and specific detection techniques are available for use by law enforcement and military officials. Laser wave-mixing spectroscopy offers the sensitivity needed to detect TATP in the minute quantities found as residue on surfaces or as trace material left after detonation.

Detecting TATP in its native form with a desirable sensitivity level is challenging since it does not fluoresce [4]. There are a number of different methods that work around the lack of absorption or fluorescence. The simplest method for detecting TATP involves breaking it down into acetone and hydrogen peroxide in the presence of a strong acid [5]. In addition, there is a variety of

colorimetric, electrochemical and surface detection techniques, as listed in Table 1. Laser wave-mixing detection coupled with a colorimetric assay presented here offers sensitivity levels that are equal or better than previously reported techniques for triacetone triperoxide.

5.2 Experimental Setup

The experimental setup used here is similar to that discussed previously in this dissertation. A 405-nm solid-state laser with a sustained output power of 53 mW is split by a 70/30 Reflectance/Transmittance beam splitter to form two input beams, E1 and E2. The reflected beam from the beam splitter, E1, has higher laser intensity and serves as the pump beam. The weaker beam, E2, is modulated by an optical chopper (Stanford Research Systems, SR540, Sunnyvale, CA). The chopper is interfaced to a lock-in amplifier (Stanford Research Systems, SR810, Sunnyvale, CA), which is connected to a computer for data acquisition and display. These two input excitation beams travel equal distances to a 10 cm lens that focuses and mixes the beams within the sample cell. The beam waist is calculated to be 23 μm using the beam waist equation [6] and the resulting laser probe volume is estimated to be 0.5 nL. A 150 μm i.d. flexible fused silica capillary tube (Polymicro Technologies, Phoenix, AZ) is used as a sample holder and detection cell after a small portion of the outer polyimide coating is removed to allow input laser beams to pass through. The analyte samples are pushed through the capillary using a syringe pump (New Era Pump Systems, NE-1000, Farmingdale, NY).

All UV-visible absorption measurements are performed using a UV-visible absorption spectrometer (Hewlett Packard, 8452A) and a Quartz cuvette and FT-IR work is performed using a FT-IR spectrometer (Nicolet 1700). Trace amounts of TATP is obtained off the shelf from a vendor or synthesized using the method reported by Dubnikova [7]. Equimolar portions of acetone and hydrogen peroxide are mixed at 0°C. Concentrated sulfuric acid is then added drop wise (5 drops) to the mixture. After 24 hours, the resulting TATP crystals are collected and analyzed by NMR and FT-IR. The reaction can also produce the dimer diacetone diperoxide (DADP) as DADP and TATP are both formed in the ring closing reaction [8]. TATP is the kinetic product of the reaction [7], and DADP, a thermodynamic product of the reaction, forms more slowly. Hence, a small amount of DADP is present with TATP in the final product. Both TATP and DADP are both explosive chemicals; however, DADP is harder to isolate and less stable than TATP, and it is not used as widely in real-world applications.

5.3 FT-IR and NMR Studies

FIGURE 5.1 shows the FT-IR spectrum of 10 mg/mL TATP in acetonitrile from 1050 to 1350 cm^{-1} with a broad peak from 1150 to 1220 cm^{-1} and two smaller peaks at 1235 cm^{-1} and 1275 cm^{-1}. The FTIR collects 50 scans of neat acetonitrile as background. The background is subtracted from the 50 scans of TATP in acetonitrile solution. Our FT-IR spectrum matches well with that previously reported [4]. **FIGURE 5.2** shows the proton NMR confirmation for our synthesized TATP and the result agrees with previously published data [9, 10],

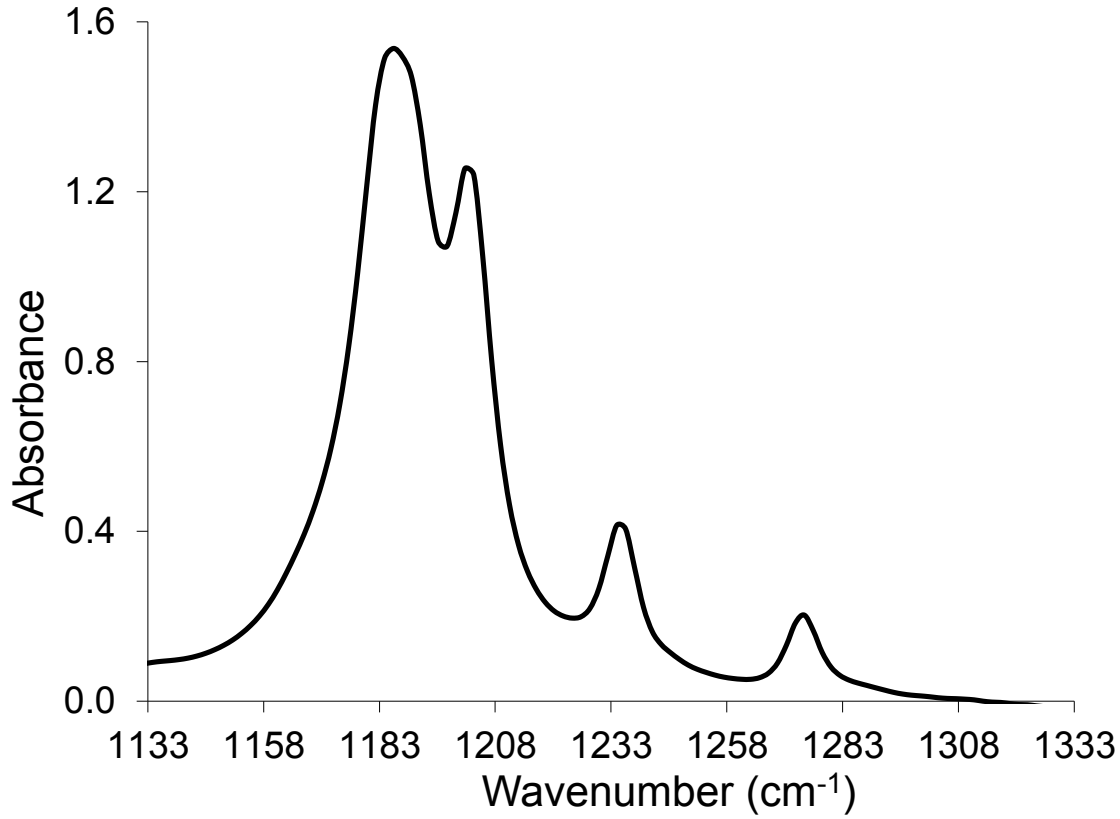

FIGURE 5.1 FT-IR spectrum of 10 mg/mL TATP in acetonitrile with a large peak centered at 1195 cm^{-1} and 2 smaller peaks at 1235 and 1275 cm^{-1}. The instrument was blanked using neat acetonitrile.

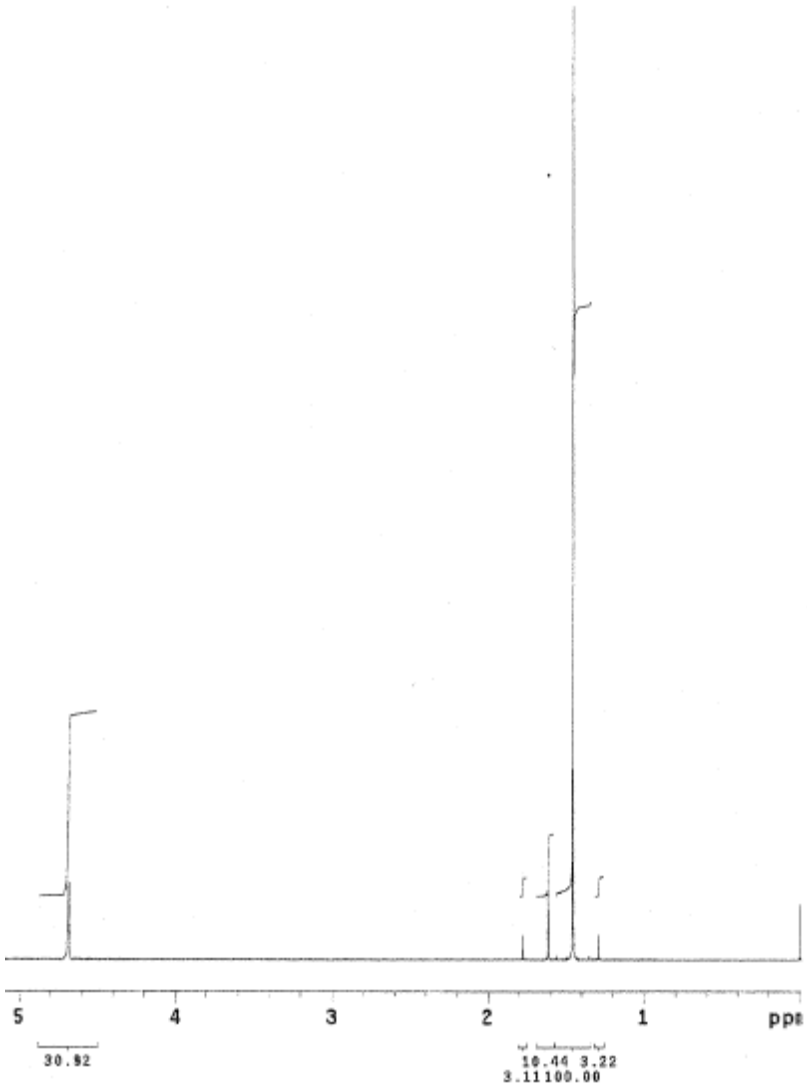

FIGURE 5.2 Proton NMR spectrum of synthesized TATP. The largest peak at 1.46 ppm is the methyl peak shifted down field due to the two oxygen atoms bound to the alpha carbon. The two smaller peaks that appear to be a doublet at 1.29 and 1.77 ppm are actually two singlet peaks that represent equatorial and axial methyl groups due to the impurity DADP. The two singlet peaks at 1.6 and 4.8 ppm are due to water.

with a large singlet at δ = 1.46 ppm and two very small singlets at δ = 1.29 and 1.77 ppm. The smaller peaks are likely from a small amount of diacetone diperoxide, a by-product of TATP synthesis. The DADP peaks, δ = 1.29 and 1.77 ppm, are the axial and equatorial methyl groups in the cyclohexane like DADP molecule. These peaks match those reported by Pena *et al.* [10]. The peaks at 1.6 and 4.7 ppm can be attributed to residual water in the sample, as hydrogen peroxide used in the reaction is a 50% solution in water. Bulk water that can form a film on NMR tube walls is known to give a peak at 4.7 ppm in $CDCl_3$ [11]. The monomeric form of water that is dissolved into the $CDCl_3$ yields a peak at 1.6 ppm. The NMR water peaks observed likely result from TATP crystals that are not fully dried. **FIGURE 5.3** shows carbon NMR confirmation with two peaks indicative of TATP at δ = 21.33 ppm and δ = 107.55 ppm for the methyl and peroxy carbons, respectively. The small doublet at δ = 23.14 and 20.40 ppm are indicative of the by-product DADP. These results agree with those previously reported [10].

5.4 UV-Visible Absorption Studies

The breakdown of TATP by using strong acid results in the production of acetone and hydrogen peroxide as previously reported [12]. Hydrogen peroxide is detected with an enzyme-catalyzed method for peroxide determination. In this work, 2, 2-azino-bis (3-ethylbenzothiazoline)-6-sulfonate (ABTS) is used as the substrate for horseradish peroxidase (HrPO). ABTS is colorless and it reacts readily with hydrogen peroxide in the presence of HrPO to yield a green-colored

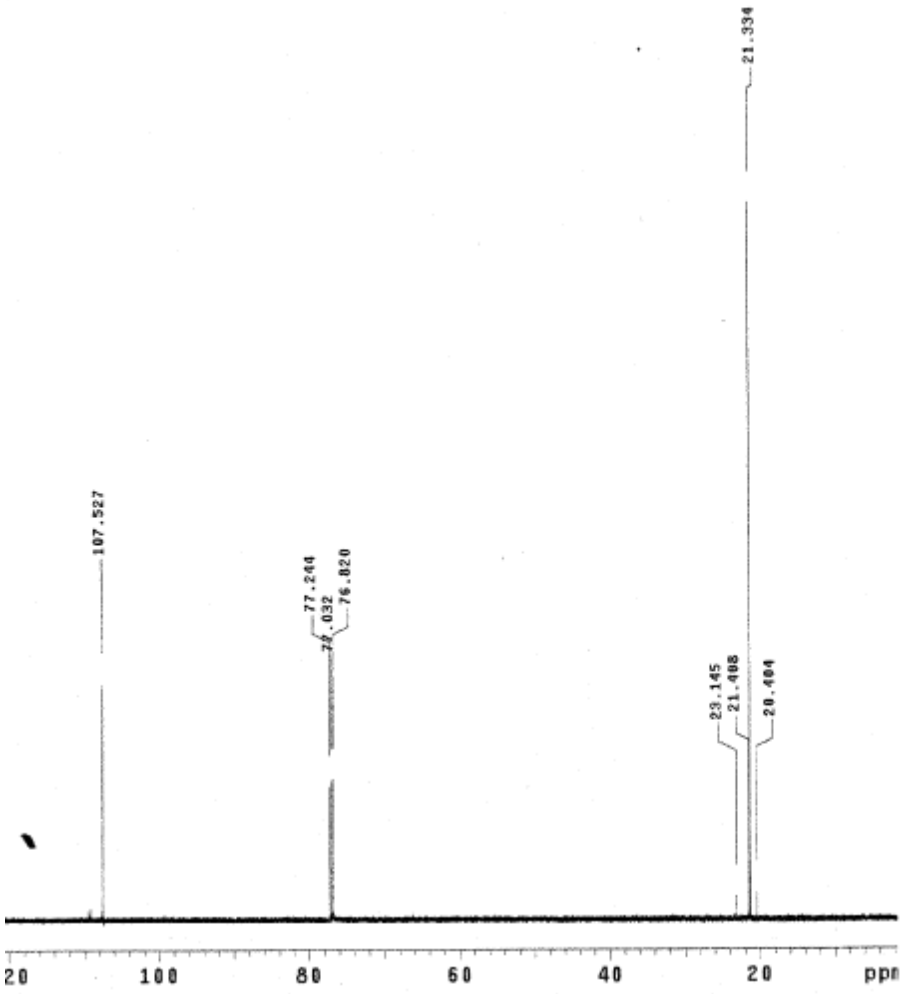

FIGURE 5.3 Carbon NMR spectrum of synthesized TATP with peaks at 21.33 and 107.55 ppm from TATP carbons, peaks at 20.40 and 23.14 ppm from DADP carbons, and triplet peaks at 77 ppm from $CDCl_3$.

radical cation with major absorption peaks at 415, 650, 730 and 810 nm. The horseradish/ABTS reaction system is optimized and confirmed using UV-visible absorption measurements for a number of parameters before laser wave-mixing analysis.

FIGURE 5.4 shows UV-visible absorption spectrum with four broad peaks at 425, 646, 733 and 823 nm, and the peak at 425 nm has the largest absorbance. There are four laser options available in the lab for this work. A 405 nm diode laser with 53 mW output power, a 633 nm HeNe with 12 mW output, a tunable external cavity diode laser with a 768 – 794 nm tuning range and 15 mW output, and a tunable external cavity diode laser with a 830 – 855 nm tuning range and 40 mW output. For this work, a 405 nm solid-state laser is chosen since it provides the highest output power and it can probe the strongest absorption peak.

The reaction time needed to maximize the absorption level is determined by taking UV-visible absorption spectra at set time intervals while monitoring the absorbance at 405 nm, as shown in **FIGURE 5.5**. The reaction begins to plateau at 10 minutes and shows minimal change thereafter. These results indicate that the reaction should be allowed to proceed for at least 10 minutes before analyzing in the DFWM detection setup.

It is also important to determine the incubation time needed to degrade TATP with 18 M sulfuric acid in order to produce the peroxides that react with HrPO/ABTS. **FIGURE 5.6** shows the absorbance values at 405 nm while incubating TATP with 18 M sulfuric acid. The results indicate that TATP is

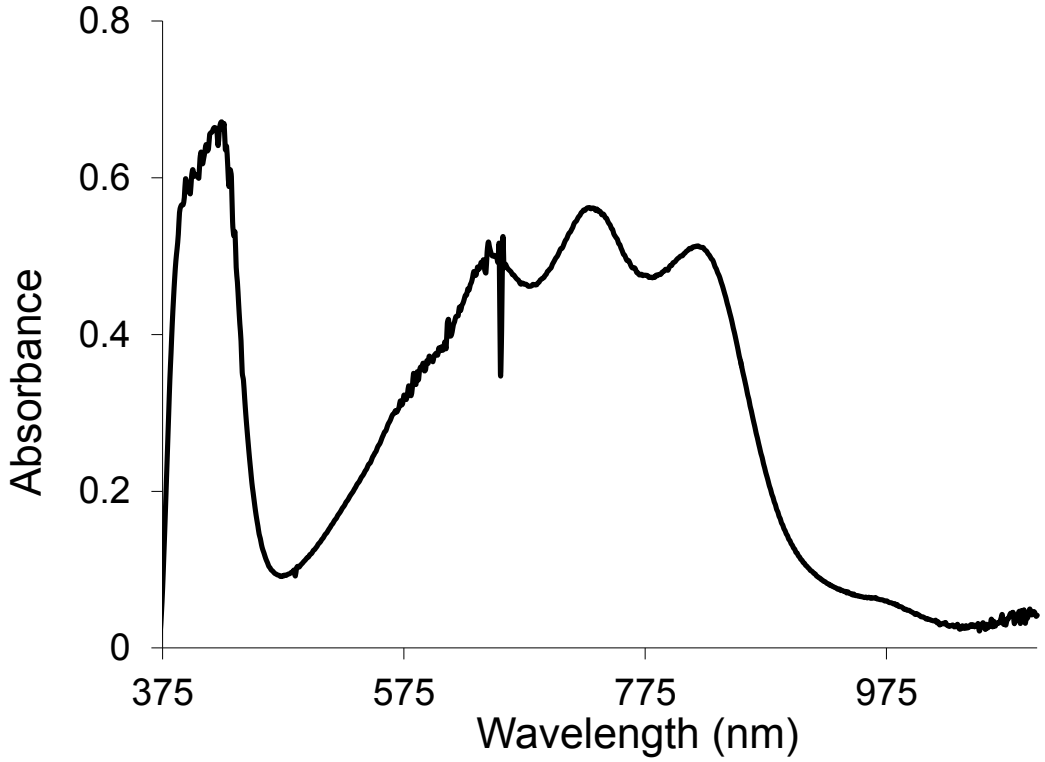

FIGURE 5.4 UV-visible absorption spectrum of horseradish peroxidase-ABTS reaction mixture with TATP showing four large absorption peaks at 425, 646, 733 and 823 nm. A 405 nm solid-state laser is used to excite the sample.

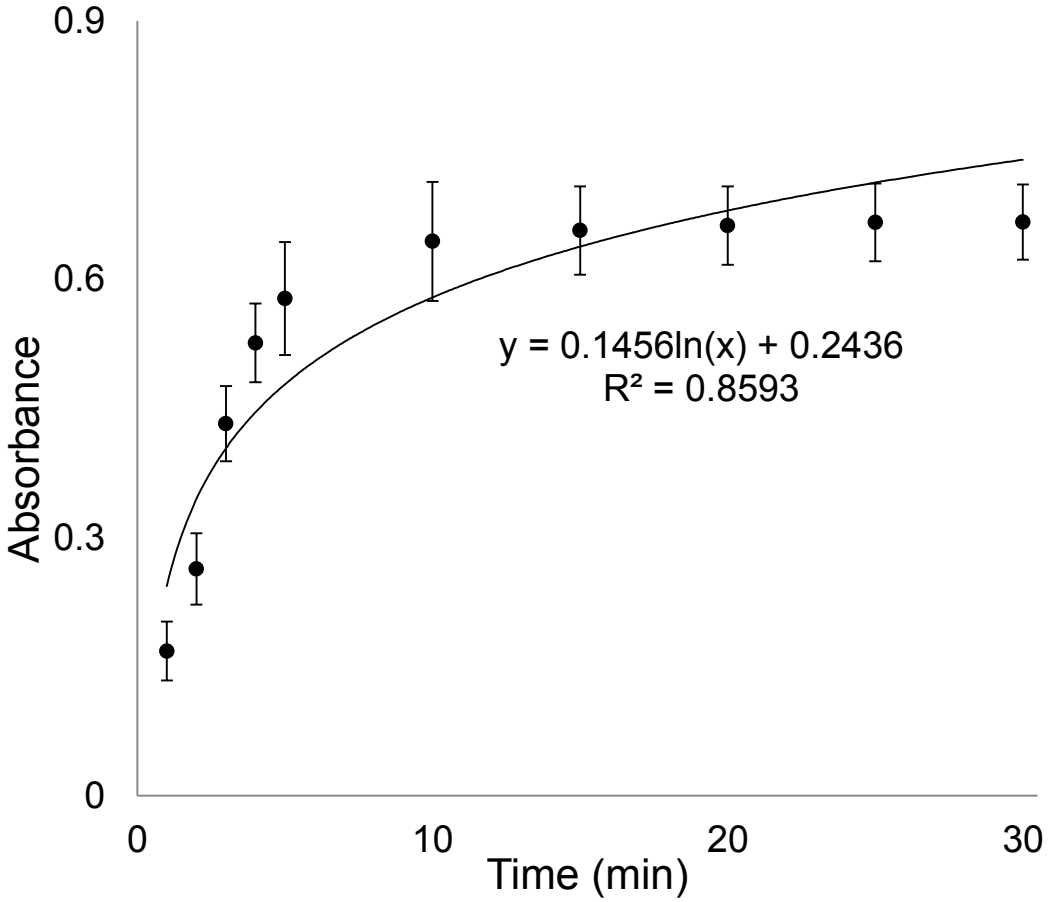

FIGURE 5.5 Reaction-time study showing absorption plateau beginning at 10 minutes, the reaction time needed for horseradish peroxidase, ABTS and TATP.

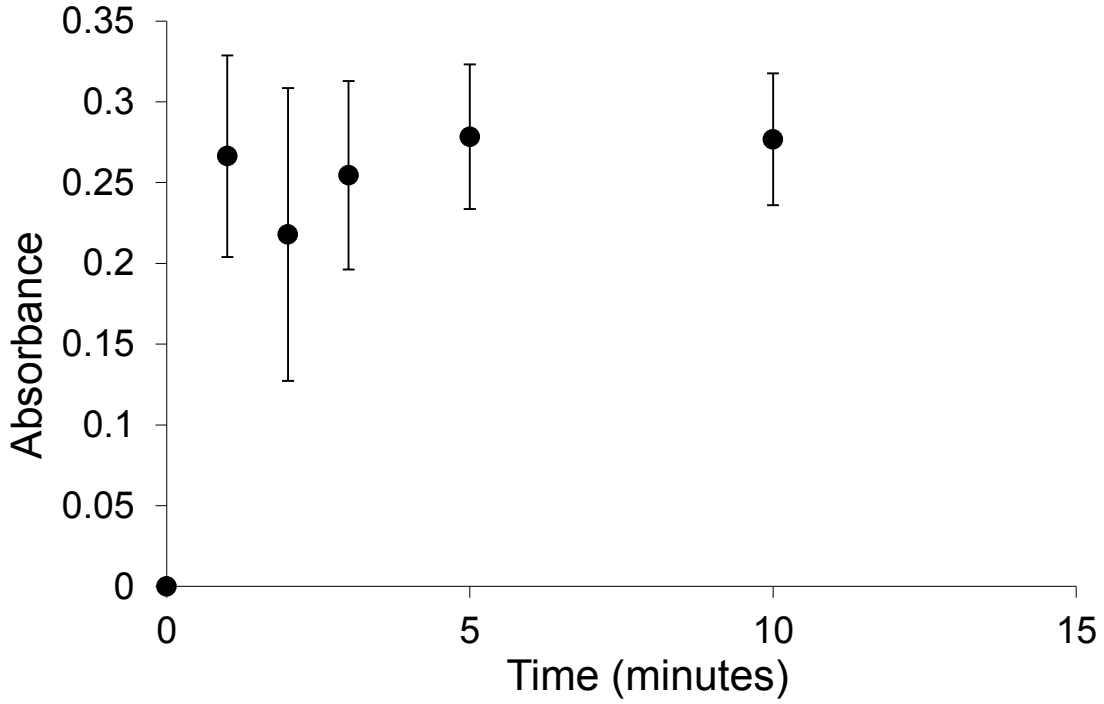

FIGURE 5.6 Incubation-time study indicating the effect on absorption at 405 nm using 18 M sulfuric acid. A pre-incubation time of one minute is adequate to breakdown TATP.

broken down quickly and that a long incubation time is not needed. However, the acid volume required to push the degradation of TATP into peroxide is critical to the reaction. **FIGURE 5.7** shows an examination of the volume of 18 M sulfuric acid needed to breakdown TATP while monitoring the absorption peak at 405 nm. The results indicate that 50 µL of the acid should be used to maximize TATP degradation in order to create colored ABTS radical cations.

These studies provide the reaction mixture parameters used in this work. First, 100 µL of TATP is incubated with 50 µL of 18 M sulfuric acid for 2 minutes. Then, 400 µL of 0.67 mg/mL ABTS in 0.01 M sodium acetate buffer and 400 µL of 0.052 M horseradish peroxidase in 0.01 M sodium acetate buffer are added and allowed to react for 10 minutes. The colored product is then analyzed and confirmed.

5.5 Laser Wave-Mixing Detection

Once the parameters of the reaction are determined and confirmed using UV-visible absorption measurements, the DFWM detection parameters are optimized. First, the optimum amplitude modulation frequency is determined by changing the optical chopper frequency while monitoring the DFWM signal, as shown in **FIGURE 5.8**. As usual, the 60 Hz AC frequency and its harmonic frequencies are avoided in this test, and the results show that 500 Hz yields the strongest signal and S/N, and it agrees with previously published reports [13, 14]. The modulation frequency should be slow enough to allow adequate grating

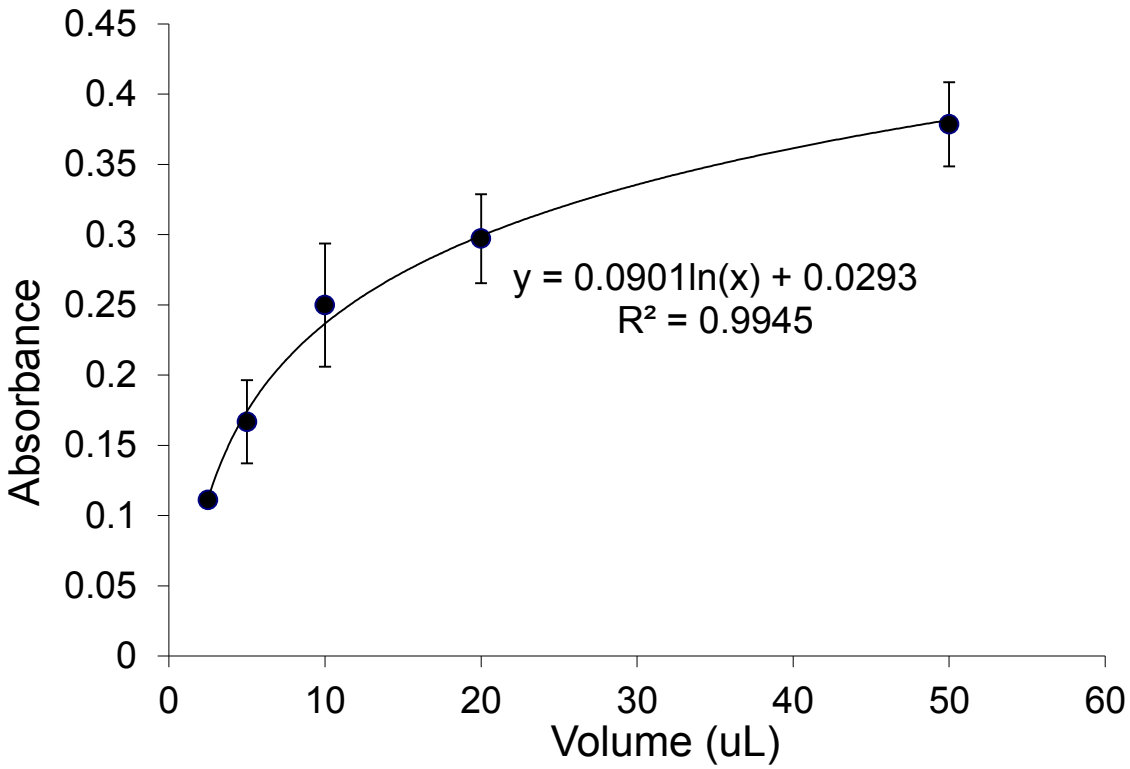

FIGURE 5.7 Acid-volume studies while monitoring absorption at 405 nm. The more acid is used, the more TATP is broken down into peroxide, and hence, the higher the absorption.

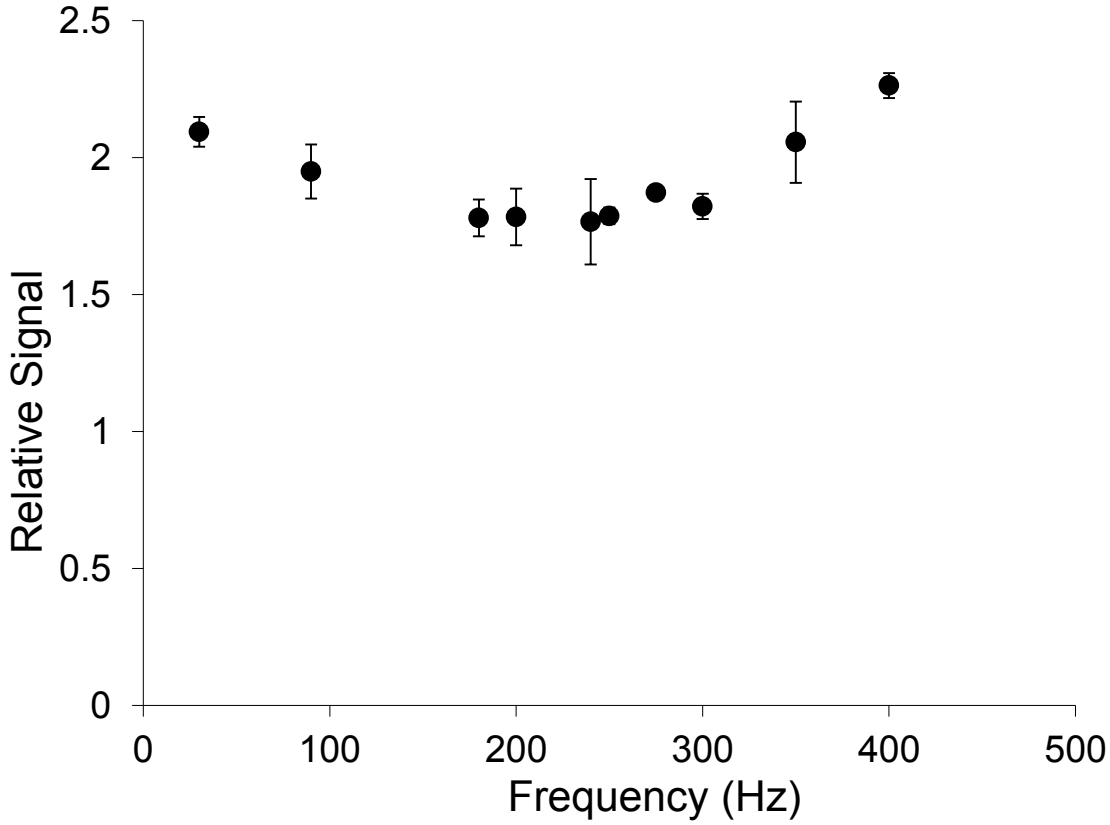

FIGURE 5.8 The optical chopper modulation test shows that the signal is strong at 500 Hz.

formation, especially in condensed-phase analytes, and fast enough to avoid some low frequency background environmental noise sources.

The analyte flow rate also has some effect on the DFWM signal strength since fast flow rates may not allow the thermal gratings to fully form inside the detection probe volume. As shown in **FIGURE 5.9,** the optimum analyte flow rate is determined to be 0.05 mL/hr for the capillary cell used and it is well within the range of flow rates commonly used in capillary electrophoresis separation systems.

FIGURE 5.10 shows confirmation of DFWM signal for the 100 ug/mL TATP sample with the expected cubic dependence on laser power within the 10 to 37.3 mW range tested. The experimental slope is 2.94, very close to the expected slope of 3.0, confirming the detection of DFWM signal and not other conventional optical signals such as fluorescence.

FIGURE 5.11 shows our detection sensitivity study with a TATP sample peak compared to that of a blank solution (same solvent without TATP). A 10 pg/mL analyte solution is injected into the capillary cell to generate the DFWM signal. A preliminary concentration detection limit of 3.7 pg/mL or 3.7 ppt is determined (at S/N of 2) based on the peak recorded with a S/N of 14.6. Our concentration detection limit compares favorably to those of other detection methods, as shown in **TABLE 5.1.**

The mass detection limit of this assay is determined based on our calculated laser probe volume formed by the two input beams. First, the diameter of the input beam spots (2.20 mm) and the center-to-center distance

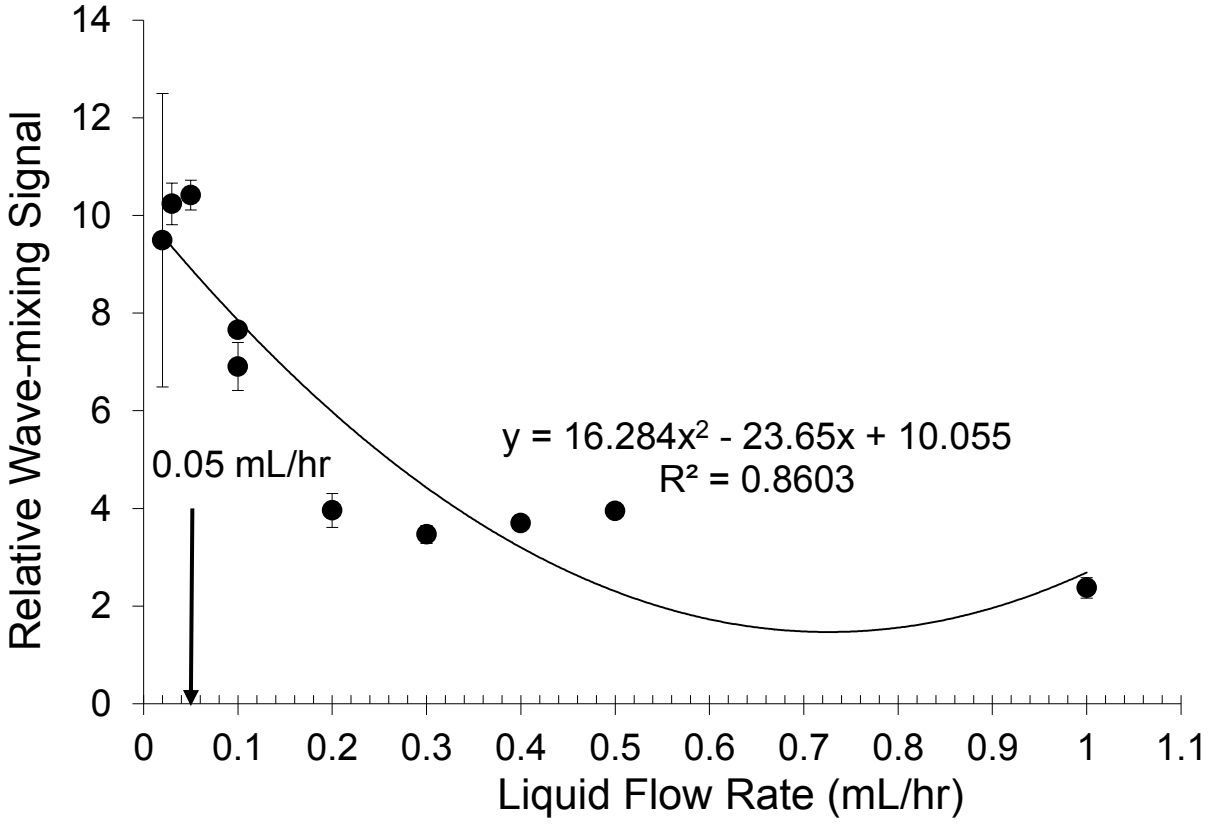

FIGURE 5.9 Analyte flow-rate study indicates that the signal remains strong over a range of flow rates widely used for capillary electrophoresis. A flow rate of 0.05 mL/hr is used for the work here.

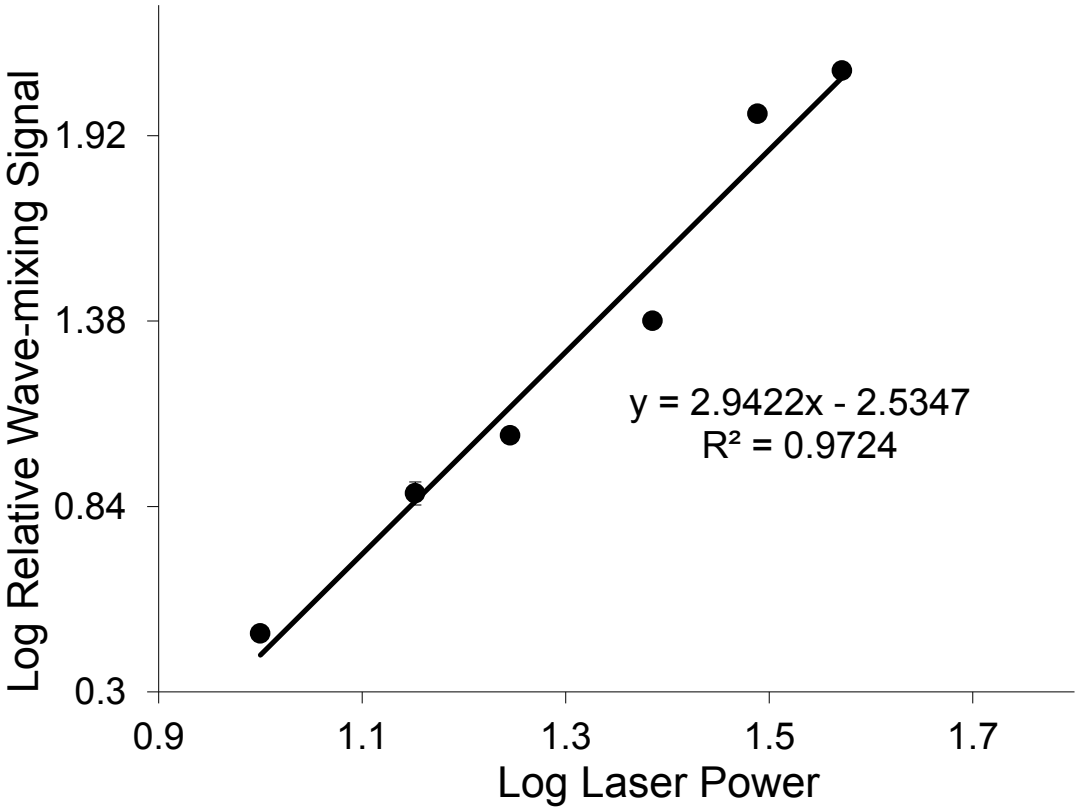

FIGURE 5.10 Cubic dependence of DFWM signal on laser power is confirmed for the 10 to 37.3 mW power range tested. A slope of 2.94 is measured, close to the expected slope of 3.0.

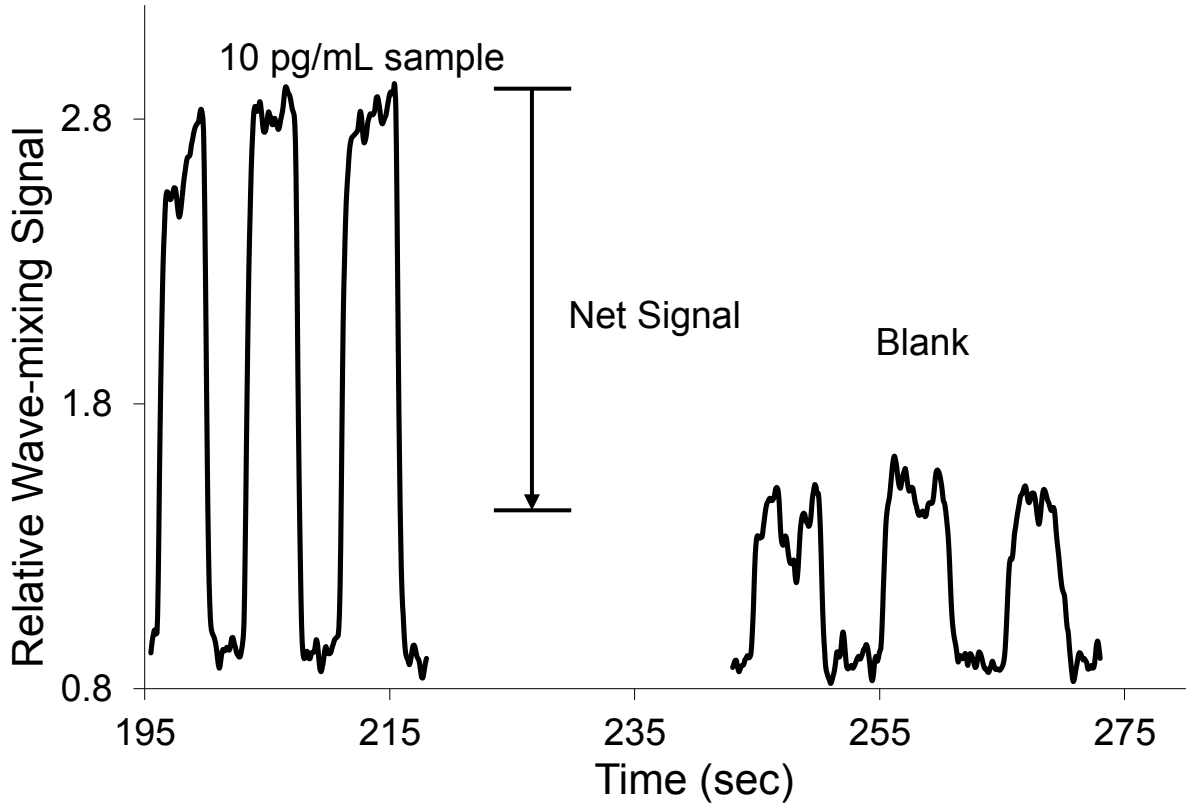

FIGURE 5.11 Laser wave-mixing detection of TATP complexed with horseradish peroxidase and ABTS. The blank sample consists of acetonitrile, sulfuric acid, horseradish peroxidase and ABTS.

between the two input beams (2.88 mm) are measured. Based on the beam angle calculated (1.65°) for the two input beams, a laser probe volume of 0.468 nL is determined. Based on this probe volume, a mass detection limit of 1.77 x 10^{-15} g or 7.80 x 10^{-18} mole or 4.69 x 10^{6} molecules inside the probe volume is determined.

5.6 Conclusions

Laser wave mixing has been demonstrated to be a sensitive detection technique for TATP in the liquid phase. Breaking down TATP into peroxides that form a colored complex with ABTS in the presence of horseradish peroxidase allows the detection of TATP using a convenient visible laser wavelength. Our low ppt concentration detection limit and low femtomole mass detection limit for TATP in the condensed phase compare favorably to those from other detection methods.

Table 5.1: Comparison of detection methods for TATP.

TATP Detection Technique	**Wavelength (λ)**	**Limit of Detection (LOD)**	**References**
UV-visible absorption	415 nm	8 x10^{-6} M	Analyst, **2002**, Vol. 127, 1152 – 1154
Fluorescence spectroscopy	Ex at 324 nm Em at 405 nm	2 x 10^{-6} M	Analytical Chemistry, **2003**, 75, 4, 731-735
Metal-ion complexation	N/A	N/A	J. Phys. Chem. A **2002**, 106, 4951-4956
Self-immolative dendritic probe	Ex at 279 nm Em at 560 nm	N/A	Chem. Commun., **2008**, 5701–5703
Reaction with borate prochelator	Ex at 270, 350 nm Em at 380, 400 nm	10 nM	Inorganic Chemistry, 47, 21, **2008,** 9748-9750
Double step chronoamperometry		8.51 uM	Microchemical Journal, **2010**, 94, 166-170
Chemiluminescence		18 nM	Anal Bioanal Chem **2011,** 400, 313–320
Colorimetric sensor array using Amberlyst-15		10 nM	J Am Chem Soc, **2010**, 132, 15519-15521
Laser wave mixing (liquid phase)		16.6 pM,	This work

REFERENCES

1. Wolffenstein, R. *Chem. Ber.* **1895**, *28*, 2265 – 2269.

2. Olsen, JM: *The San Diego Union Tribune*, **2007**, Nov 23.

3. Bonner, R: *The New York Times*, **2005**, Nov 15.

4. Schulte-Ladbeck, R; Edelmann, A; Quintas, G; Lendl, B; Karst, U*: Anal. Chem.* **2006**, *78,* 8150 – 8155.

5. Lin, H; Suslick, K: *JACS Comm.* 2010, 132, 15519-15521.

6. Saleh, B. E. A., Teich, M. C., Fundamentals of Photonics, 1991, John Wiley & Sons, Inc., New York.

7. F. Dubnikova, R. Kosloff, J. Almog, Y. Zeiri, R. Boese, H. Itzhaky, A. Alt, and E. Keinan; *J. Am. Chem. Soc.*, **2005**, 127 (4), 1146-1159.

8. Pacheco-Londono, L; Pena, AJ; Primera, OM; Hernandez-Rivera, SP; Mina, N; Garcia, R; Chamberlain, RT; Lareau, R: *Proceedings of SPIE*, **2004**, *5403*, 279 – 287.

9. Buttigieg, GA; Knight, AK; Denson, S; Pommier, C; Denton, MB; *For. Sci. Int'l.* **2003**, *135*, 53 – 59.

10. Pena, AJ; Pacheco-Londono, L; Figueroa, J; Rivera-Montalvo, LA; Roman-Velazquez, FR; Hernandez-Rivera, SP: *Proceedings of SPIE*, **2005**, *5778*, 347-358,

11. *Spectrometric Identification of Organic Compounds, 6th Edition.* R.M. Silverstein and F.X. Webster, John Wiley and Sons, Inc.

12. Schulte-Ladbeck, R; Kolla, P; Karst, U: *The Analyst*, **2002**, 127, 1152-1154.

13. Wu, Z; Tong, W: *Anal. Chem.* 1993, *65,* 112-117.

14. Wu, Z; Tong, W: *Anal. Chem.* 1991, *63,* 1943 – 1947.

Chapter 6

Mid-Infrared Absorption Spectroscopy Using Quantum Cascade Lasers

6.1 Introduction

Quantum cascade lasers (QCL) are compact solid-state tunable mid-IR lasers that offer many advantages over lead chalcogenide lasers and other bulky mid-IR lasers that require liquid nitrogen-based cooling systems and large power supplies. Quantum cascade lasers are compact, rugged, power efficient, tunable and they do not need cryogenic cooling. In addition, QCLs offer narrow line widths, excellent mode stability, and wavelength reproducibility levels that allow for high-resolution isotopic analysis of small molecules such as SO_3, N_2O, CO_2 and other atmospheric gases [1]. When coupled with a thermoelectrically (TE) cooled sensitive mid-IR detector, a QCL can be used effectively for ultrasensitive detection of chemical agents in the mid-IR wavelength range. In this work, we demonstrate that QCL-based absorption spectroscopy compares favorably to other sensitive absorption-based detection methods including those using multi-pass cells [2], cavity-ring down cavities [3], wavelength modulation schemes [4] and laser wave-mixing setups [5]. We confirm that the absorption spectra collected using a variety of quantum cascade lasers match FT-IR spectra. After the QCL-based detection system is successfully demonstrated in the conventional optical absorption mode, we will interface the QCL system to our laser wave-mixing setup, as described in the next chapter.

6.2 Experimental Setup

Since the QCL emits mid-IR wavelengths, we assemble our laser absorption detection setup using optical components that are suitable for mid-IR wavelengths (Thorlabs, Newton, NJ). When a pulsed QCL is used as the excitation laser, the QCL controller is used to trigger the lock-in amplifier (Stanford Research Systems, SR810, Sunnyvale, CA). When a continuous-wave QCL is used (or a QCL with high kHz rep rate), an optical chopper (Stanford Research Systems, SR540, Sunnyvale, CA) is used to modulate the excitation beam and to trigger the lock-in amplifier. The lock-in amplifier output, i.e., the transmission signal, is digitized using our custom-built AIDA data acquisition program. The QCL transmission spectra are then converted to QCL absorption spectra using the Beer's law equation.

All the initial mid-IR quantum cascade lasers (Daylight Solutions, San Diego, CA) tested in this work use the same controller (Daylight Solutions, 1001-TLC, San Diego, CA). A thermoelectrically cooled HgCdZnTe photovoltaic detector especially designed for mid-infrared wavelengths (Daylight Solutions, Amplified MCT-10001, San Diego, CA) is used to collect the QCL generated absorption signal. All the mirrors used in this work have mid-infrared capable gold coatings and calcium fluoride lenses are designed for mid-IR wavelengths.

Our liquid-phase analytes are held in an IR cell (Crystal Labs, Garfield, NJ) and the absorption path length of the cell is varied by using Teflon rings with different widths. **FIGURE 6.1** shows our custom-designed mid-IR analyte cell

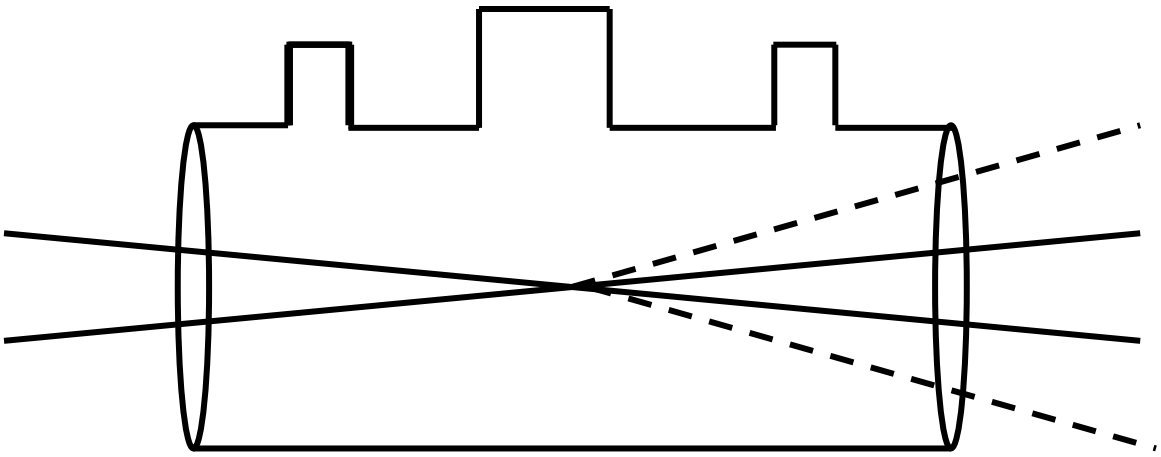

FIGURE 6.1 Mid-IR analyte cell. Each port has a Cajon fitting to allow for airtight sealing during the optical signal measurements.

with calcium fluoride windows (Curtis Technology, San Diego, CA). The cell measures 10 cm x 2.54 cm and has windows attached at a slight angle (1 degree) to minimize reflected background optical noise levels. The cell has three inlet/outlet ports that allow introduction and evacuation of gas, liquid and solid samples. All FT-IR spectra, unless otherwise indicated, are collected using a conventional FT-IR spectrometer (Nicolet Nexus 760) in the 50-pass absorption mode. Mid-IR spectra are also compared to those from the National Institute of Standards and Technology (NIST) for further confirmation.

6.3 Quantum Cascade Laser-Based Absorption Measurements

Different molecules are probed using our custom-designed quantum cascade laser-based optical absorption detection system. In some cases, the limits of detection are determined as described below for different analytes.

6.3.1 Liquid 2, 4-Dinitrotoluene Analyte (1050 – 1095 cm^{-1} Pulsed QCL)

2, 4-dinitrotoluene is found as an impurity in the production of 2, 4, 6-trinitrotoluene [6], a plasticizing agent used in the production of polyurethanes [7], and as a degradation product of TNT [8]. **FIGURE 6.2** shows the experimentally determined absorption spectra of 2, 4-dinitrotoluene collected by our QCL-based absorption detector and a conventional FT-IR in the 1050 to 1095 cm^{-1} tuning range of the QCL. Each data point is an average of 15 individual data points. The error bars represent the standard deviation of the 15 data points. As the

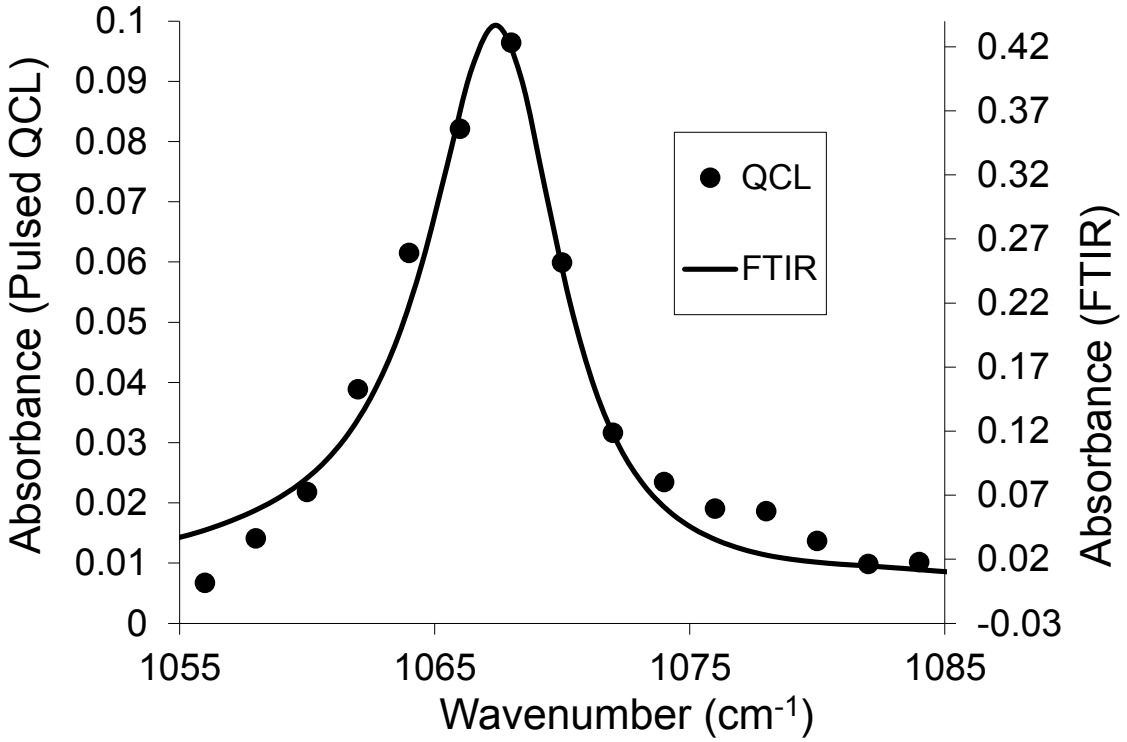

FIGURE 6.2 Absorption spectrum of DNT collected by a quantum cascade laser matches well with the FT-IR spectrum.

data are collected in transmission mode and converted to absorbance using the formula:

$$\text{Absorbance} = -\log (I/I_o)$$

where I is the intensity of the transmission through a sample and I_o is the intensity of transmission through a blank sample. The error propagation follows the form of:

$$\sigma_x = 0.434(\sigma_a/a)$$

where σ_a is the standard deviation of the transmission data and a is the average of the measured transmission [9]. All subsequent absorption spectra generated in this chapter utilize the same process to transform transmission data into absorption data.

Our QCL absorption spectrum agrees well with the FT-IR spectrum. The peak centered at 1068 cm^{-1} represents the out-of-plane bending mode of the aromatic ring [10]. This particular QCL was available and operational for a limited time and further studies were performed using another QCL.

6.3.2 Acetone (1153 - 1223 cm^{-1} Pulsed QCL)

Acetone is a common organic solvent used in the production of triacetone triperoxide (TATP) explosive. Acetone is readily available from a variety of retail outlets. Acetone has a vapor pressure of 24.5 kPa [11] at 20° C, which is much higher than the reported TATP vapor pressure of 0.0004 kPa [12]. Therefore, acetone is a good convenient test sample for our initial gas-phase detection system based on quantum cascade lasers. The broad peak centered at 1217

cm^{-1} represents the C-C stretch between the carbonyl carbon and methyl carbons [13].

6.3.2.1 Acetone Vapor (1153 - 1223 cm^{-1} Pulsed QCL)

FIGURE 6.3 shows the QCL-based absorption spectrum of acetone vapor that is generated from 1 uL of acetone deposited in a sealed 10-cm gas cell. The spectrum is collected by tuning the QCL over the available mid-IR tuning range using a 4 cm^{-1} scanning interval. Our QCL absorption spectrum compares favorably to the FT-IR spectrum.

A flowing sample of acetone vapor, rather than that sealed in an enclosed cell; more closely approximates a chem/bio agent that may be encountered in real-world situations. Hence, a flowing sample cell is designed using a simple plastic bottle with a screw cap that allows a stream of air through an inlet over the surface of a reservoir of acetone, as shown in **FIGURE 6.4**. The acetone vapor escaping from the outlet hole is probed by the QCL. On a thermal observation card, the warm beam spot is clearly visible to the naked eye. When a stream of acetone flows onto the thermal card, the stream and the beam profiles are visible. Thus, aligning the stream to pass through the laser path was a simple process. **FIGURE 6.5** shows the QCL absorption spectrum collected from this acetone vapor jet. Five separate transmission scans were collected and the average and the standard deviation for the transmission data were calculated. The spectrum experimentally generated matches a reference FT-IR spectrum of acetone.

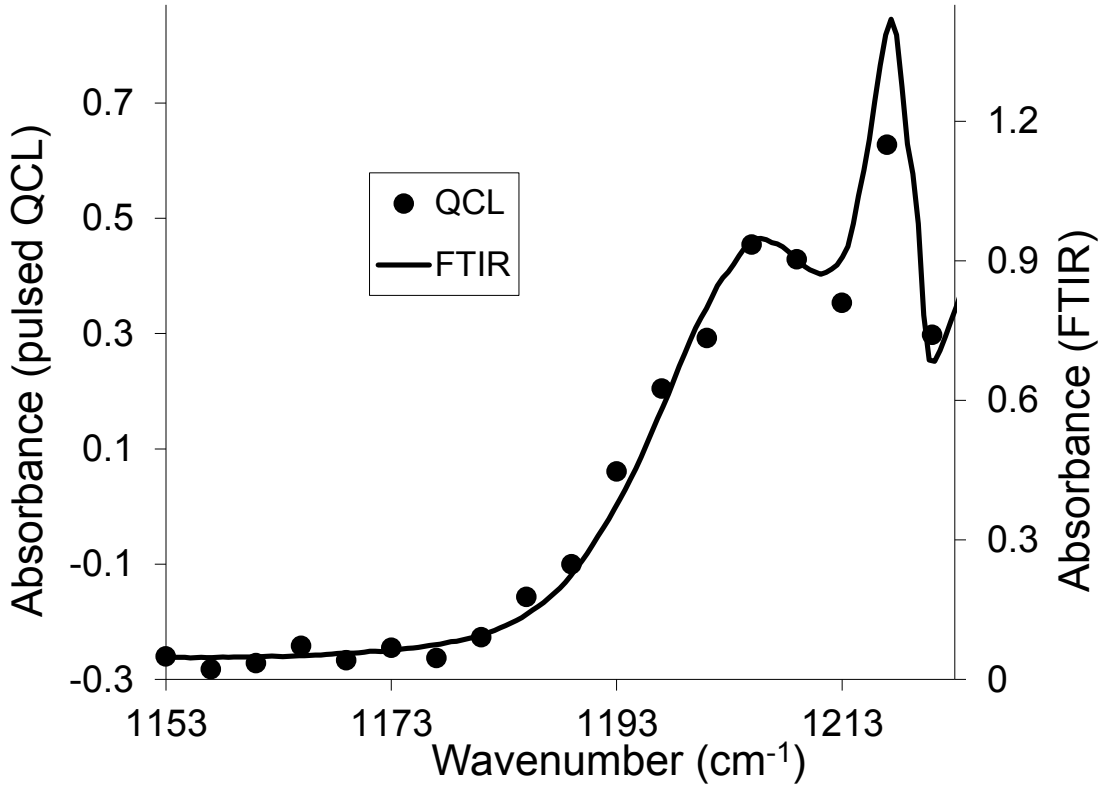

FIGURE 6.3 Gas-phase absorption spectrum of 1 µL of acetone deposited in a 10-cm sealed gas cell. The peak at 1217 cm^{-1} is observed consistently. The QCL spectrum matches the NIST spectrum.

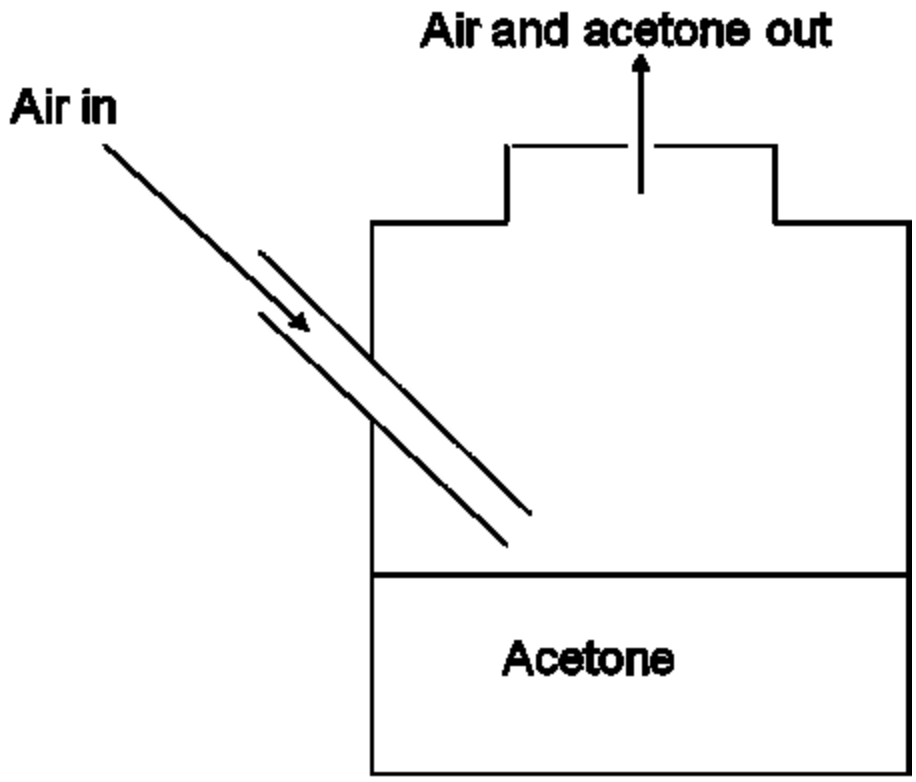

FIGURE 6.4 Custom-built flow cell for detection of flowing acetone vapor. The inlet airflow agitates the acetone analyte and creates a jet of acetone vapor at the outlet where the analyte is probed by the laser.

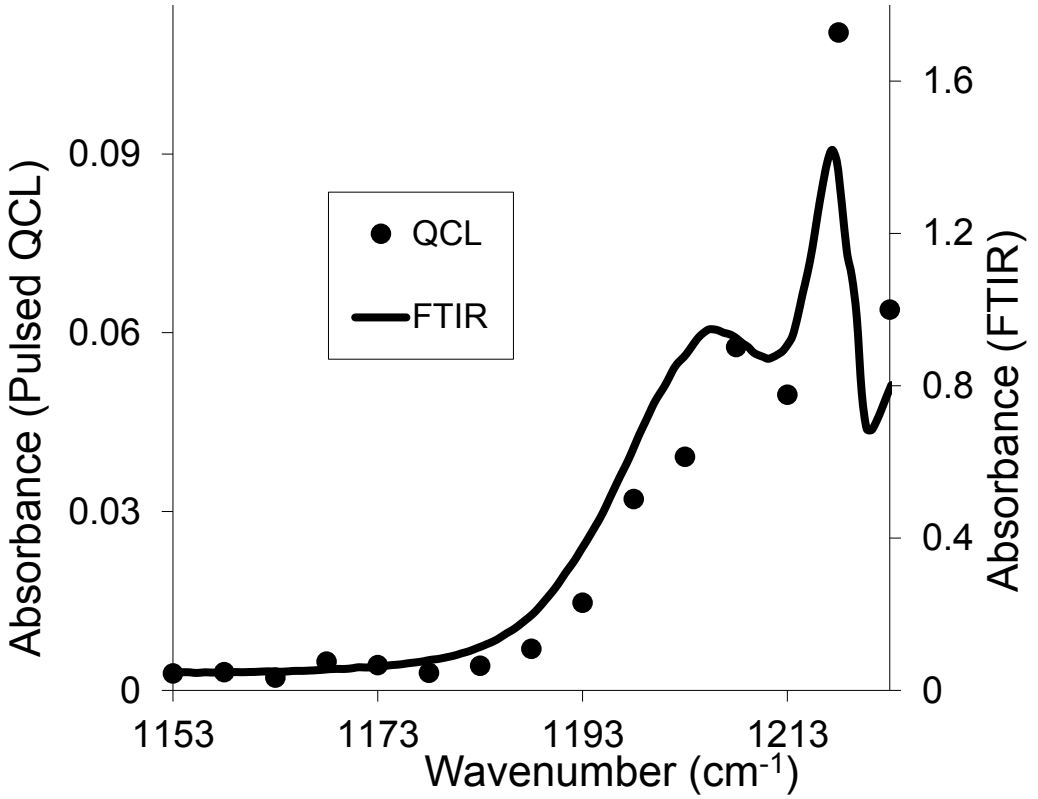

FIGURE 6.5 Absorption spectrum of acetone jet collected by a quantum cascade laser. It agrees with the FT-IR spectrum.

6.3.2.2 Acetone Vapor (1155 - 1255 cm^{-1} Continuous-Wave QCL)

FIGURE 6.6 shows the gas-phase QCL-based absorption spectrum of acetone collected at room temperature using 1 µL of acetone injected into the 10-cm gas cell and allowed to fully evaporate. Our QCL absorption spectrum of acetone vapor in a sealed cell (two-point moving averaged) matches the FT-IR spectrum. This particular continuous-wave QCL has a slightly different tuning range (1155 to 1255 cm^{-1}) as compared to that described in the previous section, and thus, the difference in spectral profile.

6.3.2.3 Acetone Liquid (1155 – 1255 cm^{-1} Continuous-Wave QCL)

FIGURE 6.7 shows the absorption spectrum of acetone in methylene chloride collected using a continuous-wave QCL with a tuning range from 1155 to 1255 cm^{-1}. The QCL absorption spectrum (3-point moving averaged) agrees well with the reference FT-IR spectrum of acetone

6.3.3 Triacetone Triperoxide (TATP) Analyte

As mentioned above, TATP is one of the explosives favored by terrorists because it is easy to produce and the components are readily available. By using a mid-IR QCL excitation source, one can directly probe TATP in its native form without using other reagents to label, tag or form complexes, as described in the previous chapters. After placing a small amount of dry TATP crystals in a sealed gas cell, a QCL excitation beam is used to probe a small amount of TATP vapor escaping from the crystals. The important TATP mid-IR spectral features

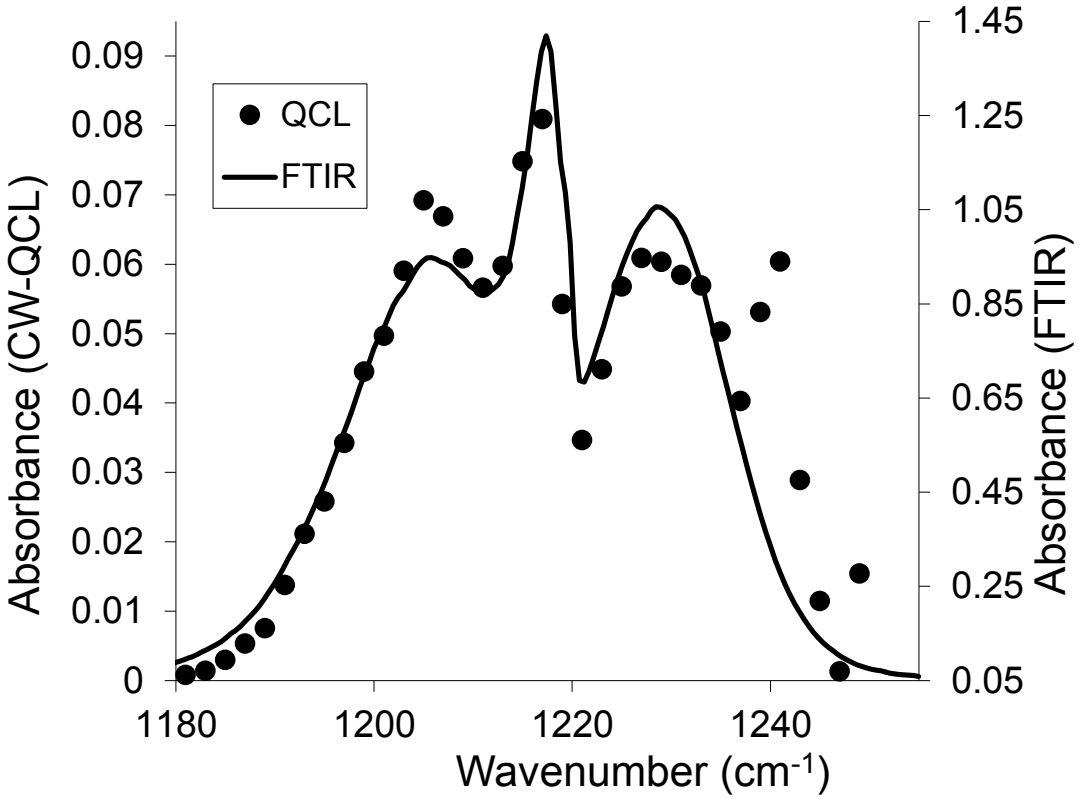

FIGURE 6.6 Absorption spectrum of gas-phase acetone collected by a continuous-wave quantum cascade laser. It agrees with the FT-IR spectrum.

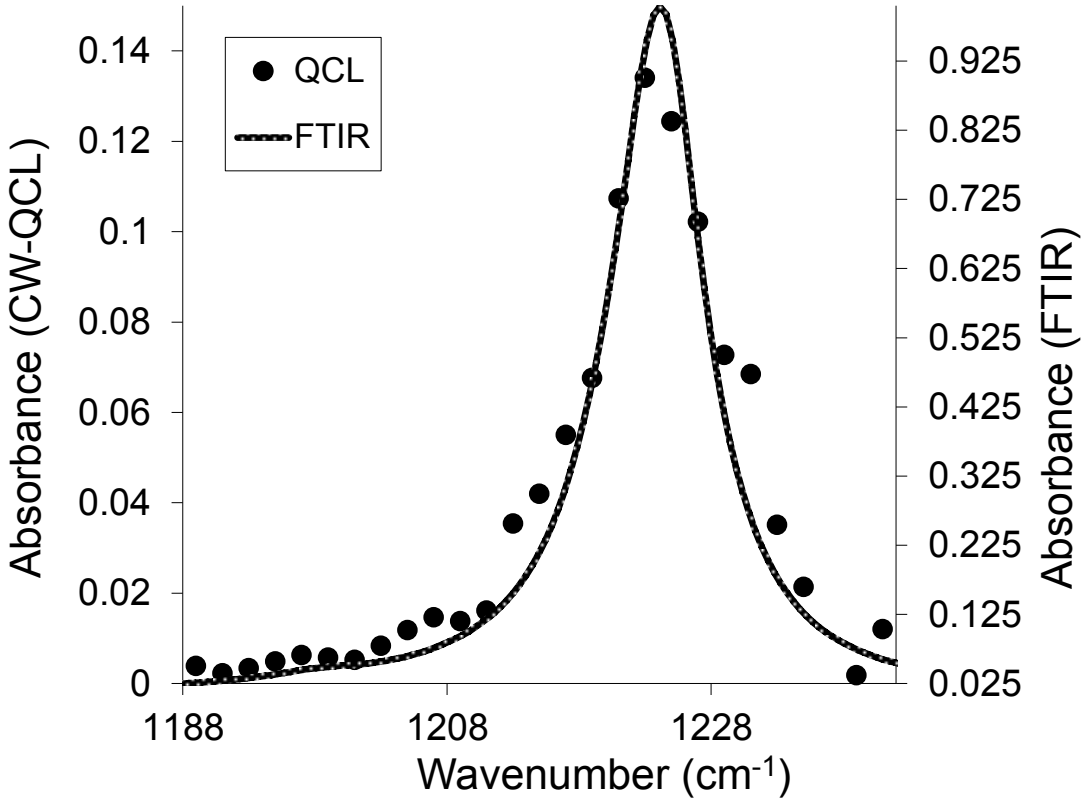

FIGURE 6.7 Absorption spectrum of acetone dissolved in methylene chloride collected by a continuous-wave quantum cascade laser. It agrees with the FT-IR spectrum.

that are probed, as described below, include the O-C-O stretching vibration at 1195 cm^{-1}, the Me-C-Me asymmetric stretching mode, the Me-C-O symmetric stretching mode [14] and the C-O-O stretching mode [15].

6.3.3.1 Triacetone Triperoxide Vapor Detection (1153 - 1223 cm^{-1} Pulsed QCL)

FIGURE 6.8 shows the pulsed QCL absorption spectrum of TATP vapor that is probed above 25 mg of TATP crystals deposited in a sealed 10-cm gas cell. The sample is allowed to sublimate before probing with the beam. The absorption spectrum collected within the tuning range of this pulsed QCL from 1153 to 1223 cm^{-1} compares well to the reference FT-IR spectrum of gas-phase TATP.

6.3.3.2 Triacetone Triperoxide Liquid Detection (1153 – 1223 cm^{-1} Pulsed QCL)

TATP is readily soluble in methylene chloride and the NIST FT-IR data show that methylene chloride has no mid-IR absorption within the tuning range of our pulsed QCL (1153 - 1223 cm^{-1}). Hence, methylene chloride is used as the solvent to prepare trace-concentration TATP solutions for our QCL absorption detection method. **FIGURE 6.9** shows the QCL absorption spectrum of 1 mg/mL TATP in methylene chloride with a peak at 1183 cm^{-1} and a shoulder at 1203 cm^{-1}. Our pulsed QCL absorption spectrum agrees well with the FT-IR spectrum. A

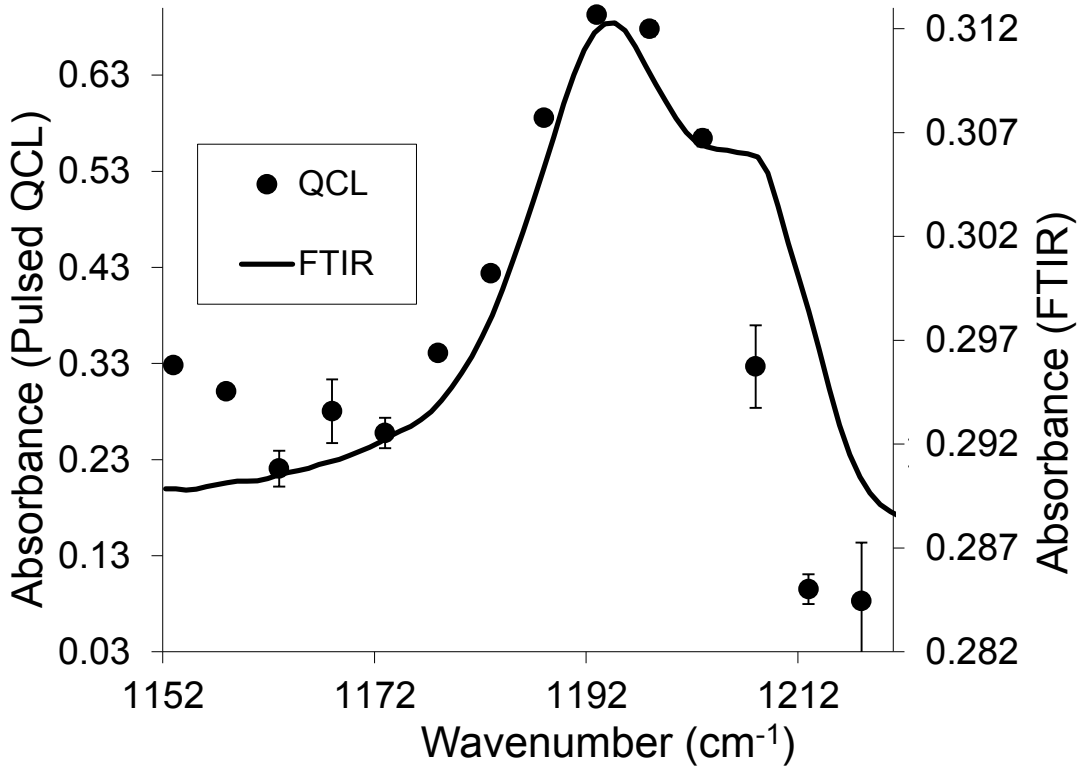

FIGURE 6.8: Absorption spectrum of TATP vapor escaping from crystals in a 10-cm cell collected by a QCL.

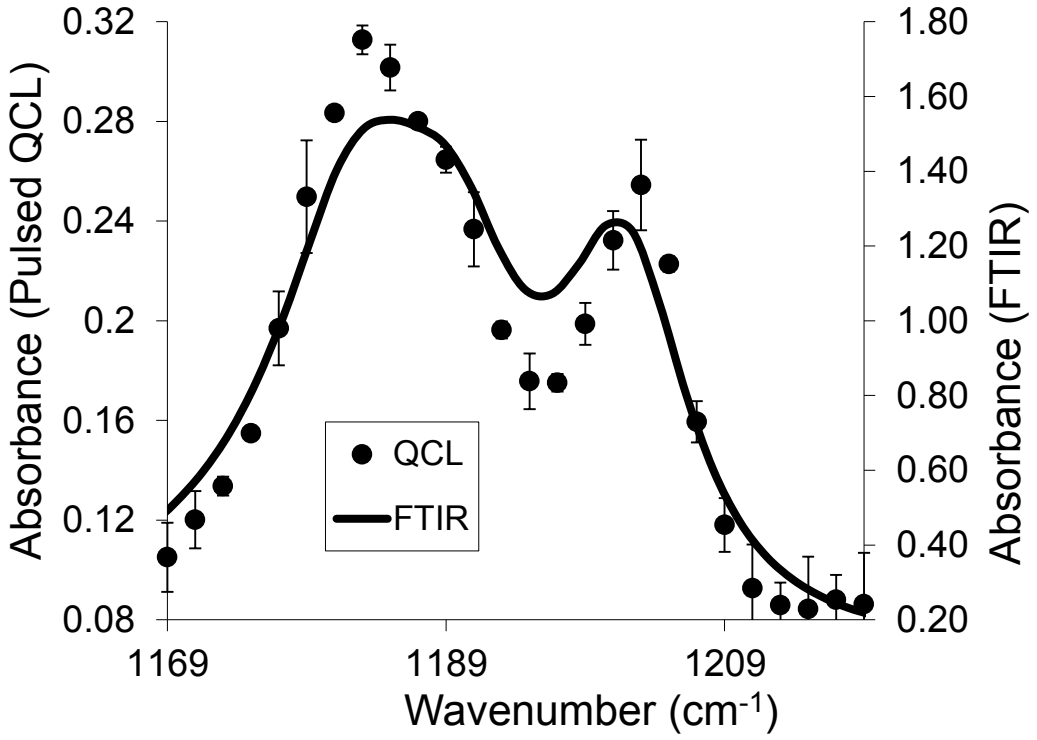

FIGURE 6.9: Absorption spectrum of 1 mg/mL TATP in methylene chloride collected by a QCL. It matches the FT-IR spectrum.

preliminary concentration detection limit of 31 ng/mL (S/N of 2) is determined for TATP based on the spectrum collected with a S/N of 335.

6.3.3.3 Triacetone Triperoxide Vapor (1155 – 1255 cm^{-1} Continuous-Wave QCL)

A trace amount of ttriacetone triperoxide vapor escaping from a small amount of TATP crystals is probed using a continuous-wave QCL with a slightly different tuning range (1155 to 1255 cm^{-1}). The TATP concentration in the vapor increases with increasing temperature. By adjusting the cell temperature, one can vary the TATP concentration in the vapor above the crystals. **FIGURE 6.10** shows how the percent transmission changes with cell temperature at 1195 cm^{-1}. As expected, a lower cell temperature leads to a higher percent transmission. As the temperature increases, the vapor pressure of TATP increases, thus reducing percent transmission. The cell is heated as evenly as possible by simply heating the room air around the cell using simple heat guns. The temperature is monitored using a digital IR temperature probe.

FIGURE 6.11 shows the absorption spectrum of TATP vapor in a sealed 10-cm cell at 47° C collected by a continuous wave QCL with a tuning range from 1155 to 1255 cm^{-1}. It agrees well with the reference gas-phase TATP FT-IR spectrum.

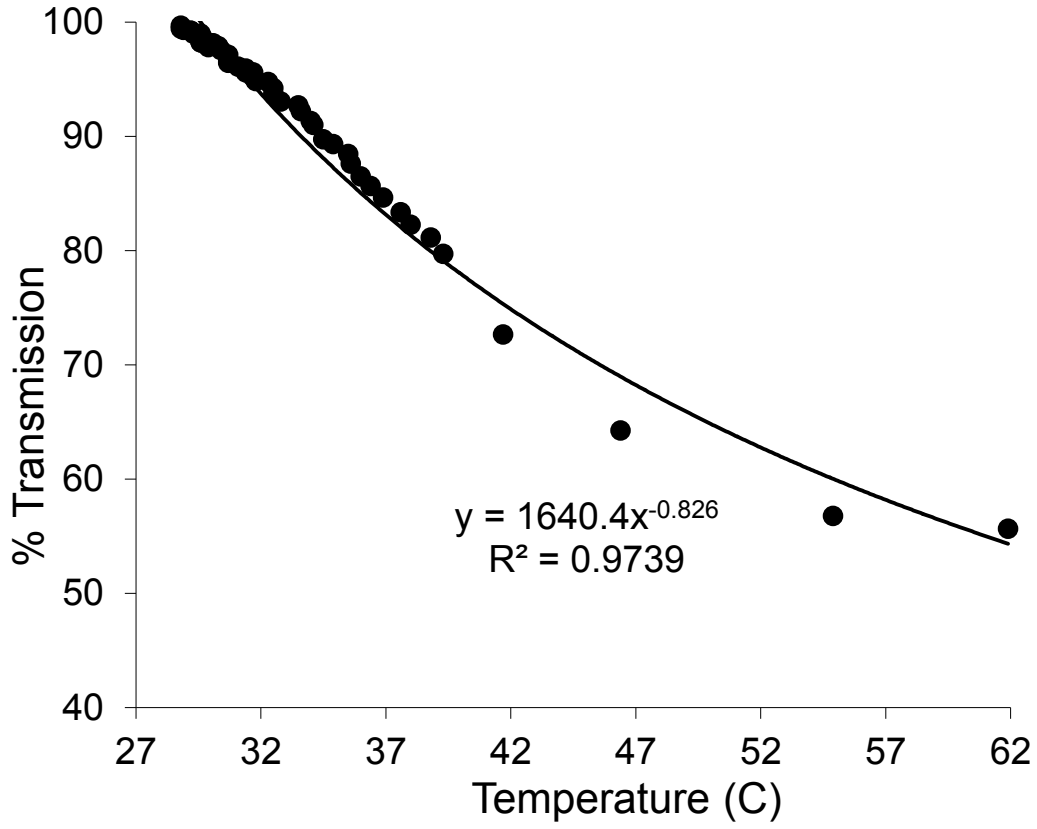

FIGURE 6.10 Change in TATP percent transmission based on temperature change.

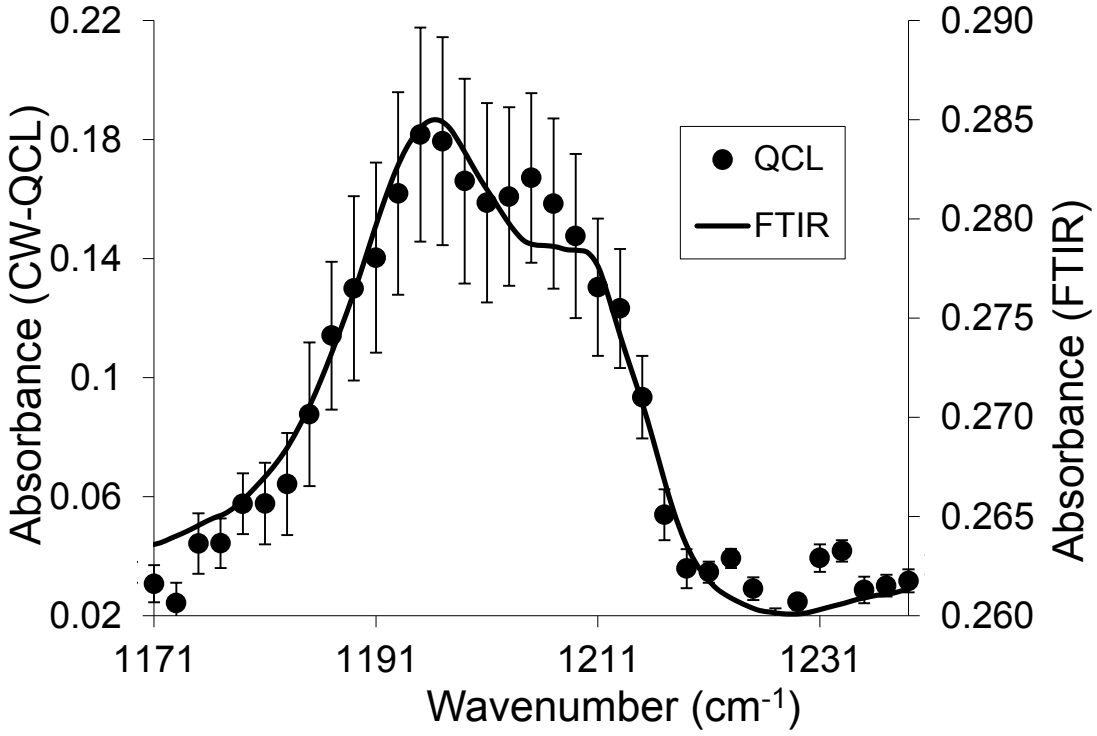

FIGURE 6.11 Absorption spectrum of TATP vapor at 47 C collected by a QCL. It matches with the FT-IR spectrum.

6.3.3.4 Triacetone Triperoxide in Liquid (1155 – 1255 cm^{-1} Continuous-Wave QCL)

FIGURE 6.12 shows an absorption spectrum of 500 µg/mL TATP dissolved in methylene chloride. The spectrum is collected using a continuous wave QCL with a tuning range from 1155 to 1255 cm^{-1}. It agrees well the FT-IR spectrum. A preliminary concentration detection limit of 44 pg/mL (S/N of 2) is determined for a TATP solution based on the spectrum collected with a S/N of 10.5.

6.4 Conclusions

Development of sensitive detection methods for explosives and chem/bio agents remains an area of active research. Simplified laser-based absorption detection methods using mid-infrared quantum cascade lasers offer many advantages including the ability to detect many compounds in their native form. The ability to detect an analyte in its native form eliminates the need for labeling, tagging and other sample preparation steps. This work demonstrates the detection of 2, 4-dinitrotoluene, acetone and triacetone triperoxide in liquid- and gas-phase analytes using simple tunable pulsed or continuous-wave mid-IR quantum cascade lasers.

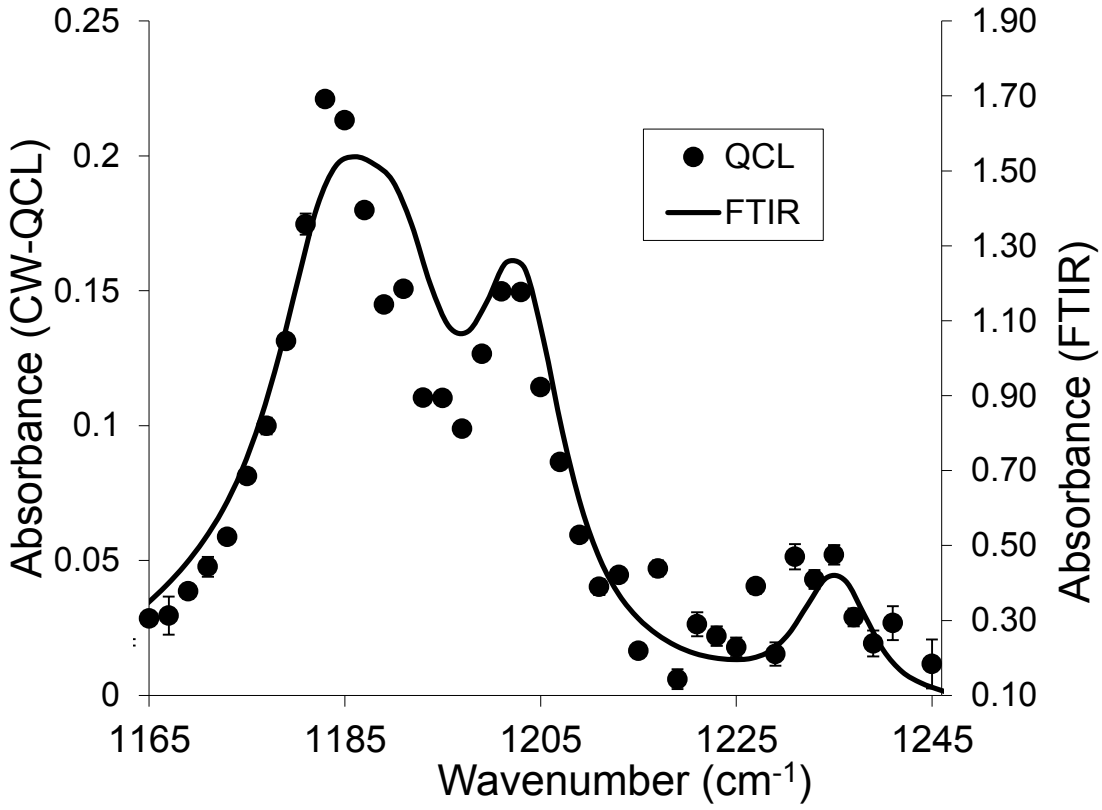

FIGURE 6.12 Absorption spectrum of 500 ug/mL TATP dissolved in carbon disulfide collected by a continuous-wave QCL. It matches the FT-IR spectrum.

REFERENCES

1. Lyons, WJ: *PhD Dissertation*, **2009**, UCSD.

2. McManus, JB; Shorter, JH; Nelson, DD; Zahniser, MS; Glenn, DE; McGovern, RM: *Appl. Phys. B* **2008**, 92, 387-392.

3. O'Keefe, A; Deacon, DAG: *Rev. Sci. Instrum.* **1988**, 59, 2544-2551.

4. Gagliardi, G; Borri, S; Tamassia; Capasso, F; Gmachl, C; Sivco, DL; Baillargeon, JN; Hutchinson, AL; Cho, AY: *Isotopes in Environmental and Health Studies* **2005**, 41, 313-321.

5. Mickadeit, F; Bernoilles, S; Kemp, HR; Tong, WG: *Anal. Chem.* **2004**, *76*, 1788-1792.

6. Jenkins, T.F.; Walsh, M.E. *Talanta.* **1992,** 39(4), 419-428.

7. http://www.epa.gov/ttn/atw/hlthef/dini-lue.html

8. Esteve-Nunez, A.; Caballero, A.; Ramos, J.L. *Microbiology and Molecular Biology Reviews.* **2001,** 65(3), 335-352.

9. Skoog, D., Holler, J., Crouch, S. Principles of Instrumental Analysis; 6th Ed., Thomson Brooks/Cole: Belmont, 2007.Dokken, KM; *PhD Dissertation*, **2006**, Kansas State University.

10. www.sigmaaldrich.com/catalog/product/sial/650501?lang=en&region=US

11. Oxley, JC; Smith, JL; Shindem K; Moran, J: *Propellants, Explosives, Pyrotechnics,* **2005**, *30(2),* 127- 130.

12. Max, JJ; Chapados, C: *Journal of Chemical Physics,* **2007**, *126*, 154511-1 – 154511-9.

13. Oxley, J; Smith, J; Brady, J; Dubnikova, F; Kosloff, R; Zeiri, L; Zeiri, Y: *Applied Spectroscopy*, **2008**, *62(8)*, 906-915.

14. Pretsch, E; Buhlman, P; Affolter, C: Structure Determination of Organic Compounds, Springer-Verlag, Berlin, Heidleberg, New York, 2000; Chapter 4.

Chapter 7

Mid-IR Laser Wave-Mixing Spectroscopy Using Quantum Cascade Lasers

7.1 Introduction

The use of quantum cascade lasers (QCL) in mid-IR laser wave-mixing spectroscopy allows chemical analysis in the molecular fingerprint region while using a relatively compact solid-state mid-IR light source. Acetone is a volatile organic compound of interest in a wide range of areas including atmospheric chemistry, disease diagnosis, and as a precursor to the manufacture of triacetone triperoxide. Acetone is also shown to increase the amount of HO_2 and peroxyl acyl nitrates (PAN's) in the upper troposphere [1]. The formation of HO2 and PAN, in turn, has an effect on ozone concentration levels [2]. Acetone is ubiquitous in the atmosphere with concentrations in the ppbv range.

Diabetes is an endemic disease that typically requires a blood draw to determine glucose and glycosylated hemoglobin (HbA1c %) levels in blood [3]. In a healthy human, breath acetone concentration levels are in the ppbv range, with concentrations increasing into the ppmv range for patients with diabetes [4]. Research has also linked high levels of breath acetone in patients with congestive heart failure, which leads to excessive production of ketones due to a relative shift from carbohydrate to fat metabolism (lipolysis) as an energy source [5]. Burning of fat as a part of a dietary program can also be monitored using breath acetone measurements [6]. Acetone is also one of three reagents needed to produce triacetone triperoxide [7]. It has a relatively high vapor pressure and it

absorbs light in the mid-IR region from 1155 to 1255 cm^{-1}. Hence, a fast, sensitive, cost effective, non-invasive detection technique is needed in many areas including diabetes research and other biomedical and environmental applications.

7.2 Experimental Setup

The QCL wave-mixing experimental setup is similar to those described previously for visible-laser wave-mixing setups. A QCL supplies the input beams needed for our two-beam forward-scattering wave-mixing setup. Gas-phase samples are probed inside a 10-cm gas cell with BaF_2 windows (Curtis Technology, San Diego, CA). The cell has three inlet/outlet arms. Two ¼-inch diameter arms are used for attachment to vacuum and gas lines and a ½-inch diameter arm is used for introduction of solid or liquid samples. In addition to this enclosed cell, an acetone vapor jet system is also used where a stream of air introduced over acetone deposited at the bottom of a bottle generates an analyte vapor jet that can be probed, as described previously in Chapter 6. Liquid-phase samples are probed using an adjustable path length IR cell (Crystal Labs, Garfield, NJ) that uses multiple width Teflon rings to change its path length. The wave-mixing signal is collected using a solid-state mid-IR detector. One of the input beams is modulated using an optical chopper (Stanford Research Systems, SR540, Sunnyvale, CA) and the signal is collected using a lock-in amplifier (Stanford Research Systems, SR810, Sunnyvale, CA) and digitized using a custom designed AIDA data acquisition program.

Before detecting acetone at trace concentration levels, we compare a few solvents that may be appropriate for the continuous-wave QCL wavelength tuning range. **FIGURE 7.1** shows comparison of methylene chloride and carbon disulfide as solvents for acetone**.** Methylene chloride shows a significant amount of optical absorption, and hence, background laser wave-mixing signal. As expected, carbon disulfide also shows a small wave-mixing signal due to its nonlinear properties even though it has no optical absorption. Hence, carbon disulfide is a more appropriate solvent for acetone in the liquid phase.

In the gas phase, methylene chloride is used as the solvent for acetone since it has a higher vapor pressure and it can more readily vaporize in the gas cell. It is also a good solvent for acetone and it allows efficient transport of trace amounts of acetone vapor inside the gas cell. Methylene chloride generates a small background signal in the QCL wavelength range; however, the background signal is still much smaller than that of an acetone/methylene chloride solution. The background signal is subtracted from the total signal and only the net wave-mixing signal is reported in our work.

For liquid-phase analytes, the laser wave-mixing signal is usually modulated at a relative low frequency (400 Hz) to avoid grating wash out. However, our mid-IR photodetector used in this work is an AC coupled photoconductive system with a thermoelectric cooler that operates with a bandwidth of 10 kHz. As expected and as shown in **FIGURE 7.2,** the strongest wave-mixing signal is observed at 4 kHz, the highest chopping frequency available from our mechanical optical chopper. Although one could maintain

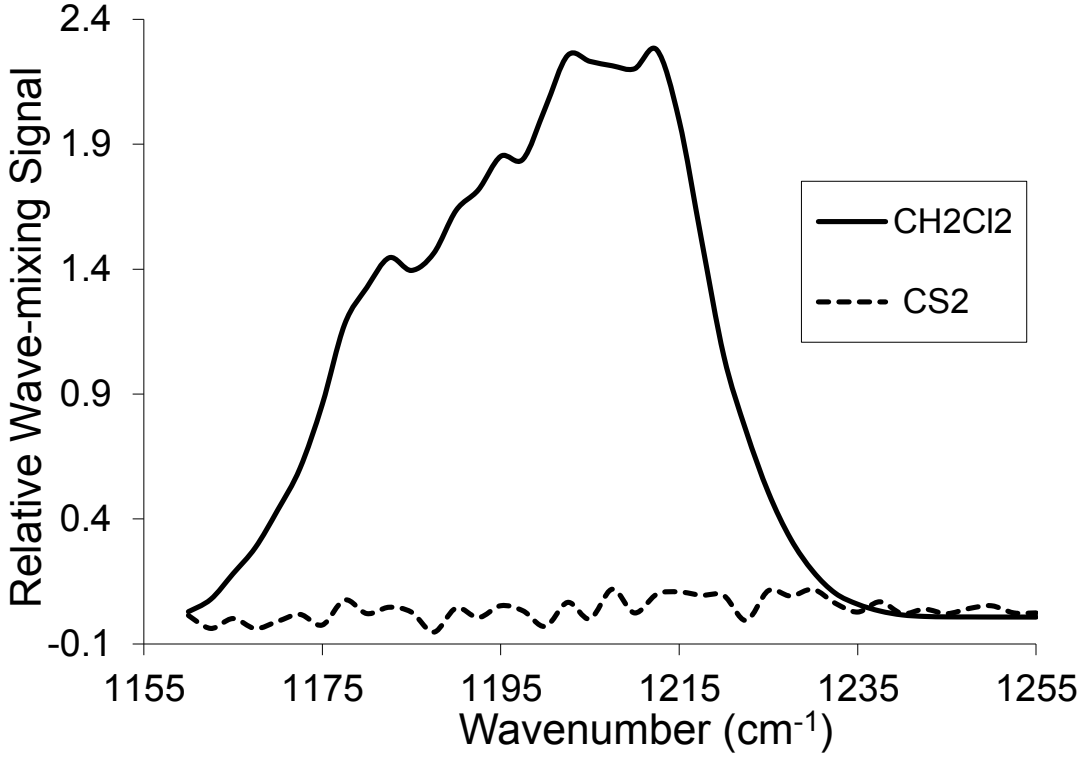

FIGURE 7.1 Comparison of methylene chloride and carbon disulfide as a solvent for acetone. Carbon disulfide has a small baseline absorption with no major peaks that could interfere with acetone.

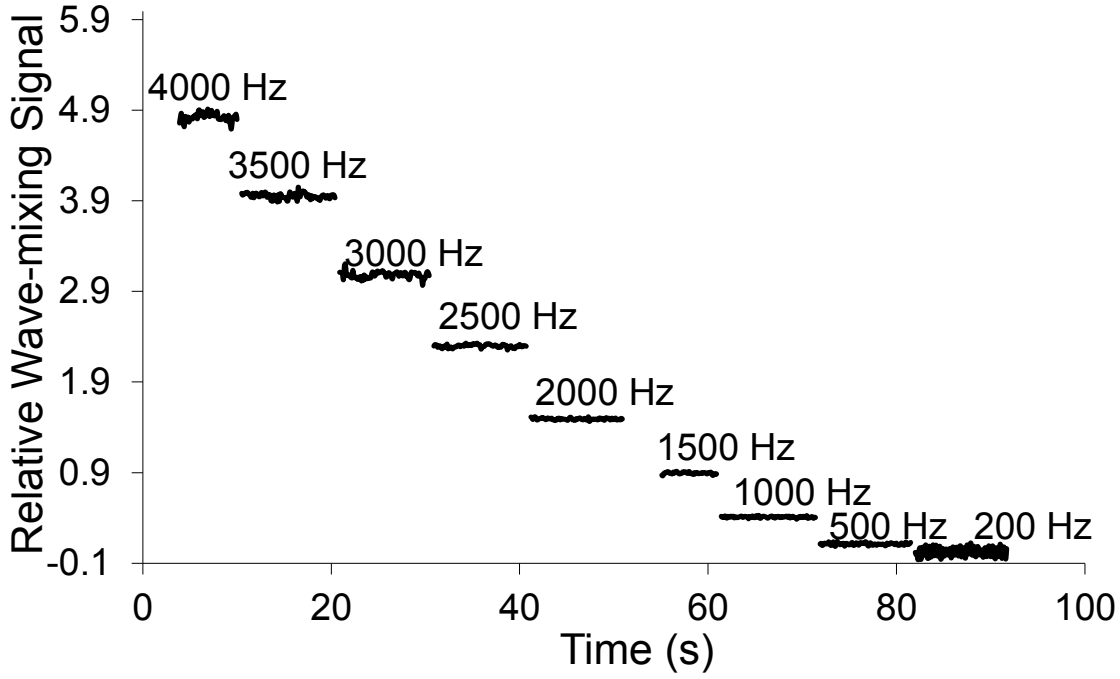

FIGURE 7.2 Comparison of signal and S/N levels at different optical chopper frequencies for the detection of acetone in the liquid phase.

sharper gratings and gain some wave-mixing signal enhancement by lower the modulation frequency, the signal loss at the mid-IR photodetector is more significant. Hence, a modulation frequency of 4 kHz is used with this mid-IR detector.

7.3 QCL Wave-Mixing Detection of Gas-Phase Acetone

The infrared spectrum of acetone is well known and the C=O stretch yields the classic FT-IR peak that is characteristic of acetone and other carbonyl containing compounds. This strong stretching peak in the 1700 - 1750 cm^{-1} range is widely used to identify chemical structures of organic molecules, especially when coupled with data from mass spectrometry and NMR spectroscopy. However, there is another strong line in the FT-IR spectrum that can be used. The bending mode centered on the carbonyl carbon, bounded by the two adjacent methyl carbons, has an infrared absorption in the 1200 cm^{-1} region. The continuous-wave QCL used in this work offers a wavelength tuning range that covers this peak at 1200 cm^{-1} [8].

Acetone is a very strong absorber and the laser wave-mixing signal can be easily concentration saturated at high concentration levels in the gas phase, i.e., a signal dip is observed at the absorption peak, as shown in **FIGURE 7.3**. Instead of a large peak at 1217 cm^{-1}, there is a significant drop in signal at line center when it is concentration saturated. In addition, the signal peak could also be attenuated due to auto-absorption, i.e., the signal beam itself is absorbed and

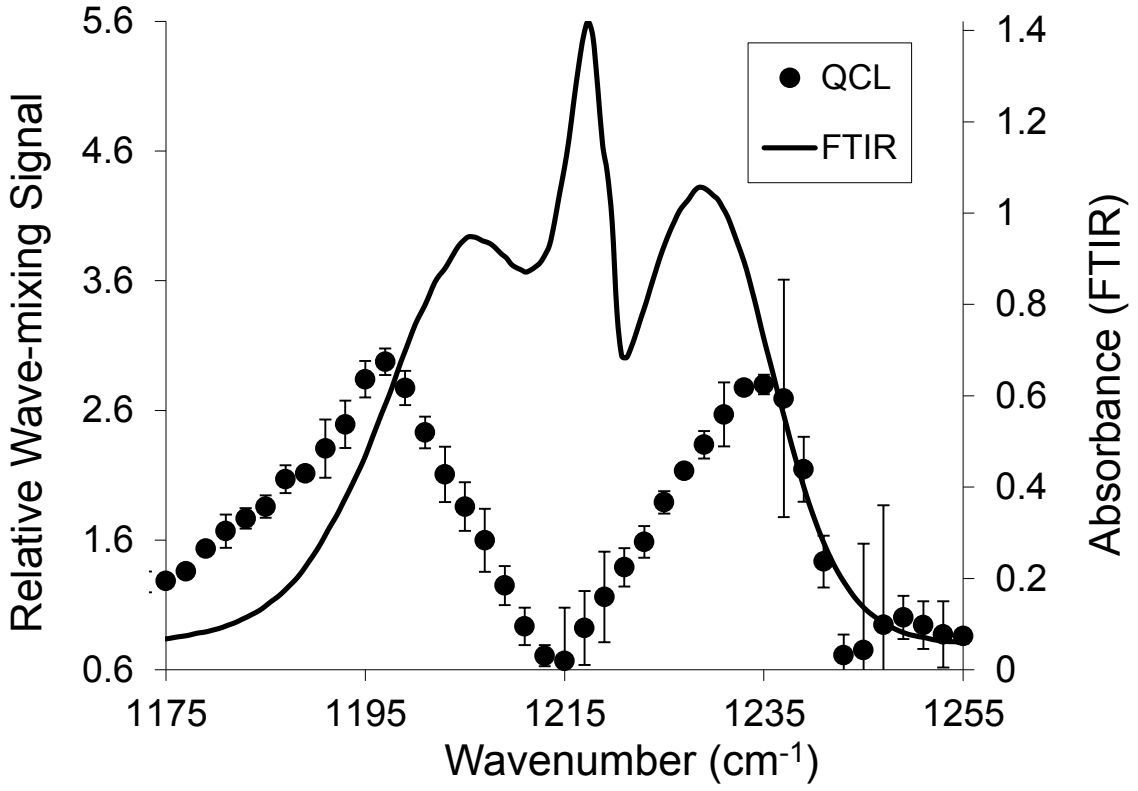

FIGURE 7.3 Comparison of gas-phase acetone wave-mixing spectrum from QCL and absorption spectrum from FT-IR. Acetone is a strong absorber and concentration saturation (a dip) is observed at 1215 cm^{-1} even with only 1 µL of acetone deposited to create the vapor.

could not pass through the analyte when high concentration levels of a strong absorber, such as acetone, is present.

To collect gas-phase QCL wave-mixing spectra of acetone, it is dissolved in methylene chloride so that known amounts of trace-concentration acetone can be introduced into the sample cell. A 1 uL aliquot of the acetone/methylene chloride solution is injected into a 10-cm gas cell with a volume of 50.6mL. The concentration of acetone vapor in the cell is estimated to be 6 ppm.

FIGURE 7.4 shows the central peak at 1217 cm^{-1} and the two shoulders. The QCL wave-mixing signal is confirmed by verifying a cubic dependence on laser power, as shown in **FIGURE 7.5**. Following confirmation of the QCL wave-mixing signal, the detection setup is optimized to yield the best S/N. A series of diluted acetone samples are prepared and probed with the QCL tuned to the 1217 cm^{-1} peak.

FIGURE 7.6 shows detection sensitivity of our QCL wave-mixing method for acetone samples. The blank (methylene chloride) signal is subtracted from the total signal to determine the net signal for acetone. A preliminary concentration detection limit of 1 ppb is determined for acetone in the gas phase. This compares well to detection limits of other gas-phases detection methods as shown in **TABLE 7.1**. Hence, QCL-based mid-IR laser wave mixing offers comparable or better detection sensitivity levels using a compact solid-state detector design that is more portable and less bulky than other methods including GC-MS-based systems.

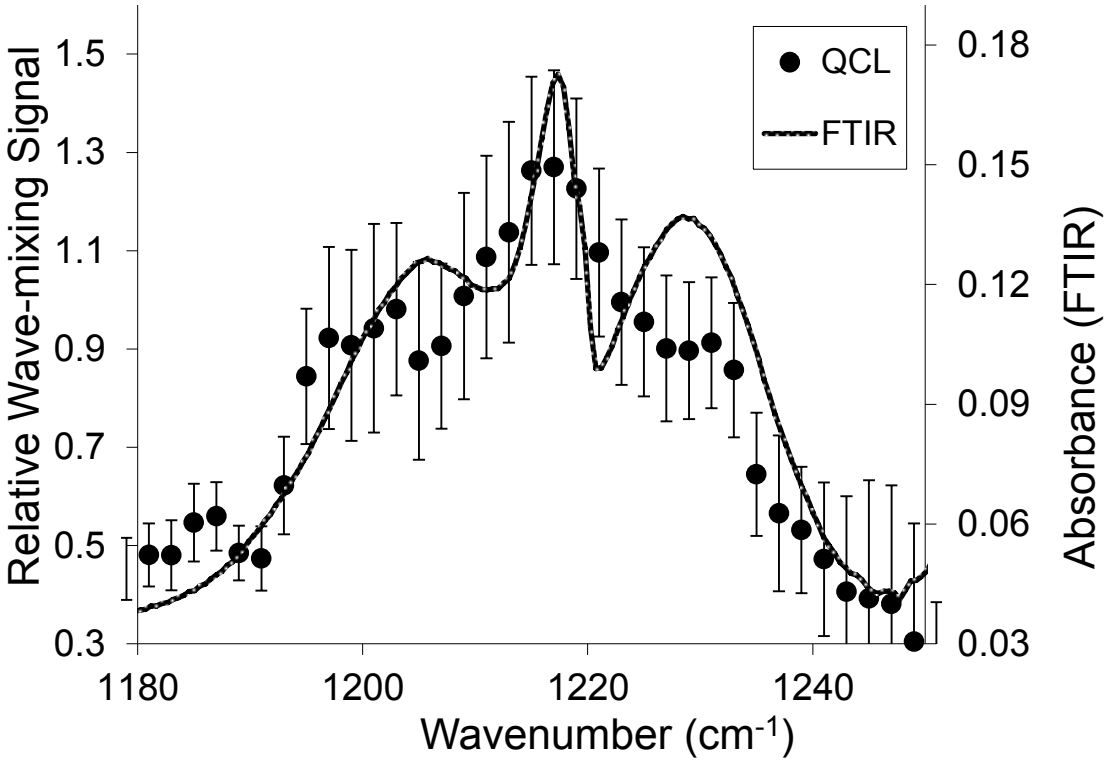

FIGURE 7.4 Laser wave-mixing QCL spectrum of 1 uL of a 1:1000 acetone/methylene chloride solution injected in a 10-cm gas cell compared to a FT-IR spectrum.

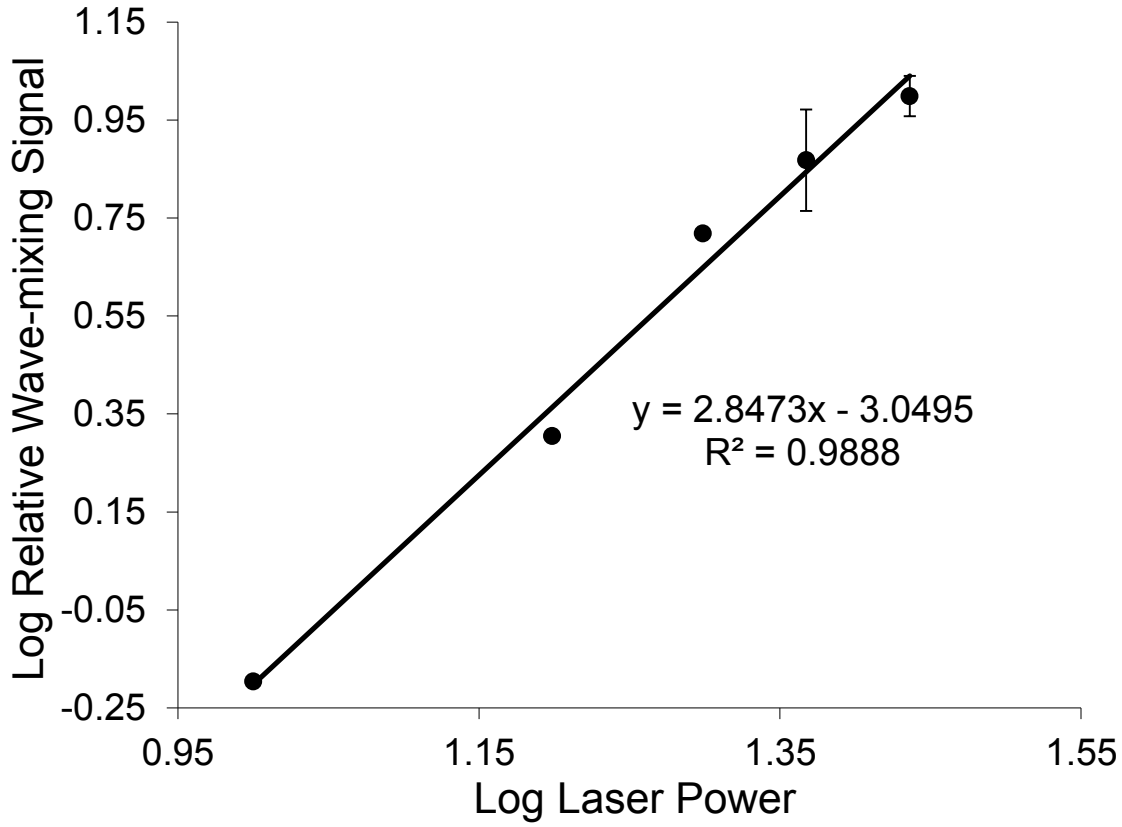

FIGURE 7.5 Cubic dependence on laser power for the gas-phase acetone wave-mixing signal.

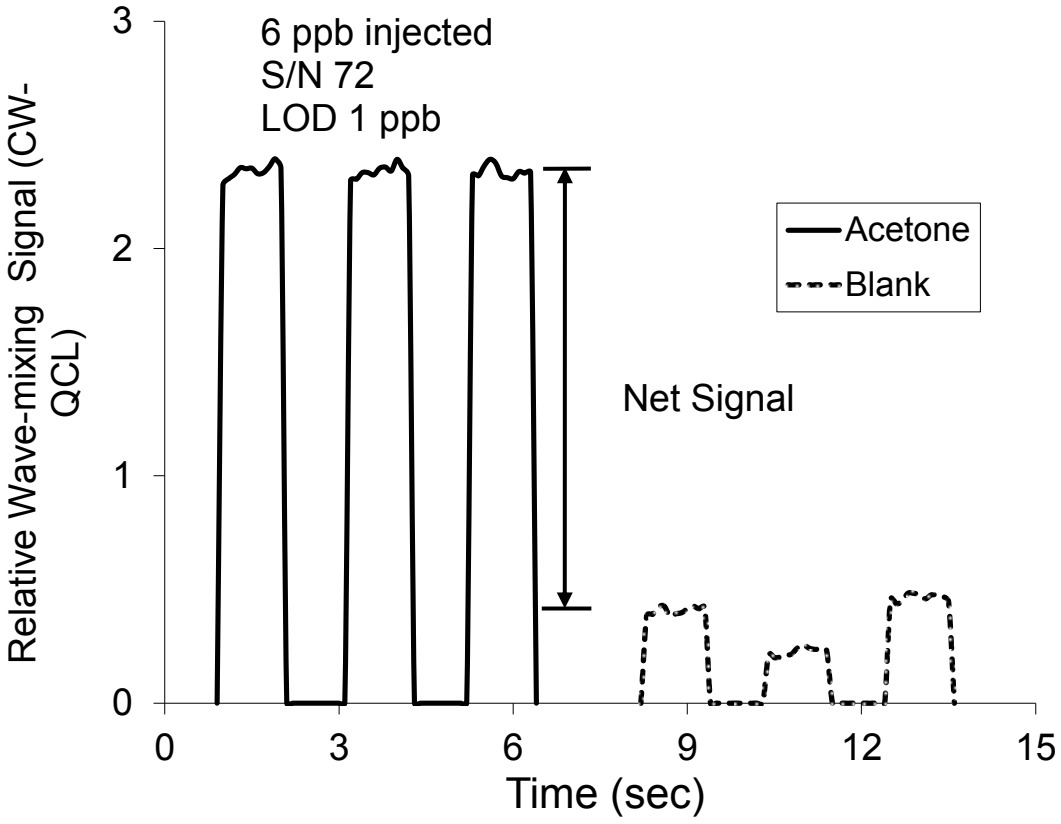

FIGURE 7.6 Wave-mixing detection sensitivity for gas-phase acetone.

7.4 QCL Wave-Mixing Detection of Liquid-Phase Acetone

As expected, there are some differences between gas-phase and liquid-phase FT-IR spectra. The gas-phase acetone spectrum has three distinct peaks centered on 1217 cm^{-1}. When acetone is in a mixture with other solvents, intermolecular interactions affect the spectral profiles. These changes are partly due to changes in the dipole moment of the acetone molecule in the presence of the solvent molecules and the inhibition of stretching and bending due to the close proximity of solvent molecules relative to the freedom of movement acetone has in the gas phase. **FIGURE 7.7** shows the effect of different solvents on the acetone FT-IR spectral profiles. In carbon disulfide, the solvent of choice in this work, liquid-phase acetone yields a peak at 1215 cm^{-1}.

FIGURE 7.8 shows the wave-mixing spectrum of 1:500 diluted acetone in carbon disulfide collected by a continuous-wave QCL. The absorption maximum at 1215 cm^{-1} and the peak width match those of the FT-IR spectrum. Similar to gas-phase high-concentration analytes, liquid-phase analytes could also suffer concentration saturation. When the absorption is strong and the analyte concentration is high, the wave-mixing signal at the line center could be attenuated due to concentration saturation and auto-absorption of the signal beam by the analyte itself.

FIGURE 7.9 shows cubic dependence on laser power for liquid-phase acetone, confirming the nonlinear laser wave-mixing signal. For detection limit calculations, it is important to determine the net signal generated by the analyte since some solvents yield background wave-mixing signal. For example, carbon

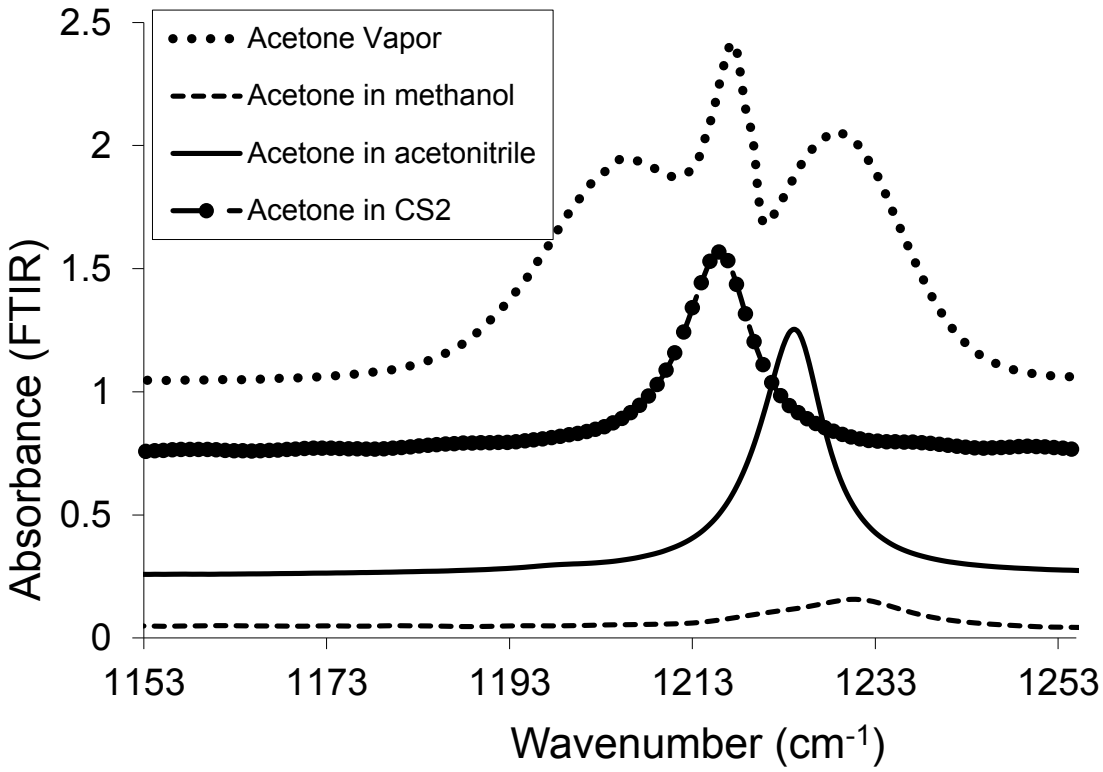

FIGURE 7.7 Comparison of acetone FT-IR spectra, showing different phase and solvent effects.

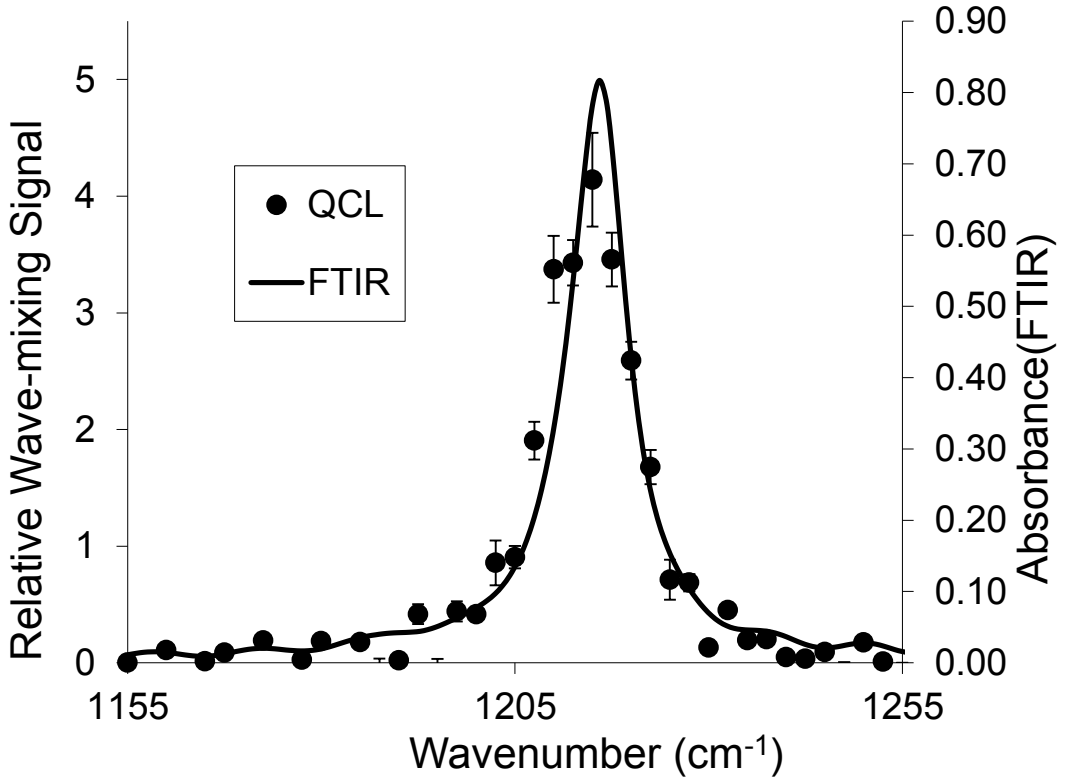

FIGURE 7.8 Wave-mixing QCL spectrum of 1:500 diluted acetone in carbon disulfide with the peak at 1215 cm^{-1}. It matches well with the FT-IR spectrum.

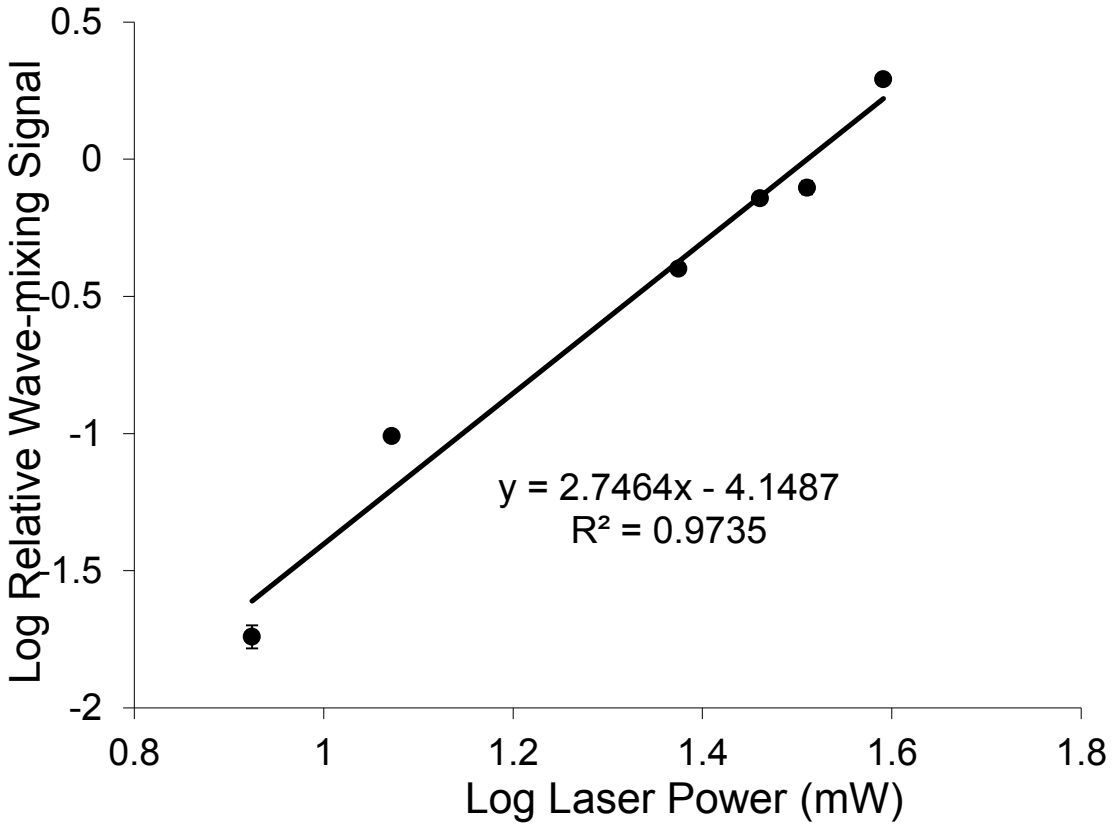

FIGURE 7.9 Cubic dependence on laser power for the wave-mixing signal of 1:500 diluted acetone in carbon disulfide. Error bars are too small to be seen since they are within the dot at each point on the graph.

disulfide yields a small wave-mixing signal due to its third-order nonlinear susceptibility $\chi^{(3)}$. Hence, it is important to monitor this background signal and only use the net signal generated by the analyte when determining detection limits.

FIGURE 7.10 shows detection sensitivity of the wave-mixing signal for liquid-phase acetone using a continuous-wave QCL. Using the "net" wave-mixing signal generated, a preliminary concentration detection limit of 1.25×10^{-10} M is determined for acetone. As shown in **TABLE 7.1,** our detection limit is comparable or better than those of other sensitive methods while offering unique advantages including small portable detector designs, robustness, enhanced chemical specificity levels, and detection of analytes in their native form.

7.5 Conclusions

Acetone is a molecule of interest across a range of disciplines. It has many potential applications in a wide range of areas including as a disease biomarker, for diabetic control, and as an important chemical in atmospheric chemistry and security/defense applications. The work presented here shows that both gas-phase and liquid-phase acetone can be detected with excellent sensitively levels using a compact laser wave-mixing setup based on a mid-IR tunable solid-state continuous-wave quantum cascade laser.

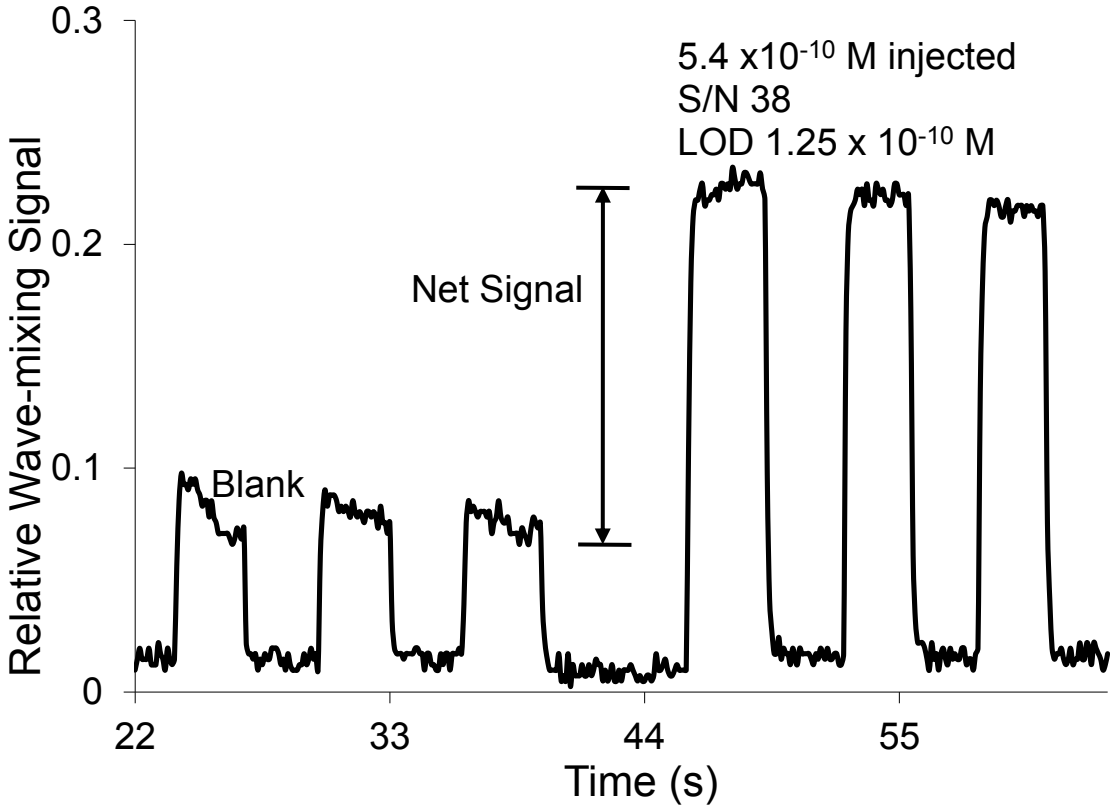

FIGURE 7.10 QCL wave-mixing detection sensitivity for acetone in carbon disulfide.

TABLE 7.1 Comparison of Gas-Phase Detection Methods

Method	LOD	Ref
Quartz enhanced photoacoustic spectroscopy	70 ppb	Journal of Breath Research, **2007**, 1, R1-R12
Si:WO_3 nanoparticle sensor	20 ppb	Analytical Chemistry, **2010**, 82, 3581-3587
In-needle pre-concentration and GC-MS	0.5 ppb	Journal of Chromatography B, **2009**, 877, 2551–2556
Nanostructured copolymers	1 ppm	Nano Letters, **2006**, 6(8), 1598-1602
Ultrasonic transducers	3.5 ppm	Appl Phys Lett, **2007,** 91, 094102-1 - 094102-3
Laser Wave Mixing	1 ppb	This work

REFERENCES

1. Wohlfrom, KH; Hauler, T; Arnold, F; Singh, H*: Geophysical Research Letters.* **1999**, *26(18),* 2849-2852.

2. Stockwell, WR; Milford, JB; Gao, D; Yang, YJ; *Atmospheric Environment,* **1995**, *29(14)*, 1591- 1599.

3. Ueta, I; Saito, Y; Hosoe, M; Okamoto, M; Ohkita, H; Shirai, S; Tamura, H; Jinno, K: *Journal Chromatography B*, **2009**, *877*, 2551-2556.

4. Deng, C; Zhang, J; Yu, X; Zhang, W; Zhang, X: *Journal Chromatography B*, **2004**, 269-275.

5. Kupari, M; Lommi, J; Ventila, M; Karjalainen, U: *American Journal of Cardiology*, **1995**, *76*, 1076-1078.

6. Kundu, SK; Bruzek, JA; Nair, R; Judilla, AM: *Clinical Chemistry*, **1993**, *39(1)*, 87-92.

7. Dubnikova, F; Kosloff, R; Almog, J; Zeiri, Y; Boese, R; Itzhaky, H; Alt, A; Keinan, E: *Journal of the American Chemical Society*, **2008**, *127(4)*, 1146-1159.

8. Pretsch, E; Buhlman, P; Affolter, C: Structure Determination of Organic Compounds, Springer-Verlag, Berlin, Heidleberg, New York, 2000; Chapter 4.

Chapter 8

Mid-IR Wave-Mixing Detection of Triacetone Triperoxide Using Quantum Cascade Lasers

8.1 Introduction

Quantum cascade lasers (QCL) have opened up new areas of analytical spectroscopy, especially when coupled to nonlinear wave-mixing spectroscopy. In this work, different QCLs are explored and tested for sensitive detection of triacetone triperoxide (TATP) and acetone, both for gas-phase and liquid-phase analytes.

Triacetone triperoxide is excited and probed over different mid-IR wavelength ranges to explore its characteristic spectral features. Since TATP does not absorb UV or visible light, one cannot use UV or visible lasers to detect TATP unless it is detected indirectly or through complexation [1]. TATP yields strong absorption peaks in the mid-IR range and one can use mid-IR laser spectroscopic detection effectively, especially by taking advantage of the unique features of a quantum cascade laser. TATP has a relatively low vapor pressure; however, it is still higher than those of other explosive chemicals including TNT, PETN and RDX, as shown in **TABLE 8.1** [2]. In this work, we demonstrate sensitive detection of liquid-phase TATP and gas-phase TATP using a compact portable mid-IR QCL-based wave-mixing detector.

TABLE 8.1 Comparison of vapor pressures of various explosives

Explosive	MW	Vapor Pressure at 20°C, Pa	Vapor Pressure at 100°C, Pa
EGDN	152	5.2	2300
NG	227	0.03-0.2	55
TATP	222	0.4	31000
2,4-DNT	182	2.5	
TNT	227	0.001	5 to 15
PETN	316	$1x10^{-6}$	$9x10^{-4}$
RDX	222	$1x10^{-7}$	$9x10^{-5}$
From *Propellants, Explosives, Pyrotechnics,* **2005,** pg 130			

8.2 Experimental Setup

The wave-mixing experimental setup is similar to those discussed in previous sections of this dissertation. The QCL output beam is split to generate two input beams for our two-beam forward-scattering wave-mixing setup. Gas-phase TATP samples are probed using a 10-cm gas cell with BaF_2 windows (Curtis Technology, San Diego, CA). Liquid-phase TATP samples are probed using an adjustable IR cell (Crystal Labs, Garfield, NJ) that uses different Teflon rings to change the path length of the cell. The wave-mixing signal is collected using a solid-state photodetector. The wave-mixing signal is modulated using an optical chopper (Stanford Research Systems, SR540, Sunnyvale, CA) and collected using a lock-in amplifier (Stanford Research Systems, SR810, Sunnyvale, CA). The signal is then digitized and stored using a custom-designed data acquisition program (AIDA).

The QCL light source is used both in the DFWM detection mode and in the transmission detection modes. To operate in the transmission mode, the unchopped input beam is blocked so that single-beam infrared transmission measurements can be made. The QCL is also switched to the pulsed mode and operated at very low rep rates (2.5 kHz). This reduces the QCL output power significantly, preventing power saturation at the detector. The laser controller is used to trigger the lock-in amplifier and the transmission signal is converted to optical absorbance using Beer's Law:

$$A = - \log I/I_o$$

where I_o is the transmission intensity of a blank and I is the transmission intensity of the analyte.

8.3 QCL with 1195 to 1280 cm^{-1} Tuning Range

This QCL is operated in the pulsed mode at 100 kHz rep rate to probe TATP vapor escaping from a small amount of crystalline TATP deposited inside the 10-cm gas-phase cell. The QCL output power is high at the center of the tuning range and lower at the extremes of the tuning range. Furthermore, the laser wave-mixing signal has a cubic dependence on laser power, hence, it is important that the wave-mixing spectrum collected by a QCL be power normalized in order to measure the spectral profile more accurately. **FIGURE 8.1** shows a QCL wave-mixing spectrum collected with a 5 cm^{-1} scan interval. This wave-mixing spectrum shares similar features with the FT-IR spectrum, especially the large peak at 1195 cm^{-1}. Previously published spectra also show the secondary TATP peaks at 1240 and 1260 cm^{-1} [1]. The 5 cm^{-1} scan interval used for this QCL does not yield high spectral resolution in order to accurately capture some of these minor spectral features.

FIGURE 8.2 shows cubic dependence on power for the wave-mixing signal collected by this QCL at 1195 cm^{-1}. The laser power is varied by modulating the QCL laser current on the controller. This particular QCL does not yield a good power stability level and the resulting error bars are relatively long.

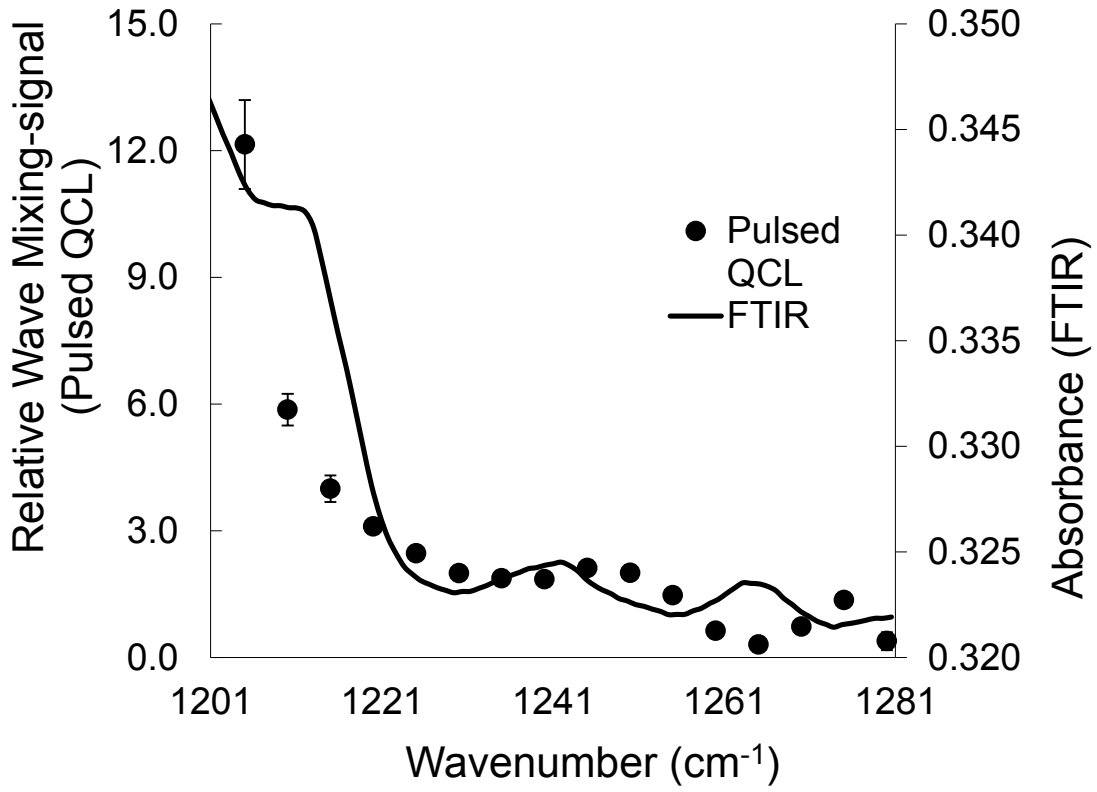

FIGURE 8.1 Wave-mixing TATP spectrum collected by a pulsed QCL from 1195 to 1280 cm^{-1} with a 5 cm^{-1} scan interval and normalized for laser output power. Three expected peaks are present, but shifted as compared to the FT-IR spectrum.

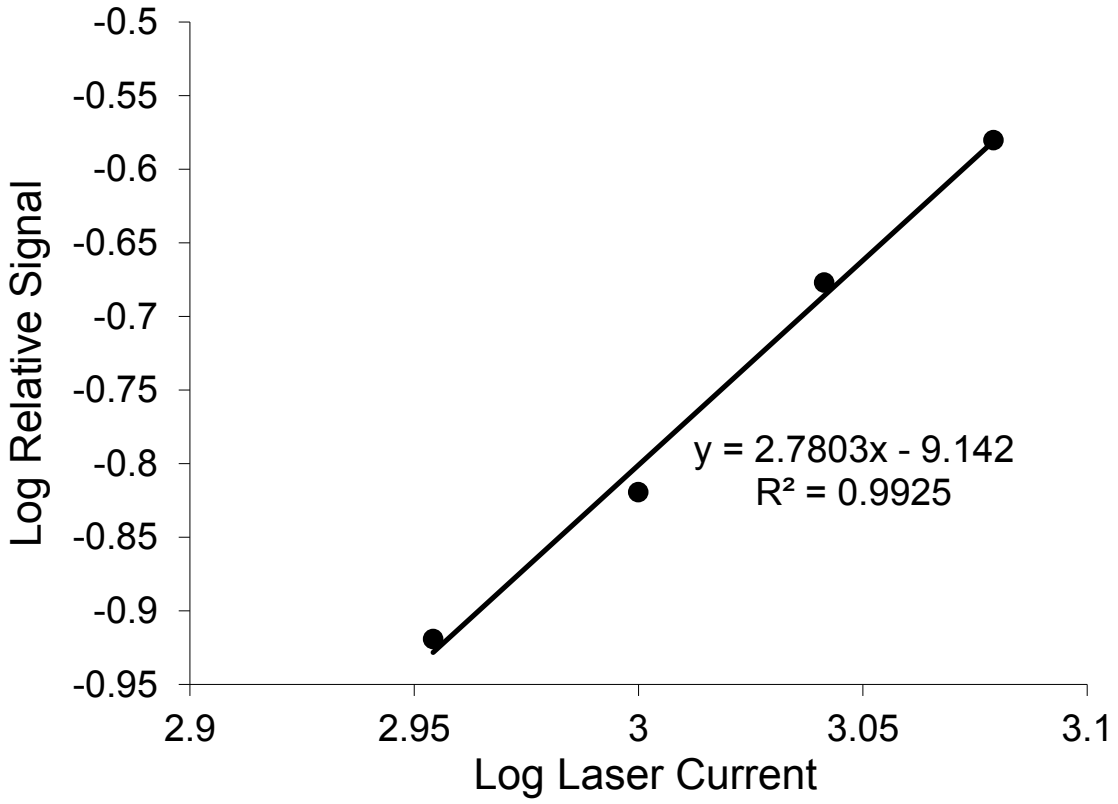

FIGURE 8.2 Cubic dependence on laser power for the wave-mixing signal of TATP at 1195 cm^{-1} using QCL current-modulated detection setup.

When using TATP crystals to generate TATP vapor for the laser probe volume, the concentration of the TATP vapor is estimated using the Clapyeron equation [3]:

$$\text{Log}_{10} P = A - B/T$$

$$A = 15.855$$

$$B = 4490$$

Using this equation, one can determine the vapor pressure to be 0.0364 Torr at 25 C. Using a rearranged form of the universal gas law,

$$m = pVM/RT$$

and the 0.05 L cell volume, V, the mass, m, of TATP in the cell is estimated to be 2.18×10^{-5} g. This corresponds to 436 ng/mL or 436 ppb. Using the equation for determining LOD at S/N of 2,

$$\text{LOD} = (\text{ppb})\ (\text{sq rt}\ (2/\text{S/N}))$$

A preliminary concentration detection limit of 77 ppb is determined based on the measured signal with a S/N of 63. Our first QCL allows us to measure a wave-mixing spectrum with peaks at 1195, 1235 and 1260 cm^{-1}. Our mid-IR wave-mixing spectrum agrees with the FT-IR spectrum and the spectrum previously reported for this wavelength range. This QCL also allows us to detect TATP with a reasonable detection limit.

8.4 QCL with 1220 to 1330 cm^{-1} Tuning Range

The second QCL used in this work is a pulsed QCL with a tuning range from 1220 to 1320 cm^{-1} and an output power ranging from 50 to 90 mW,

depending on the wavelength selected. This QCL can probe the two smaller TATP peaks at 1240 and 1270 cm^{-1} and the major peak at 1195 cm^{-1}. This QCL yields a lower output power as compared to the first QCL, and hence, it is more challenging to collect a wave-mixing spectrum. **FIGURE 8.3** shows the QCL wave-mixing spectrum collected at full power and the major spectral features are similar to those of the FT-IR spectrum. As with the previous QCL, the 5 cm^{-1} scan interval used for this QCL does not yield high spectral resolution in order to accurately capture some of the minor spectral features.

FIGURE 8.4 shows cubic dependence on laser power for the wave-mixing signal at 1270 cm^{-1}. This is a much weaker peak as compared to the strong 1196 cm^{-1} peak. In addition, the output power of this QCL is relatively low and the power stability is low. Hence, the experimental slope is not as close to the expected slope of 3.0.

8.5 QCL with 1153 to 1223 cm^{-1} Tuning Range

This third QCL is a pulsed QCL with a tuning range from 1153 to 1223 cm^{-1}. This QCL also has an updated controller that allows the user to scan wavelengths automatically using two different scanning modes. The first mode is a fast-sweep scan that takes the laser through its full tuning range in less than 10 s. The second mode is a step scan that allows the user to set the parameters of the scan. Both modes allow the user to collect the entire spectrum much more quickly as compared to the previous QCLs where the user manually tunes the laser for each scan interval.

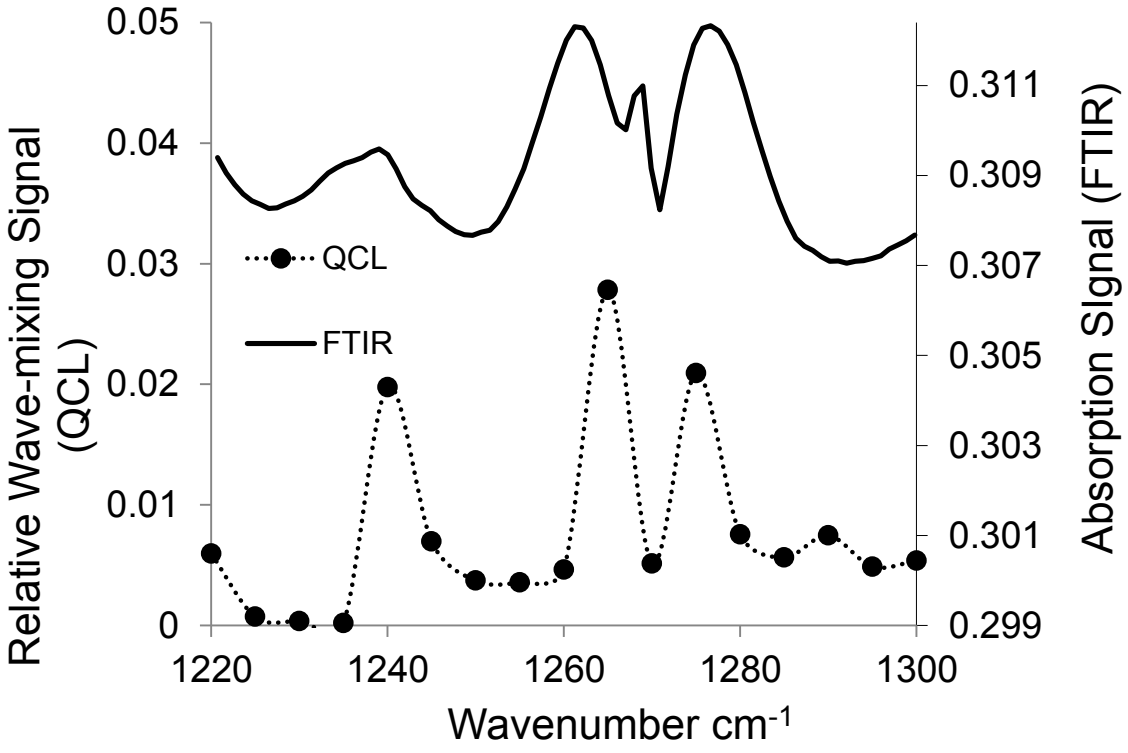

FIGURE 8.3 Wave-mixing spectrum of TATP in the 1220 to 1330 cm^{-1} range with a 5 cm^{-1} scan interval. It shows some characteristics that are in common with those from a FT-IR scan.

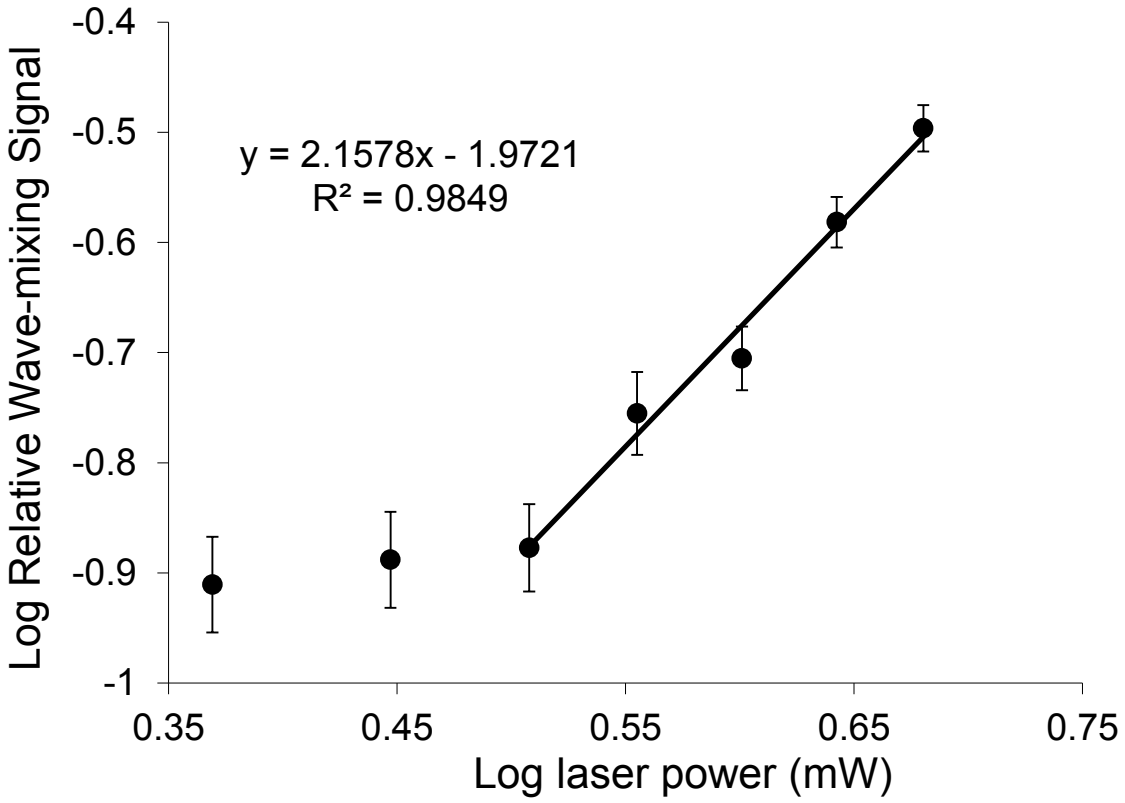

FIGURE 8.4 Cubic dependence on laser power for wave-mixing signal at 1270 cm^{-1}. This is a weak absorption peak as compared to the main peak at 1195 cm^{-1}. Thus, the slope is not as close to the expected slope of 3.0.

The fast-sweep mode is a continuous process in which the laser controller moves the grating at a set speed through the full tuning range of the QCL. Since it is a fast process, the lock-in amplifier time constant is set to 10 ms or faster and the AIDA data acquisition program is set to 20 samples/s or higher. Based on the start and stop times and the overall scan time needed, the wavelength of each data point can be determined. **FIGURE 8.5** shows the result of 10 consecutive fast scans and the error bars associated with each wavelength point of the spectrum. It is apparent that there is a great deal of variability at each wavelength point of the scan. Some of this variability is inherent in the communication between the lock-in amplifier and the digital-to-analog converter since the number of data points collected per sweep is not the same for all the fast-sweep scans.

FIGURE 8.6 shows the TATP wave-mixing spectrum collected in the fast sweep mode and it is compared to the FT-IR spectrum. The wave-mixing spectrum is normalized to compensate for the differences in the laser power at different wavelengths. **FIGURE 8.7** shows the same TATP wave-mixing spectrum after using a 5-point moving average.

The step-scan method for tuning the QCL wavelength range does not have the problems associated with the fast-sweep method. However, it is a slower data collection process since the grating is moved systematically to select the wavelengths across the entire tuning range. The user can position the grating and then tune to another grating position and stay there for the user defined time interval. For this relatively slow process, the lock-in amplifier is set

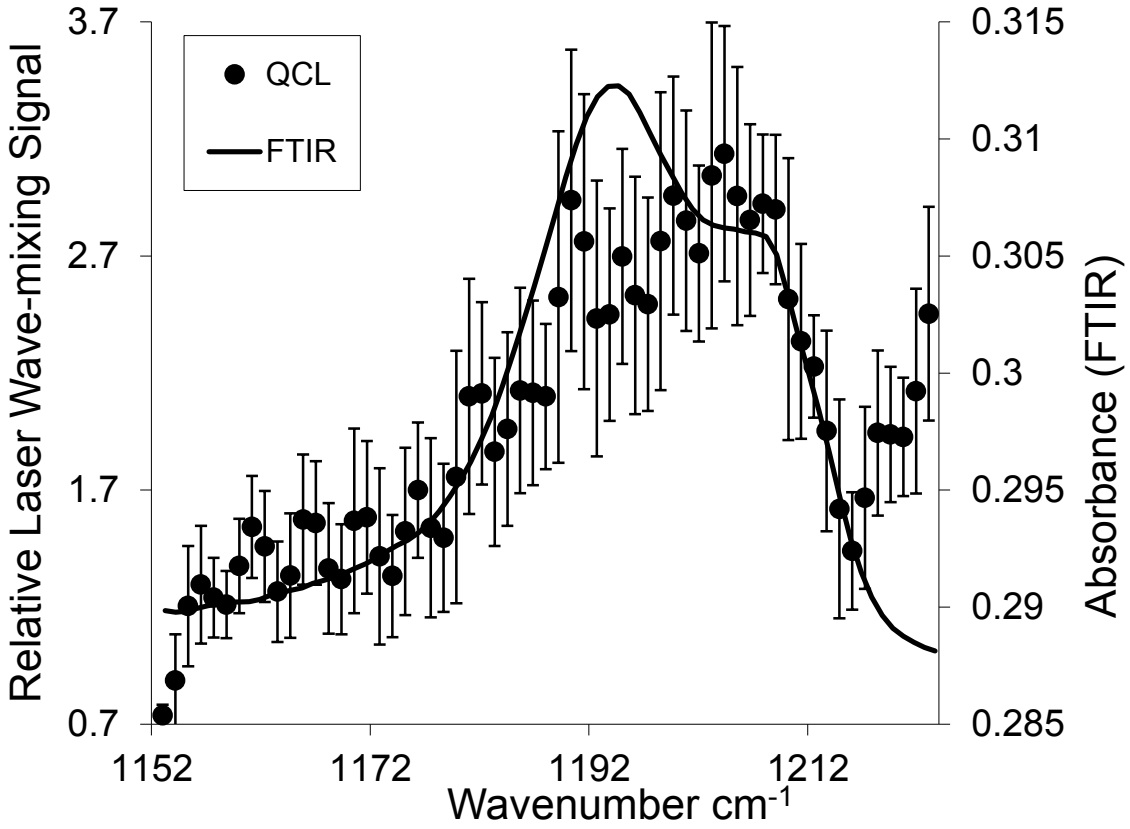

FIGURE 8.5 Wave-mixing spectrum of TATP vapor collected by using the fast-sweep mode of the QCL. The wave-mixing spectrum has the same general characteristics of the FT-IR spectrum, however, the fast-sweep mode does not yield good S/N, and hence, it is not used as much as the other scanning modes available. The spectrum is normalized to compensate for the differences in the laser power at different wavelengths.

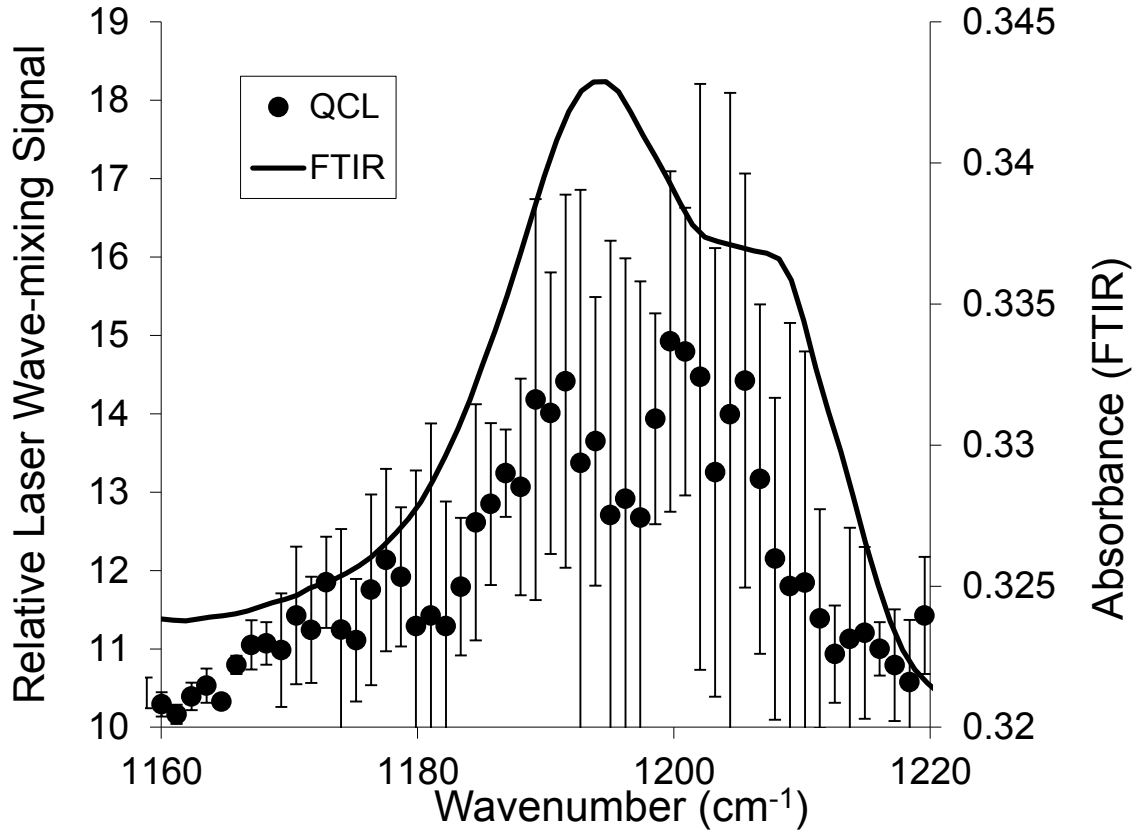

FIGURE 8.6 Wave-mixing spectrum collected by using the fast-sweep mode of the QCL and compared to the FT-IR spectrum. The spectrum is normalized to compensate for the differences in the laser power at different wavelengths.

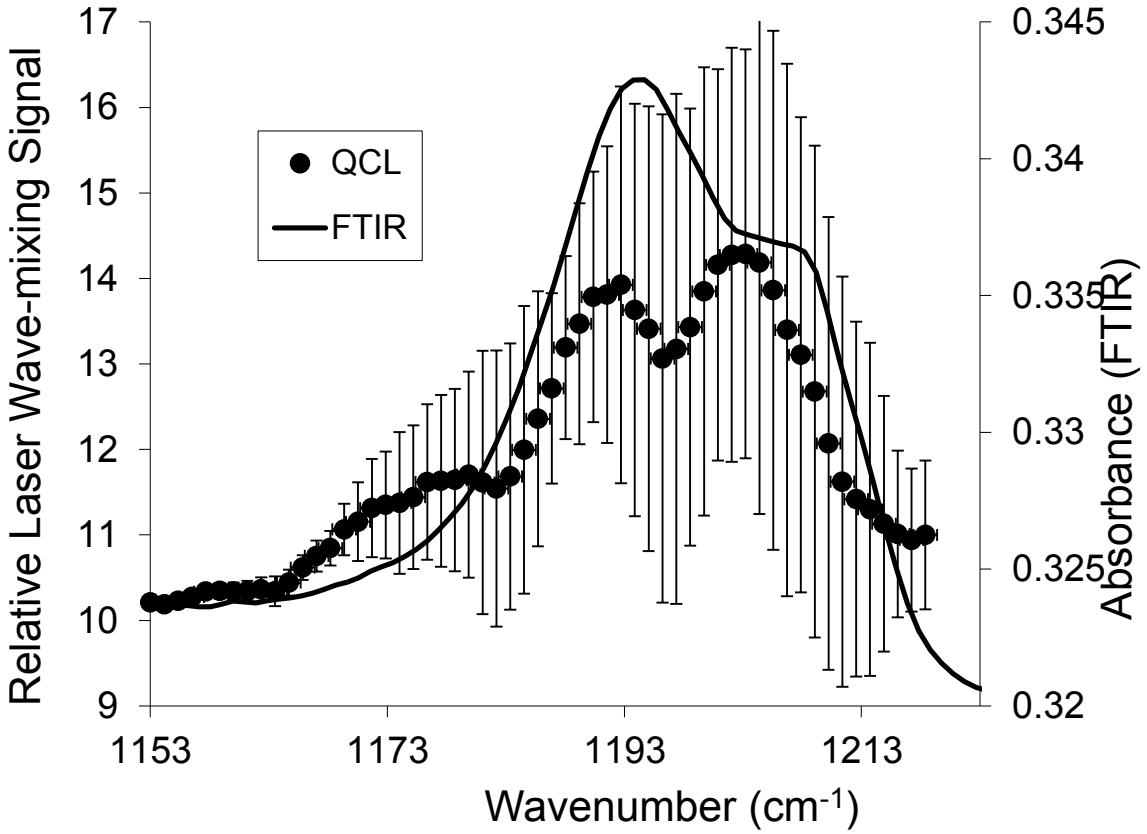

FIGURE 8.7 Wave-mixing TATP spectrum (5-point moving averaged) compared to the FT-IR spectrum.

to a time constant of 100 ms and the data collection rate is set to 10 samples/s. A single scan with 50 wavelength steps could take 200 s if one takes 4 s to signal average at every wavelength step. Although this may take longer to collect a spectrum as compared to the fast-sweep mode, the S/N is much better and the wavelength accuracy is much higher.

To confirm the TATP wave-mixing signal, cubic dependence on laser power is tested using an on-resonant wavelength and an off-resonant wavelength. **FIGURE 8.8** shows cubic dependence (slope of 2.8) on power for the wave-mixing signal monitored "on resonant" at the 1185 cm^{-1} peak. **FIGURE 8.9** does not show cubic dependence on laser power (slope of 1.1), as expected, when monitored "off-resonant" at 1153 cm^{-1} away from a peak.

8.6 Continuous-Wave QCL with 1155 to 1255 cm^{-1} Tuning Range

The final QCL used in this work is a continuous-wave mode-hop-free QCL with a tuning range from 1155 to 1255 cm^{-1}. This QCL also has an updated controller that allows the user to scan wavelengths automatically. The previous QCLs used are pulsed lasers and the peak powers are high, but the average powers are much lower, usually less than 15 mW. The low average power level results from a low rep rate (5% duty cycle) set by the manufacturer. The new continuous-wave QCL, on the other hand, can yield a power output of up to 80 mW, depending on the current and the wavelength selected.

This new CW QCL can operate in either pulsed, CW or CW-mode-hop-free modes. The CW mode has the broadest tuning range (1155 to 1255 cm^{-1}).

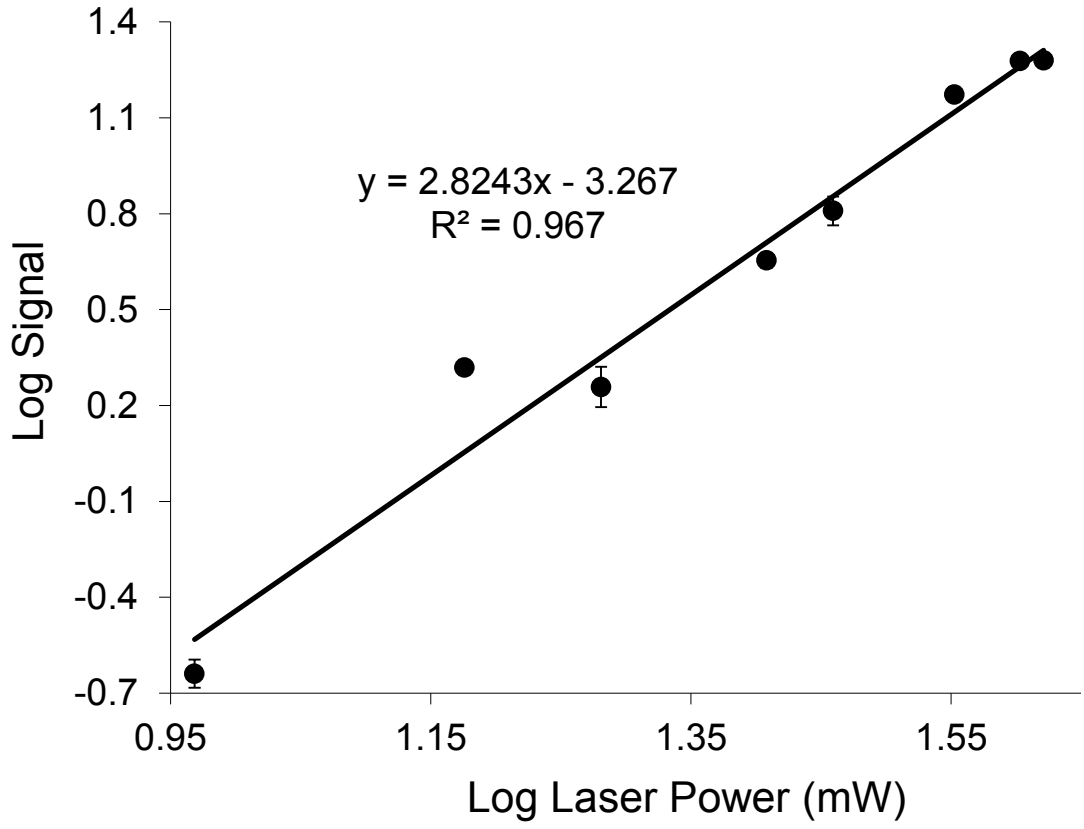

FIGURE 8.8 Cubic dependence on laser power for the wave-mixing signal at 1185 cm^{-1}.

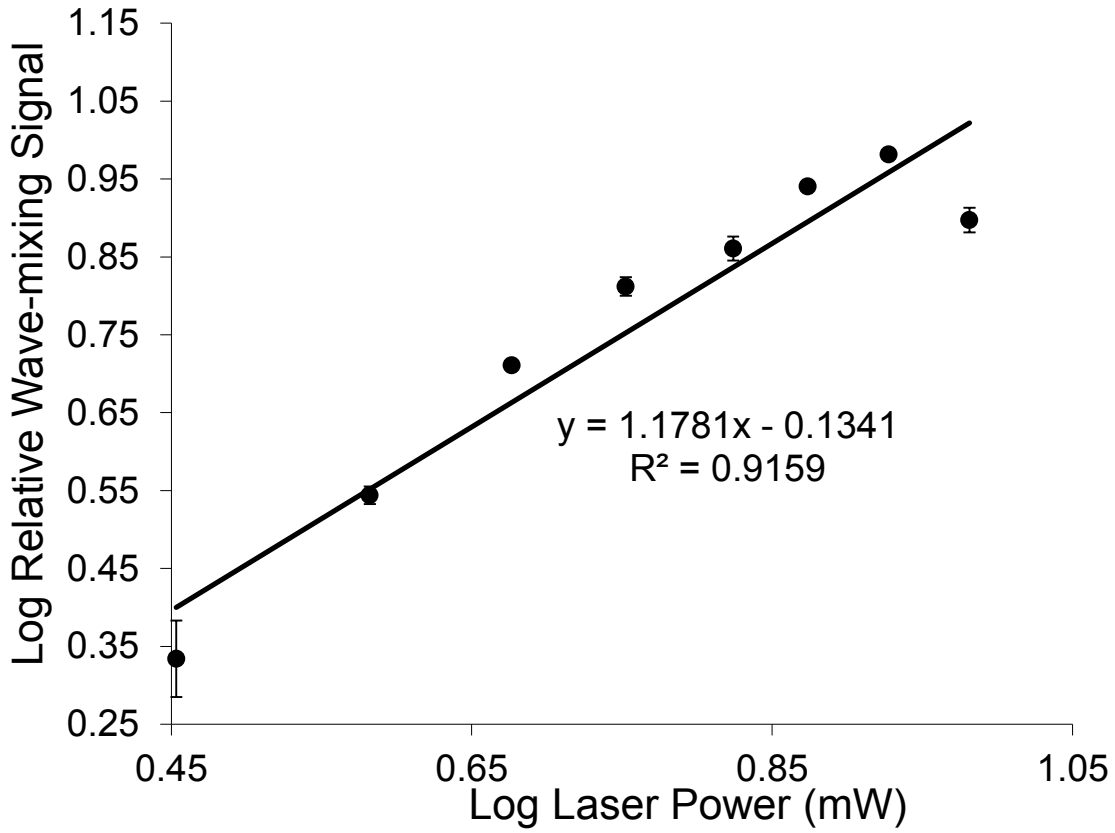

FIGURE 8.9 Power dependence plot at an off-resonant wavelength. As expected, a slope close to 1 is observed when the nonlinear wave-mixing signal is not present.

The CW-mode-hop-free mode has a narrower tuning range (1195 to 1235 cm^{-1}). The pulsed mode and the mode-hop free mode are not used in this work. The CW mode is selected for this work since a broad tuning range is needed to cover the main peak and the smaller peaks. The step-scan tuning mode is set to move in 1 or 2 cm^{-1} scan interval, which is much larger than the wavelength shift expected in a mode hop. The mode-hop free functionality of this QCL will be used in future studies that require much high spectral resolution to resolve isotopes.

In laser wave-mixing spectroscopy, a number of factors and parameters can affect the signal strength including the solvent used in liquid-phase samples, the angle between the two input beams, the analyte path length, the analyte flow rate, and the amplitude modulation frequency. Each of these parameters is tested and optimized in order to optimize the signal and the S/N.

TATP is soluble in a number of different solvents. Methylene chloride, acetonitrile, methanol, ethanol, 1, 4-Dioanxe, toluene and carbon disulfide are tested as potential solvents for TATP using FT-IR. Analyzing the solvents as neat solutions more closely approximates their usage in this work since the analyte, i.e., TATP, is usually at trace-concentration levels in these solvents. Ethanol, methanol, dioxane and methylene chloride all have strong absorption lines in the tuning range of the CW QCL and they could completely auto-absorb the signal beams and even the input beams. With these solvents, the input beams are not present post sample. Thus, ethanol, methanol, dioxane and

methylene chloride are not used as solvents. Toluene also has a number of large peaks in the wavelength tuning range of the CW QCL.

As shown in **FIGURE 8.10,** carbon disulfide shows virtually no FT-IR absorption in the QCL tuning range, and acetonitrile shows a moderate amount of signal and it shares the same characteristics as the laser power plot (**FIGURE 8.10C)**. Neither trace follows the power profile of the QCL output, and hence, carbon disulfide is selected as an appropriate solvent for TATP.

The angle between the two input beams is also optimized to generate the best S/N. Generally, the smaller the beam angle, the sharper the dynamic gratings, and the stronger the wave-mixing signal is observed. A simple test is performed to determine the optimum angle. By keeping one input beam stationary and by moving the other beam, one can adjust the angle conveniently. As the beams move closer to each other, the crossing angle gets smaller. Using an analyte with 250 ug/mL TATP in carbon disulfide, an optimum angle of 0.96° is determined for the CW QCL.

The cell design and the cell path length are also optimized to yield the best S/N. The demountable FI-TR cell used in this work (Crystal Labs, SL-2) has a variety of Teflon inserts to be sandwiched between the windows so that the path length can be changed. An unnecessarily long path length could cause auto-absorption of the signal beam by the analyte itself. In our UV and visible laser-based wave-mixing setups, capillaries with internal diameters from 20 to 250 um are used as sample holders. However, there are no capillary cells that

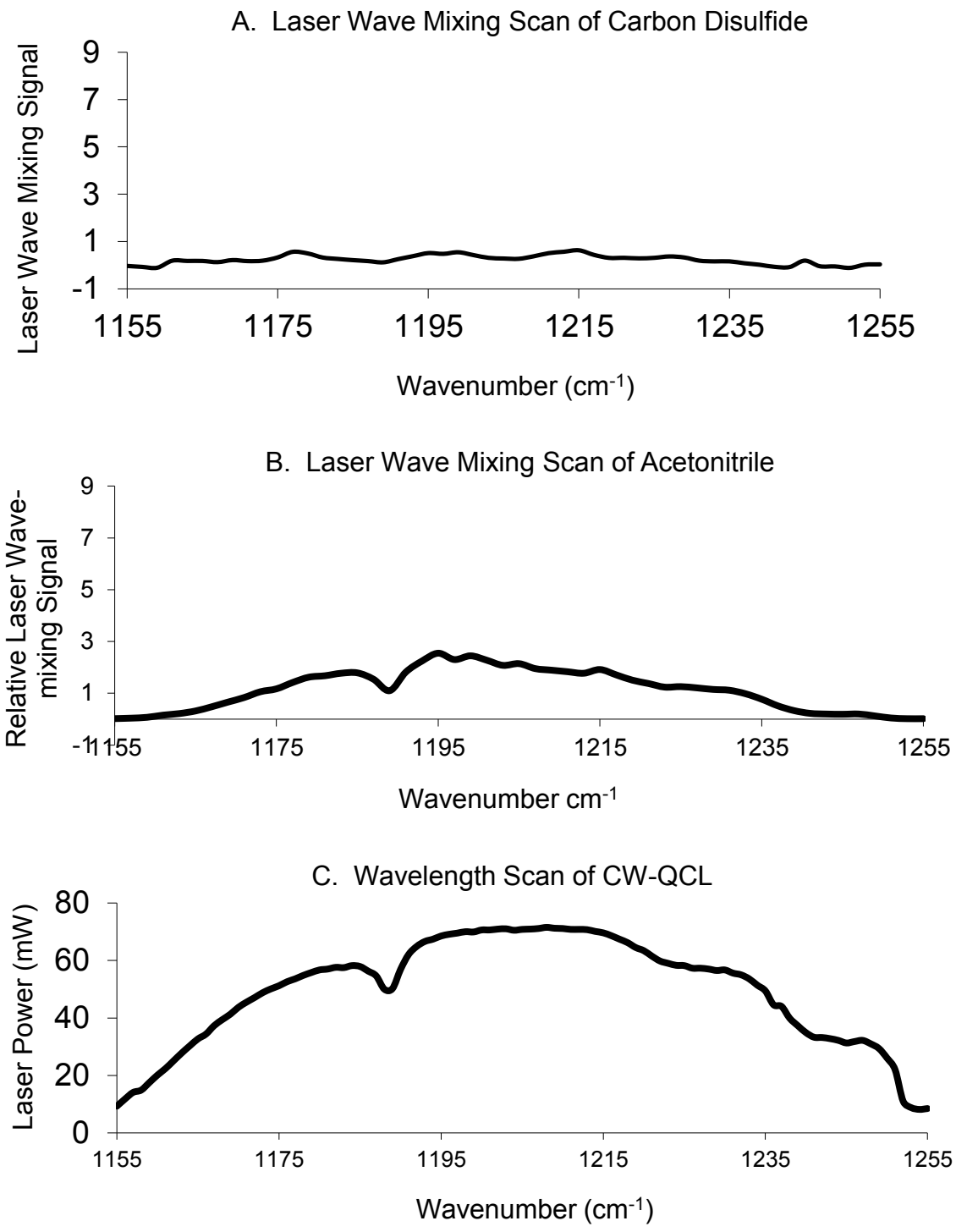

FIGURE 8.10 A, B and C Carbon disulfide (Figure 8.10A) has been shown to exhibit a small laser wave-mixing signal without optical absorption in the mid-IR range. Acetonitrile (Figure 8.10B) has a very small absorbance in this wavelength region. Figure 8.10C shows a plot of laser power levels at different QCL laser wavelengths.

are suitable for mid-IR wavelengths. Using the demountable IR cell, we determine that a path length of 1.7 mm yields the best S/N for this setup.

In UV and visible laser-based wave-mixing setups, an amplitude modulation frequency of 400 Hz is suitable for liquid-phase analytes. As shown in **FIGURE 8.11,** the optimum frequency is determined to be 4 kHz for the CW QCL mid-IR wave-mixing setup. This is entirely because the mid-IR photodetector is designed to detect fast rep-rate signals from a pulsed laser and the detector performs ideally above 5 kHz. For gas-phase TATP detection, the liquid IR cell is replaced with a 10-cm re-sealable gas cell with three inlets/outlets. The path length of the TATP vapor is extended out to 10 cm, i.e., the length of the gas cell.

FIGURE 8.12 shows a QCL wave-mixing spectrum for 50 µg/mL liquid-phase TATP dissolved in carbon disulfide. The laser wave-mixing spectrum matches well with the FT-IR spectrum. **FIGURE 8.13** shows comparison of QCL wave-mixing spectra at different concentration levels. The two dominate peaks at 1185 and 1203 cm^{-1} are seen at each concentration level and they match those in the FT-IR spectrum (top trace). As expected, some concentration saturation is observed for the wave-mixing spectrum at the highest concentration level tested (500 ug/mL).

FIGURE 8.14 shows detection sensitivity of CW QCL wave-mixing detection of 250 ng/mL liquid-phase TATP dissolved in carbon disulfide with a S/N of 26.5, compared to the blank signal of carbon disulfide. A preliminary

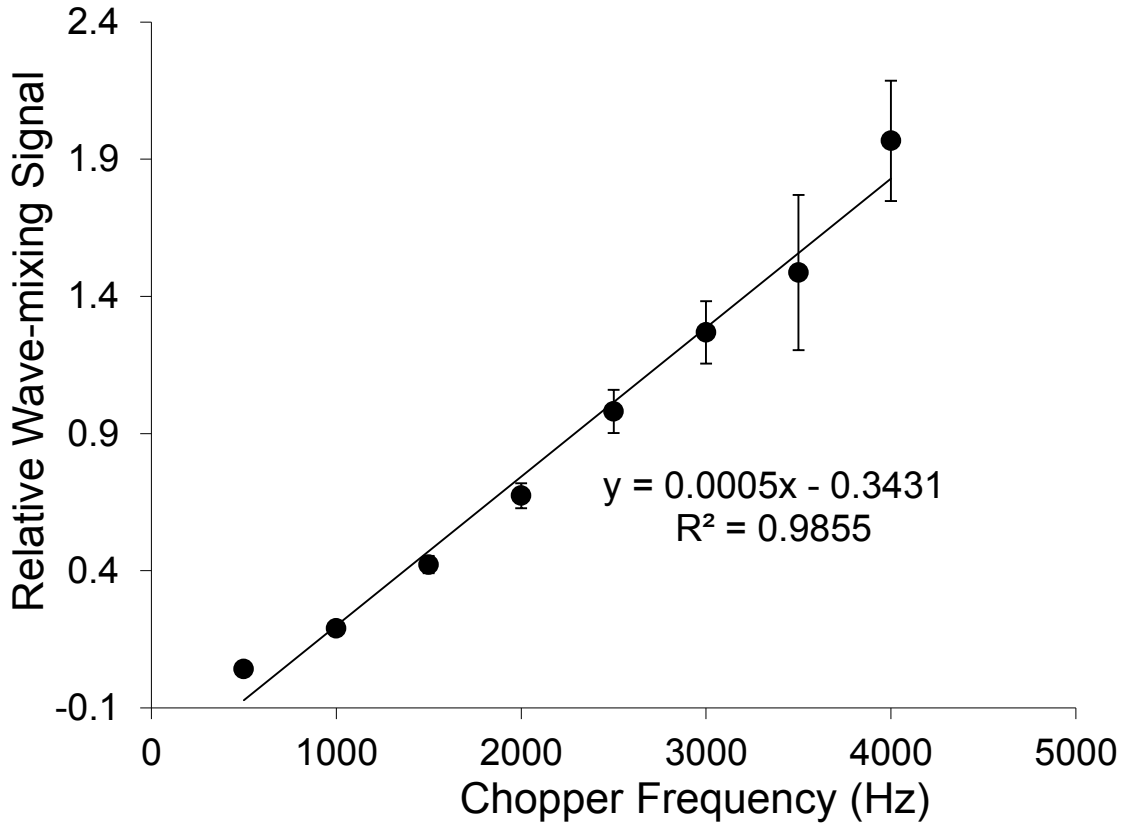

Figure 8.11 Wave-mixing signal at different optical chopper modulation frequencies. The optimal modulation frequency is determined to be 4000 Hz for the sample and the detector used.

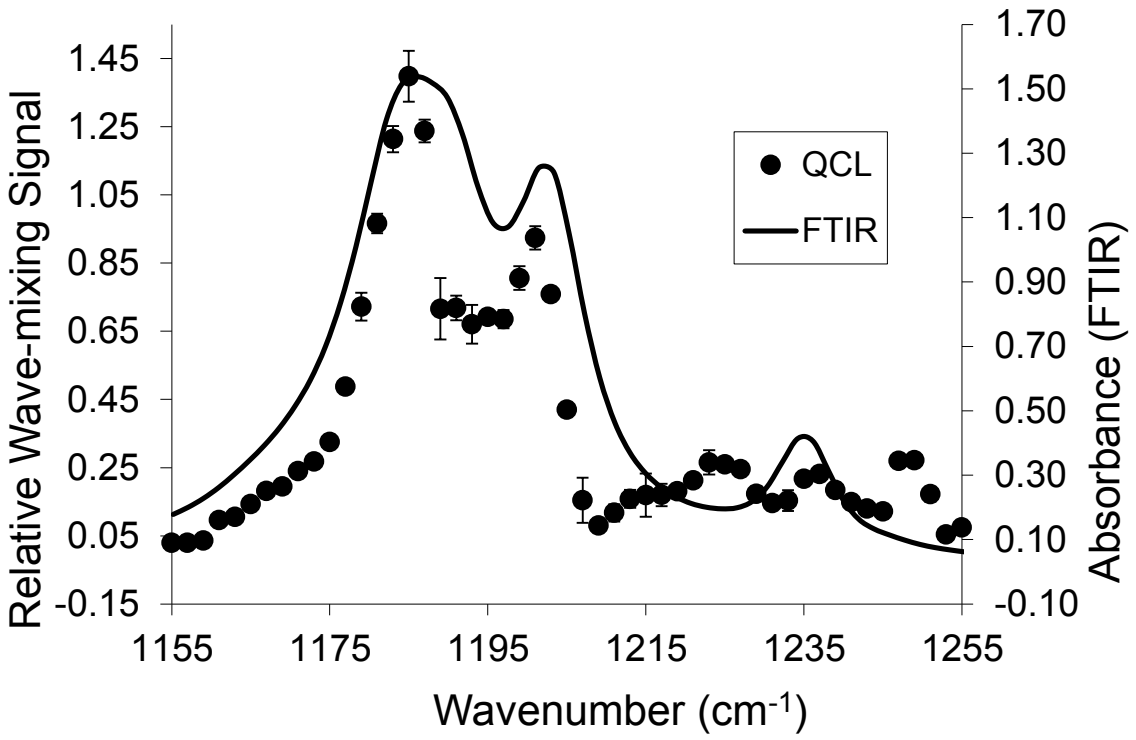

FIGURE 8.12 Wave-mixing spectrum of 50 ug/mL TATP dissolved in carbon disulfide compared to the FT-IR spectrum.

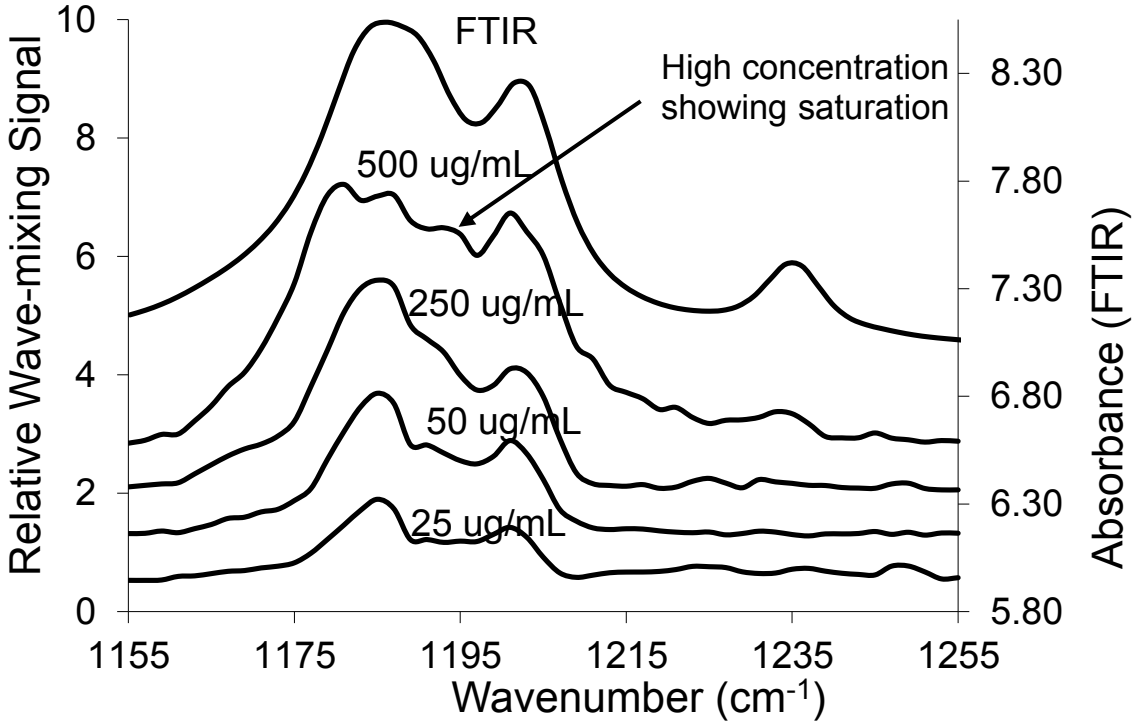

FIGURE 8.13 Wave-mixing spectra of TATP dissolved in carbon disulfide retain their unique spectral characteristics across a range of concentration levels.

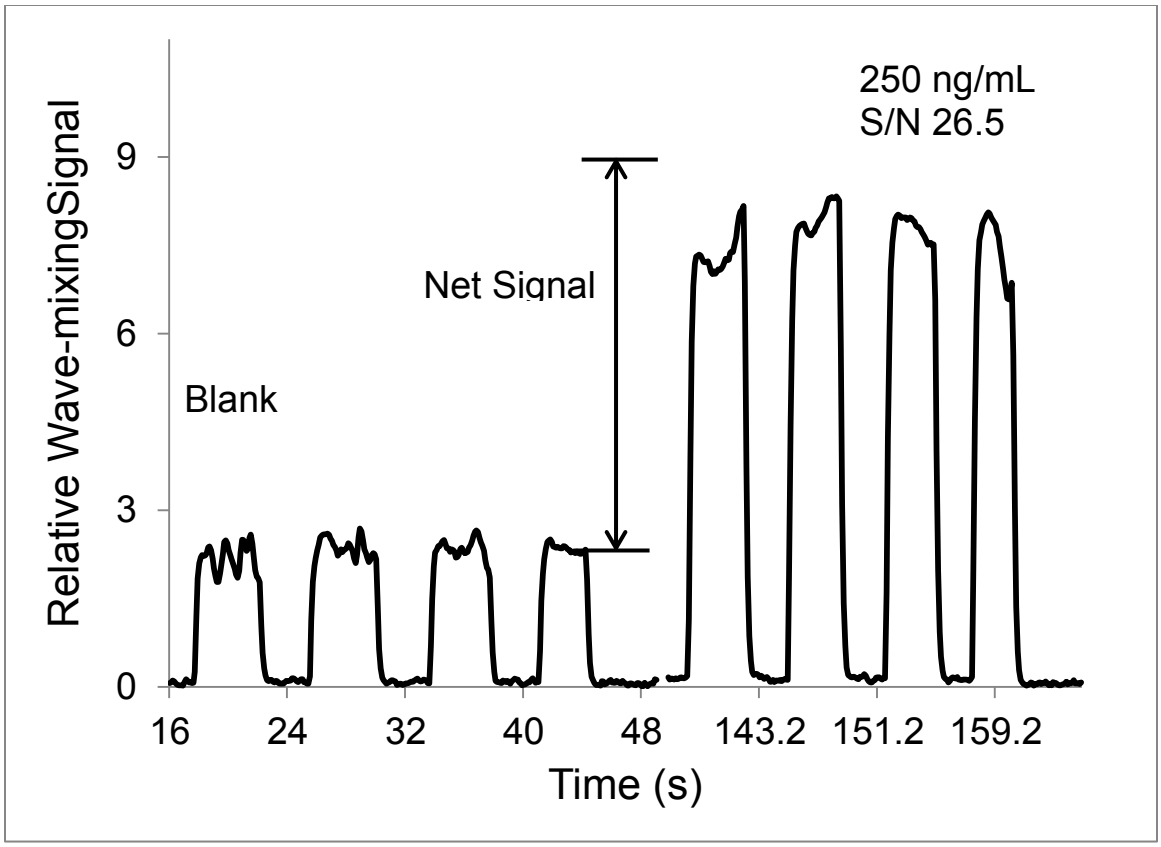

FIGURE 8.14 Wave-mixing detection sensitivity for TATP dissolved in carbon disulfide.

concentration detection limit of 69 ng/mL, 69 ppb, 31 nM is determined for liquid-phase TATP.

FIGURE 8.15 shows cubic dependence on power (slope 2.6) for the QCL wave-mixing signal of 50 ug/mL liquid-phase TATP in carbon disulfide. It is apparent that the signal is power saturated at the highest levels of the laser power tested.

In the gas phase, TATP is harder to detect. The photodetector mismatch and the low vapor pressure of TATP work against generating and detecting laser wave-mixing signals as strong as that seen for the liquid-phase TATP. **FIGURE 8.16** shows our CW QCL wave-mixing spectrum of gas-phase TATP with the major peak at 1195 cm^{-1} and the minor peak at 1235 cm^{-1}. As expected for the gas-phase analytes, the laser wave-mixing spectrum shows more features as compared to the FT-IR spectrum.

FIGURE 8.17 shows cubic dependence on power for the wave-mixing signal of gas-phase TATP. The slope (2.6) is not close to the expected slope of 3.0, partly due to the low sensitivity of the frequency-mismatched photodetector, the low population of TATP molecules in the gas phase at room temperature, and the residual background noise levels. **FIGURE 8.18** shows detection sensitivity of QCL laser wave mixing for the gas-phase TATP analyte. Based on the net signal observed between the total TATP signal (cell and TATP) and the blank signal (cell only), a preliminary concentration detection limit of 149 ppb is determined for the TATP vapor at room temperature.

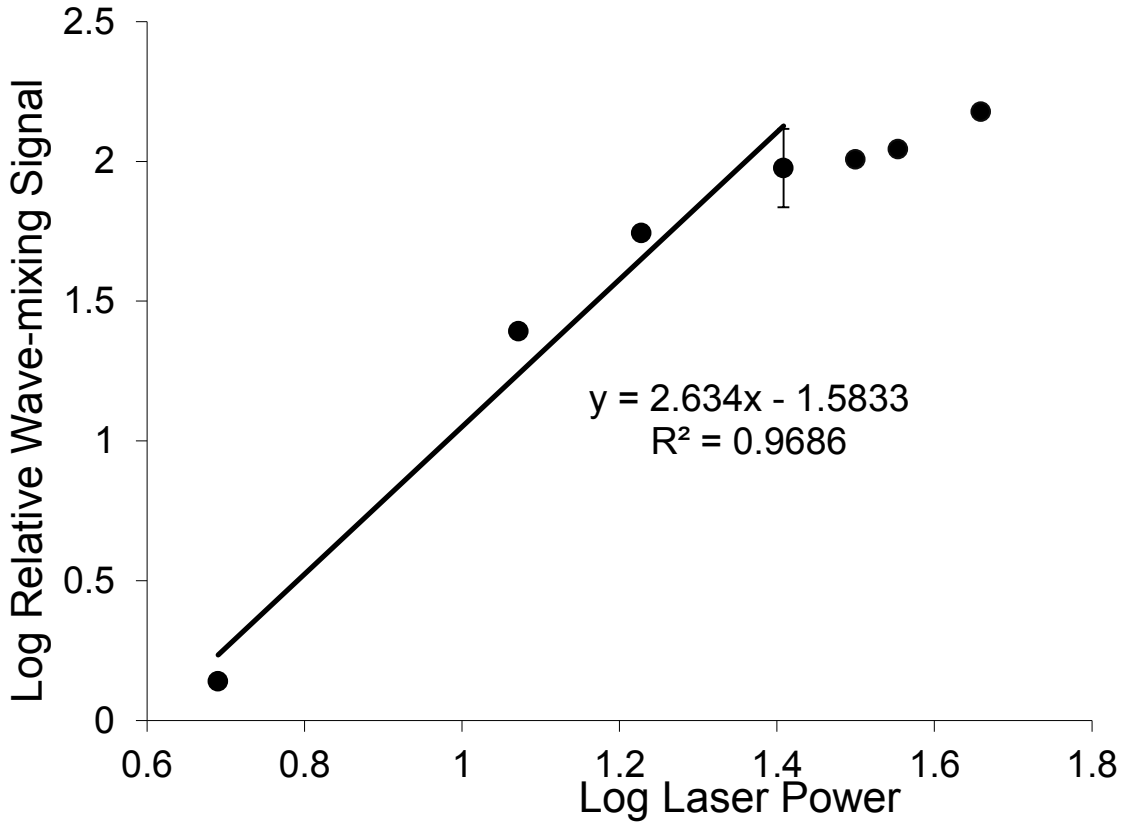

FIGURE 8.15 Cubic dependence on laser power for the wave-mixing signal of 50 ug/mL TATP in CS_2. At higher laser power levels, power dependence deviates from the expected cubic relationship due to power saturation.

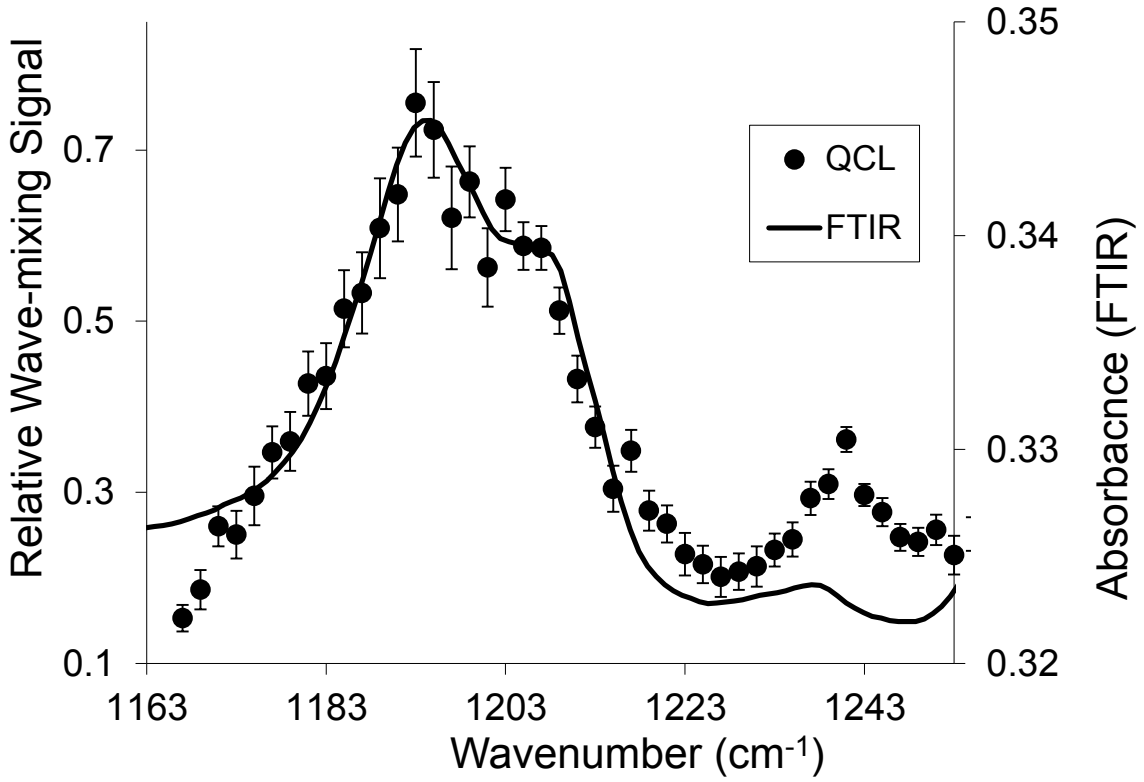

FIGURE 8.16 Comparison of wave-mixing spectrum and FT-IR spectrum for TATP vapor. The major peak at 1195 cm^{-1} and the minor peak at 1235 cm^{-1} are present.

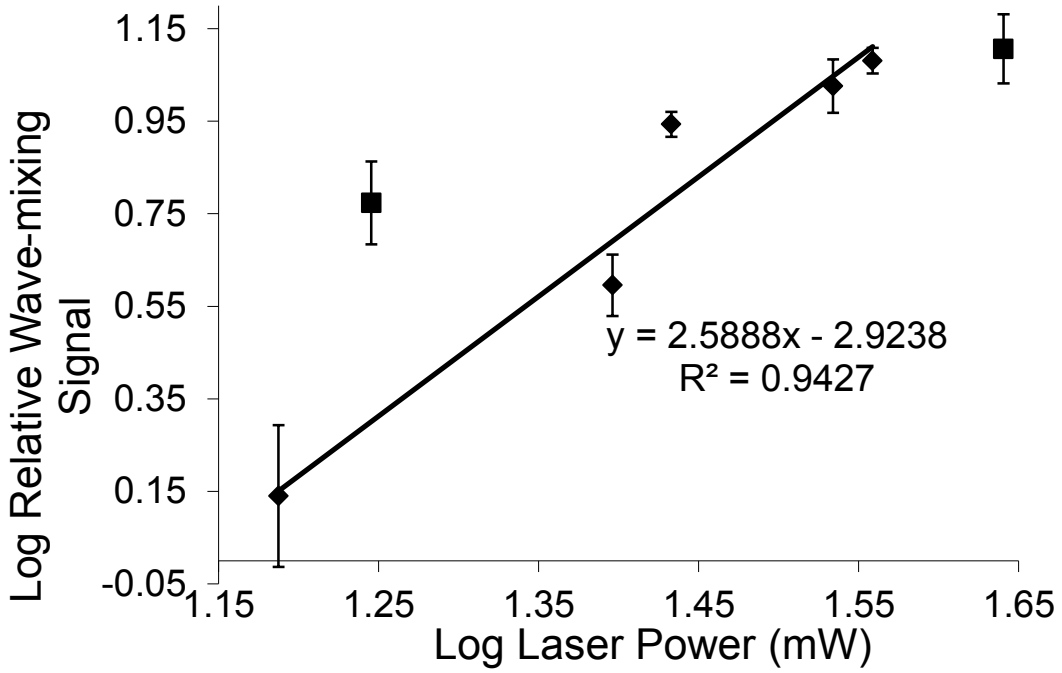

FIGURE 8.17 Cubic dependence on laser power for the wave-mixing signal of TATP vapor.

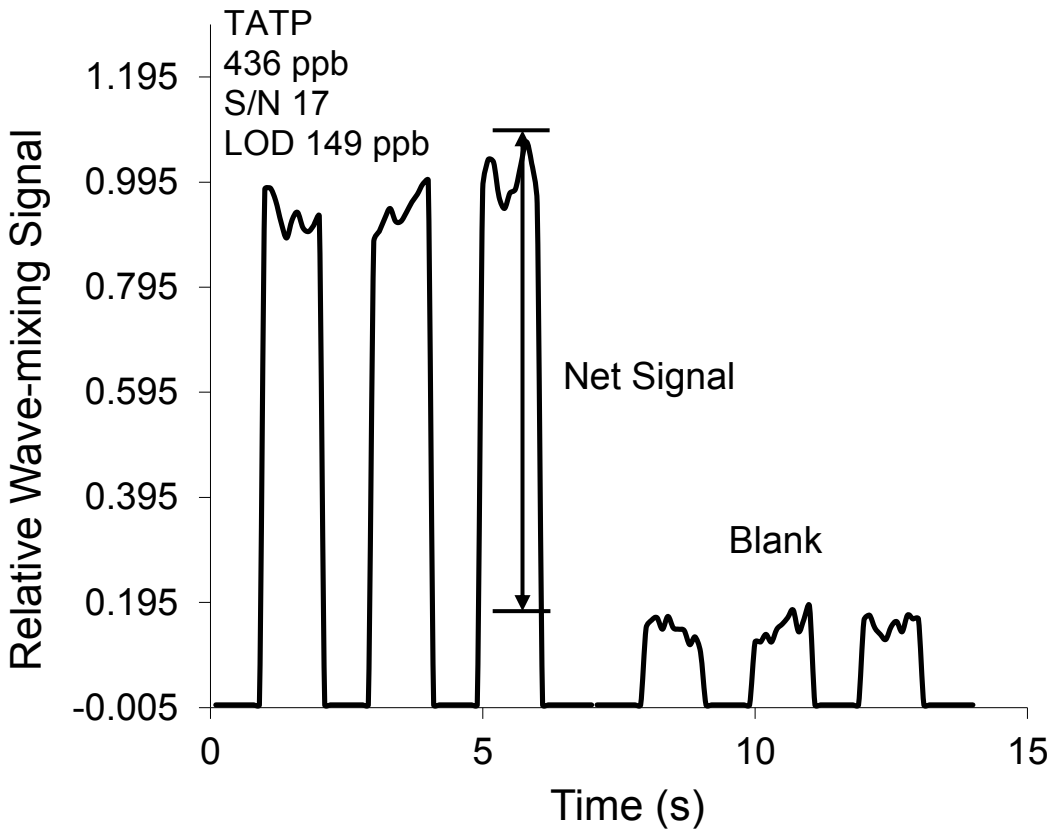

FIGURE 8.18 Wave-mixing detection sensitivity for TATP vapor.

8.7 Conclusions

Quantum cascade laser-based mid-IR wave-mixing detection is presented as a sensitive method for the detection of explosive triacetone triperoxide in both liquid- and gas-phase analytes at room temperature. The quantum cascade laser offers many advantages including portability, tunability, high spectral resolution, and power efficiency. Five different quantum cascade lasers are tested and used to probe the C-O-O stretch at 1195 cm^{-1} and the wave-mixing spectra are matched to the corresponding FT-IR spectra. Laser wave mixing is competitive with other methods available for TATP analysis. A preliminary concentration detection limit of 69 ppb is determined for liquid-phase TATP, 77 ppb for gas-phase TATP with a pulsed QCL, and 149 ppb for gas-phase TATP with a CW QCL. As shown in **Tables 8.2A and B,** our wave-mixing detection sensitivity levels are comparable or better than those of other sensitive detection methods. Laser wave mixing offers additional advantages including ease of use, portability, size, ruggedness, minimal sample preparation, and standoff detection capability.

TABLE 8.2A Comparison of sensitive detection methods for liquid-phase TATP.

TATP Detection	λ	Limit of Detection	Reference
UV-visible absorption	415 nm	1.78 ppm 8 x10^{-6} M (1.78 ppm)	Analyst, **2002**, 127, 1152 – 1154
Fluorescence spectroscopy	Ex at 324 nm Em at 405 nm	0.444 ppm 2 x 10^{-6} M (0.444 ppm)	Analytical Chemistry, **2003**, 75, 4, 731-735
Metal ion complexation	N/A	N/A	J. Phys. Chem. A **2002**, 106, 4951-4956
Self-immolative dendritic probe	Ex at 279 nm Em at 560 nm	N/A	Chem. Commun., **2008**, 5701–5703
Reaction with borate prochelator	Ex at 270, 350 nm Em at 380, 400 nm	2.22 ppb 10 nM (2.22 ppb)	Inorganic Chemistry, 47, 21, **2008,** 9748-9750
Double step chronoamperometry		8.51 uM 1.9 ppm	Microchemical Journal, **2010**, 94, 166-170
Laser wave mixing (liquid phase)	1195 cm^{-1}	69 ppb 31 nM	This work

TABLE 8.2B Comparison of sensitive detection methods for gas-phase TATP.

TATP Detection	λ	Limit of Detection	Reference
Cavity Ring Down Spectroscopy	7 - 8 um	1.2 ppb	Journal Applied Physics B: Lasers and Optics, **2002** Vol. 75, pg. 367-376
FTIR	1156 - 1243 cm^{-1}	222 ppm	Analytical Chemistry, **2006**, Vol. 78, Issue 23, pg. 8150 -8155
Quantum Cascade Laser Photo Acoustic Spectroscopy	7.15 - 7.5 um	18 ppb	Applied Optics, **2007**, Vol. 46, Issue 25, pg. 6397-6404
Organic Semi-conductor GaAs sensors		100 ppb	Sensors and Actuators B, **2009**, Vol 140, pg 122-127
Stand-off Raman Spectroscopy	514.5 nm	10 ug/cm^2 @ 7 meters	Anal Bioanal Chem, **2009**, Vol 395, pg 323-335
Colorimetric Sensor Array		2 ppb	JACS, **2010**, vol 132, pg 15519-15521
Quartz Micro Balances		1 ppm	Sensors and Actuators B, **2010**, Vol 143, pg 561-566
DFWM (gas phase)	1195 cm^{-1}	Pulsed QCL 77 ppb CW QCL 149 ppb	This work, derived from Clayperon Equation

REFERENCES

1. Schulte-Ladbeck, R; Edelmann, A; Quintas, G; Lendl, B; Karst, U*: Analytical Chemistry.* **2006**, *78,* 8150 – 8155.

2. Oxley, JC; Smith, JL; Shindem K; Moran, J: *Propellants, Explosives, Pyrotechnics,* **2005**, *30(2),* 127- 130.

3. Dunayevskiy, I; Tsekoun, A; Prasanna, M; Go, R; Patel, KN: *Appl, Opt.* **2007**, *46*(25), 6397- 6404.

4. Schulte-Ladbeck, R; Kolla, P; Karst, U: *Analyst,* **2002**, *127,* 1152 – 1154.

5. Schulte-Ladbeck, R; Kolla, P; Karst, U: *Analytical Chemistry,* **2003**, *75(4)*, 731 – 735.

6. Dubnikova, F; Kosloff, R; Zeiro, Y; Karpas, *Z*: *Journal of Physical Chemistry A*, **2002**, *106*, 4951 – 4956.

7. Sella, E; Shabat, D: *Chemical Communications*, **2008**, *vol*, 5701 – 5703.

8. Germain, ME; Knapp, MJ: *Inorganic Chemistry*, **2008**, *47(21)*, 9748 – 9750.

9. Xie, Y; Cheng, FI: *Microchemical Journal*, **2010**, *94*, 166 – 170.

10. Todd, MW: Provencal, RA; Owano, TG; Paldus, BA; Kachanov, A: *Journal of Applied Physics B: Lasers and Optics.* **2002**, *(75),* 367 – 376.

11. Capua, E; Cao, R; Sukenik, CN; Naaman, R: *Sensors and Actuators B,* **2009**, *140*, 122 – 127.

12. Pacheco-Londono, LC; Ortiz-Rivera, W; Primera-Pedrozo, O; Hernandez-Rivera, SP: *Analytical and Bioanalytical Chemistry*, **2009**, *395,* 323 – 395.

13. Hengwei, L; Suslick, KS: *Journal of the American Chemical Society*, **2010**, *132*, 15519 – 15521.

14. Lubczyk, D; Siering, C; Lorgen, J; Shifrina, ZB; Mullen, K; Waldvogel, SR: *Sensors and Actuators B,* **2010**, *143*, 561 – 566.

Appendix A: Calculation of probe volumes and mass detection limits

Calculating the mass detection limit in a DFWM setup requires the determination of the laser probe volume. This calculation is a multi-step process that begins with the measurement of the beam diameters and the center-to-center distance of the two input beams. To measure the beam diameters, an iris is used to cut the power to 90%. The 90% beam diameter is measured using a caliper. The center-to-center distance is determined by tracing the two beam spots and using the caliper for measurement.

The beam waist of the focused beam at the sample cell is calculated using the beam waist equation below:

$$4\,(\lambda * f')/\,(\pi D)$$

where λ is the wavelength of the laser, f' is the focal length of the mixing lens, and D is the diameter of the 90% beam.

The next value to calculate is the beam angle. This can be done using one-half of the center-to-center distance and the tangent formula. Appendix Figure 1 shows the triangle that is formed by the input beams. The geometric formula TAN a = opposite/adjacent is used to solve for the angle a. The total angle between the two beams is then calculated using $\theta = 2a$. This beam angle θ should be less than 2° to get optimal DFWM signal.

Once the beam angle is calculated, the probe volume can be calculated. The DFWM probe is formed by the overlap of two circular beams. The shape of

the probe volume can be considered to be two cones, stacked base to base. Using this, the geometric equation for the volume of a cone can be used to calculate a probe volume. The equation for a cone is shown below:

$$V_{cone} = 1/3\pi r^2 h$$

where r^2 is the radius of the beam waist and h is the height of the cone. The height of the cone can be determined in a manner similar to the beam-angle calculation using right triangle relationships. In this case, the length of the opposite leg of the right triangle is equal to ½ the beam waist. The angle is a, and the adjacent leg of the right triangle can be calculated using the formula h = beam waist/TAN a. Once h is known, it can be plugged into the cone volume formula. From here, the probe volume is calculated using

probe volume = two*V_{cone}.

The mass detection limit is defined as the amount of material detected within the probe volume. The concentration detection limit is first calculated using the following formula:

$$\text{Sample conc. *sq rt } ((S/n_{lod})/(S/n_{exp}))$$

The number of moles in the probe volume is calculated using the equation:

Moles = LOD in M/probe volume in L

The mass in the probe volume is calculated using the equation:

Mass = moles * MW in g/mole

The number of molecules in the probe volume is calculated using the equation:

Molecules = moles * Avogadro's number

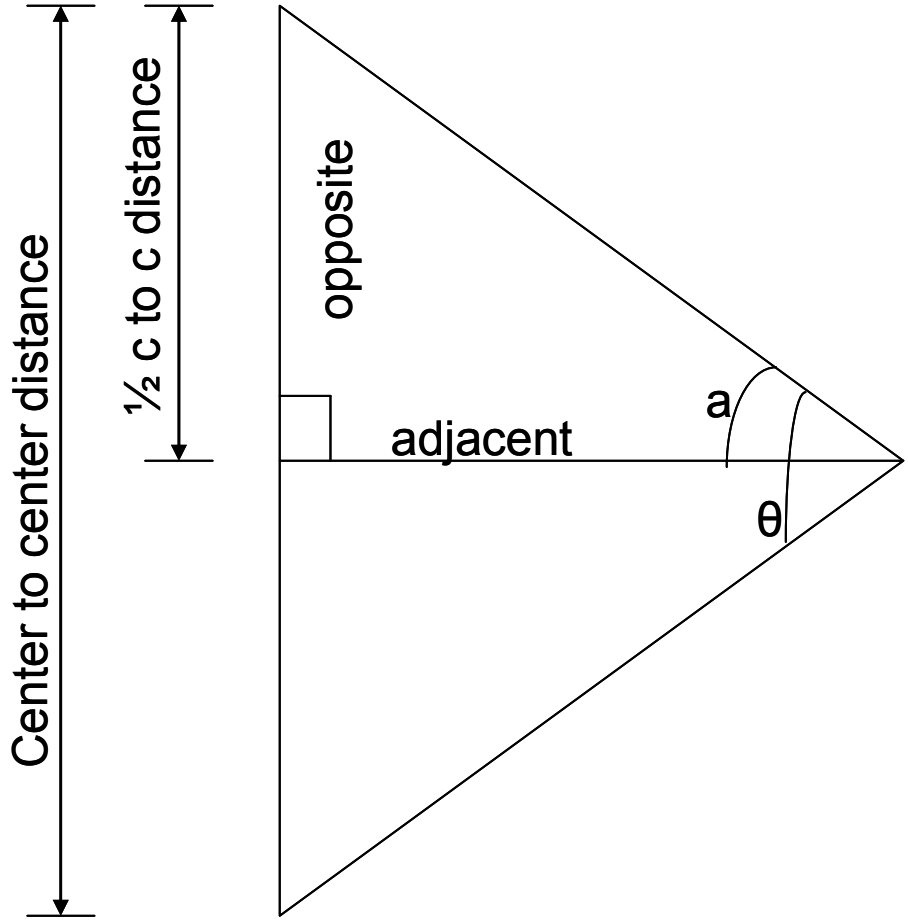

FIGURE 1: Triangle used for calculating the beam angle.

Appendix B: Standard Operating Procedure for the Quantum Cascade Laser

The quantum cascade laser is a wavelength and power tunable mid-infrared laser. The QCL utilizes a movable diffraction grating to adjust the wavelength output of the laser.

1. Turn on the water chiller; it should be set to 23°C.
2. Turn on the gray power strip. This will turn on the chopper, lock-in amplifier, detector, and power to the laser controller.
3. Turn on the laser. The power switch is located on the back of the controller box. The interlock key is located on the front of the controller box and must be in the “on” position. Then press the button to turn the laser on.
4. The laser operates using a menu system controlled by a knob and two square buttons.
5. The select button is used to select the menu, the knob scrolls through the available options (or current, wavelength, etc), and the save button locks the changes in place.
6. There are a number of menus for use. Turn the knob to scroll through the menus.
    a. Laser State Menu.
        i. Change Current: The laser has a tunable current; this menu allows the user to change the current.

ii. Relative Temperature: The user can regulate the relative temperature of the laser with this menu option.

iii. Wavelength: This allows the user to set the wavelength within the operational parameters of the laser.

iv. Convert Units: Allows the user to switch between nm and cm^{-1} units of measure.

b. Laser Operation Menu

i. Mode: Allows the user to select between pulsed, continuous wave, and CW-mode-hop-free settings.

ii. Pulse Width: Allows the user to change the pulse width in the pulsed mode.

iii. Frequency: Allows the user to change the rep rate of the pulsed mode laser.

iv. Duty Cycle: Allows the user to adjust the duty cycle of the laser.

The pulse width, frequency, and duty cycle are all connected. Adjusting one parameter will result in changes in the other two parameters. The laser is designed to do this so that it will operate properly as the parameters are changed.

c. Laser Scan Menu

i. Forward/Reverse sweep: The laser will sweep through the full tuning range of the laser.

ii. Forward sweep: The laser will sweep through the wavelengths, then reset back to home before starting another sweep.

iii. Automatic step: The laser will scan through the tuning range in a stepwise fashion, using the parameters set by the user.

iv. Manual step: The user can controller when the step is made by pressing the appropriate button.

d. Save/recall menu:

i. This allows the user to set operational parameters and to use them.

e. Information menu:

i. This allows the user to identify the laser part number, laser operation hours, controller operation hours, etc.

7. The following scan mode parameters are set using the laser box.

a. Laser Start: Sets the beginning wavelength.

b. Laser End: Sets the finishing wavelength.

c. Laser Step: Sets the distance interval between two wavelength measurements.

d. Cycles: This sets the number of time the laser will perform the scan.

e. Rate: This sets how quickly the laser moves the wavelength selection grating. 6 μmicro steps are fastest. 1 μmicro step is slower. It is noticeably slower.

f. Run step: Hit the button to start the analysis.

8. Aux 1 port outputs a signal that is collected in AIDA. The laser controller generates a voltage signal that is fed from Aux 1 to AIDA ADC channel 1. When the diffraction grating is moving, the output is zero volts. When the diffraction grating is stationery and the output is stable, the output is 5 volts.

If the water chiller is not turned on, the laser head will over heat. The laser will shut down and the controller display will note that there is a laser head temperature error. To resolve this, turn the water chiller on and let it circulate through the laser head until it is cool to the touch. Turn off the controller for 10 seconds. Then turn the controller on as described above. This should clear the error and start the laser.

Appendix C: Operation of the Mid-Infrared Camera

The mid-infrared camera is used to visualize the QCL beam. It feeds the image through a specific cable into a television screen.

1. Plug in the white cord. The camera will turn on automatically. There is no power switch.
2. Turn on the TV monitor.
3. Open the controller program. This is kept on a CD-ROM.
4. Adjust the settings as needed to optimize image quality.